

NORTHWESTERN UNIVERSITY

A Gli-Targeted Cobalt Complex and Nanoparticle Delivery Agents
for Hedgehog Pathway Inhibition

A DISSERTATION

SUBMITTED TO THE GRADUATE SCHOOL
IN PARTIAL FULFILLMENT OF THE REQUIREMENTS

for the degree

DOCTOR OF PHILOSOPHY

Field of Chemistry

By

Elizabeth Bajema

EVANSTON, ILLINOIS

December 2018

© Copyright by Elizabeth Bajema 2018

All Rights Reserved

Abstract

Many transcription factors (TFs) regulate oncogenic processes and are therefore desirable targets for drug intervention. However, few TF inhibitors have been developed to date due to a lack of specificity and few TF binding pockets. The Meade Lab has overcome these challenges by using cobalt-based complexes that disrupt Cys₂His₂ zinc finger structural motifs. The cobalt-Schiff base complexes are specific and irreversible inhibitors of zinc finger TFs. In the work presented here, a cobalt-Schiff base complex targeted to Gli TFs was generated. Gli is a known oncogene and the ultimate effector of Hedgehog pathway signaling, heavily implicated in basal cell carcinoma, medulloblastoma, and pancreatic adenocarcinoma.

To allow for activatable fluorescence imaging, the cobalt-Schiff base inhibitor was fluorescently modified and was delivered to cells with spherical gold nanoparticles (AuNP) and graphene oxide nanosheets (GO). This allows for facile visualization and tracking of the fluorescent active agent *in vitro*. Because the fluorophore is quenched by proximity to the AuNP or GO when attached, the presence of fluorescence indicates successful release of the drug payload. This work demonstrates *in vitro* specificity for Gli protein and successful delivery and visualization of Co-DNA constructs in live cells.

Acknowledgements

Thank you, first and foremost, to my advisor Tom. You have supported me personally and professionally over the last six years, and I cannot imagine what my graduate career would have been like without you. From grant applications and science dilemmas to whirlyball and ping pong, I've always known I can count on you to be my ally (or fierce competitor, as the case may be). I will always carry with me the memories of "bickering" over grant applications and laughing when we're done. And who could forget the year the Meade lab Christmas party went til 3am and you fed us all soup? Life in the Meade lab is never boring, and we mostly have you to thank for that. Joking aside, I am proud to tell interviewers about the great degree of intellectual independence that is the mark of a Meade lab graduate. That is specifically thanks to your leadership, and I know I am a better scientist and thinker because of it.

I am grateful as well to the current Meade lab members: Casey, Shaunna, Hao, Tyler, Megan, Meghan, Mike, Kaleigh, Chris, and Andrew. CAKE/Jurassic/Bio office, thanks for always being willing to chat with me when I needed a break. Kaleigh, you were the best ever co-author to write a review with. Am I saying that at least partly because we enabled one another to procrastinate til the last minute? Yes I am. No regrets. Meghan, it's been so wonderful to train you; you are motivated and awesome and I believe in your four year goal! Andrew, thank you for jumping on the cobalt train to help move this project forward.

Many past Meade lab members have been a crucial part of my success in graduate school as well. Laura Lilley, my 2012 partner in crime, I wouldn't have found the Meade lab without you, and your friendship made life better. Marie and Nat, thank you for teaching me everything I needed to be successful in graduate school. Special shout-out to all Tequila office members, may its memory rest in peace: Lauren, Victoria, Taryn, Justin, and Marie (honorary). This burns.

Thank you to Abbey and Hal, the amazing undergrads. You are both brilliant and off doing wonderful things- keep it up! Abbey, I'm so glad I had a chance to get to know you and work with you before you graduated. Hal, you are like family to me. I'm so proud of your hard work ethic and I know it will serve you well at Wayne State. Since you've graduated and left the Meade lab, I've had to listen to Weezy in the cell room. All. By. Myself. And I don't know if I can forgive you for that.

And finally, thank you times one million to my family, friends, Looah, and Mike. You all know what you mean to me. Thank you for supporting me, loving me, laughing with me, and drinking with me. Not necessarily in that order.

List of Abbreviations

^1H NMR	proton nuclear magnetic resonance
3-HPA	3-Hydroxypicolinic acid
3ThioMC3-D	3' Thiol Modifier C3 S-S from Integrated DNA Technologies
5AmMC6	5' Amino modifier C6 from Integrate DNA Technologies
acacen	acetylacetonato ethylenediamine
acacenHA	6,7-Heptanoicoacetylacetonatoethylenediamine
AFM	Atomic force microscopy
AP	alkaline phosphatase
Au	Gold
AuGliCo	AuNP functionalized with CoGli
AuNP	Gold nanoparticle
BCC	Basal cell carcinoma
BME	Basal medium eagle
BSA	Bovine serum albumin
CBS	Calf bovine serum
CD	circular dichroism spectroscopy
Ci	Cubitus interruptus protein
Co(acacen)	$[\text{Co}(\text{acacen})(\text{NH}_3)_2]^+$
Co(acacenHA)	$[\text{Co}(6,7\text{-Heptanoicoacetylacetonatoethylenediamine})]^+$
Co-DNA	Co(acacenHA) peptide coupled to a DNA sequence
CoGli	Co(acacenHA) peptide coupled to Gli consensus sequence DNA

CoGliFluor	Co(acacenHA) peptide coupled to Gli consensus sequence DNA modified with AlexaFluor488
Cys	Cysteine
Da	Daltons
DAPI	4',6-Diamidino-2-phenylindole
DCC	1,3-Dicyclohexylcarbodiimide
DFT	density functional theory
DHAP	2',6'-Dihydroxyacetophenone
DLS	dynamic light scattering
DMEM	Dulbecco's modified eagle medium
DMF	Dimethylformamide
DMSO	Dimethylsulfoxide
DPBS	Dulbecco's Phosphate-Buffered Saline
dsDNA	Double stranded DNA
DTT	Dithiothreitol
EDC	1-Ethyl-3-(3-dimethylaminopropyl)carbodiimide
EDTA	Ethylenediaminetetraacetic acid
E-FABP	Epidermal fatty acid binding protein
EMSA	electrophoretic mobility shift assay
EMT	epithelial-to-mesenchymal transition
ESI-MS	electrospray ionization mass spectrometry
EtBr	ethidium bromide
EtOH	Ethanol

ex/em	Excitation/emission wavelengths of a fluorophore
FBS	Fetal bovine serum
Gli	Gli family transcription factor proteins
Gli fwd	Forward single-stranded Gli consensus sequence DNA (5'-CTACCTGGGTGGTCTCT-3')
Gli rev	Reverse single-stranded Gli consensus sequence DNA (5'-AGAGACCACCCAGGTAG-3')
Gli1	Gli family protein Gli1
Gli2	Gli family protein Gli2
Gli3	Gli family protein Gli3
Gli _A	Gli family proteins in transcription activator form
Gli _R	Gli family proteins in transcription repressor form
GO	Graphene oxide nanosheet
GO-PEI	PEI-functionalized graphene oxide
GO-PEI-CoGli	PEI-functionalized graphene oxide with adsorbed CoGli
H ₂	Hydrogen gas
H ₂ O ₂	Hydrogen peroxide
HCl	Hydrochloric acid
HEPES	(4-(2-hydroxyethyl)-1-piperazineethanesulfonic acid)
Hh	hedgehog
HI-FBS	Heat-inactivated fetal bovine serum
His	histidine
HIV	human immunodeficiency virus

HNO ₃	Nitric acid
HSV-1	herpes simplex virus type 1
IC ₅₀	cytotoxicity, reported as 50% of the dose required for cell death
ICl	Iodomonochloride
ICP-MS	Inductively-coupled plasma mass spectrometry
IR	Infrared (spectroscopy)
K _b	binding constant of metal complex with DNA
KCl	Potassium chloride
KCN	Potassium cyanide
KMnO ₄	Potassium permanganate
L	ligand
LAR II	Luciferase assay reagent II
LOD	Limit of detection
m/z	Mass to charge ratio
MALDI-TOF	matrix assisted laser desorption ionization time of flight
MeCN	Acetonitrile
MeOH	Methanol
MES	2-ethanesulfonic acid buffer
MgCl ₂	Magnesium chloride
MgSO ₄	Magnesium sulfate
mH ₂ O	Millipore water
MIC	minimum inhibitory concentration

MLCT	metal-to-ligand charge transfer
mp	Melting point
MS	mass spectrometry
MW	Molecular weight
MWCO	Molecular weight cutoff
N ₂	Nitrogen gas
Na ₂ S ₂ O ₃	Sodium thiosulfate
NaCitrate	Sodium citrate tribasic dihydrate
NaOH	Sodium hydroxide
NH ₃	Ammonia when free, ammine when bound as a ligand
NHS	N-Hydroxysuccinimide
NP	Nanoparticle
PEI	Polyethyleneimine
PI	propidium iodide
pNPP	para-nitrophenyl phosphate
Ptch	Patched protein
qPCR	Quantitative real-time polymerase chain reaction
RB flask	Round bottom flask
RT	Room temperature
RT-qPCR	Quantitative real-time polymerase chain reaction
S100A7	Psoriasin
SAG	Smoothened agonist

Shh	Sonic hedgehog protein
Smo	Smoothed protein
SNA	Spherical nucleic acid
ssDNA	Single stranded DNA
TBE	Tris borate EDTA
TEM	Transmission electron microscopy
TEMED	N,N,N,N'-tetramethylenediamine
TF	Transcription factor
T _m	DNA melting temperature
Tris	Tris(hydroxymethyl)aminomethane buffer
UV/Vis	Ultraviolet/visible absorption spectroscopy
V	Volts
ZFTF	zinc finger transcription factor
ZnSO ₄	Zinc sulfate

*Dedicated to Tony,
who always wanted me to be a doctor*

Table of Contents

CHAPTER 1: INTRODUCTION	37
1.1. Introduction to Cobalt-Schiff Base Complexes	37
1.2. Antimicrobial Activity of Cobalt-Schiff Base Complexes	38
1.2.1. Common Methods for Assaying Antimicrobial Activity	39
1.2.2. Preclinical Complexes with Demonstrated Potency	41
1.2.2.1. Cobalt-Schiff Bases Incorporating Azido Ligands	42
1.2.2.2. Cobalt-Schiff Bases with Large Lipophilic Ligands	43
1.2.2.3. Cobalt-Schiff Bases Containing Modifications of Clinically Approved Agents	44
1.2.2.4. The Effect of Halogen Substitution on Cobalt-Schiff Base Antimicrobial Activity	45
1.3. Antiviral Activity of Cobalt-Schiff Base Complexes	47
1.4. Anticancer Activity of Cobalt-Schiff Base Complexes	48
1.4.1. Nonspecific Cytotoxic Cobalt-Schiff Bases	48
1.4.1.1. Methods for Assessing DNA Interaction Mechanism	49
1.4.1.2. Preclinical Complexes with Demonstrated Cytotoxicity or DNA Interaction	51
1.4.2. Histidine-Targeted Cobalt-Schiff Bases	55
4.2.1. Investigating Mechanism of Action	56
4.2.2. Investigating <i>In Vitro</i> and <i>In Vivo</i> Biological Activity	58

CHAPTER 2: HEDGEHOG PATHWAY STUDIES IN MAMMALIAN CELLS	61
2.1. Background, Hedgehog Pathway	61
2.1.1. Hedgehog Pathway and Basal Cell Carcinoma (BCC)	62
2.1.2. Hedgehog Pathway and Medulloblastoma (MB)	63
2.2. Approach for Hedgehog Pathway Inhibition	64
2.3. Specificity of CoGli <i>In Vitro</i>	66
2.4. Investigations in C3H/10T1/2 Cells	68
2.4.1. Hh Pathway Induction	68
2.4.2. Hh Pathway Inhibition by CoGli	69
2.5. Investigations in NIH/3T3 Shh Light II Cells	71
2.5.1. Hh Pathway Induction	71
2.5.2. Hh Pathway Inhibition by CoGli, Not Conclusively Determined	72
2.5.3. Cell viability	74
2.5.4. Confocal Microscopy	75
2.6. qPCR in ASZ Cells	76
2.7. Conclusions and Future Work	77
2.8. Materials and Methods	78
2.8.1. Electrophoretic Mobility Shift Assay (EMSA)	78
2.8.2. C3H/10T1/2 Cell Assays	80
2.8.2.1. Culture Method	80
2.8.2.2. Alkaline Phosphatase Assay	81
2.8.2.3. Total Protein Assay	81
2.8.3. NIH/3T3 Shh Light II Cell Assays	82

	15
2.8.3.1. Culture Method	82
2.8.3.2. Dual Luciferase Assay	82
2.8.3.3. MTS Assay for Cell Viability	83
2.8.3.4. Confocal Microscopy for Visualization of CoGliFluor Delivery.....	83
2.8.4. qPCR in ASZ cells	84
2.8.4.1. Culture Method: ASZ and BSZ	84
2.8.4.2. qPCR Culture Method and Primers	84

CHAPTER 3: NANO CONSTRUCTS FOR CELLULAR DELIVERY OF CO-DNA86

3.1. DNA-Functionalized Spherical Gold Nanoparticles (AuNP)	86
3.1.1. Background and Design of Nano Construct	86
3.1.2. DNA Loading and Release from Spherical AuNPs	87
3.1.3. Cellular Uptake and Viability	90
3.1.4. Confocal Microscopy	90
3.1.5. Biological Activity	91
3.2. Graphene Oxide (GO) Nanosheets	92
3.2.1. Background and Designs of Nano Constructs	92
3.2.2. DNA Loading and Release from GO Nanosheets	94
3.2.2.1. 5ssGli@GO and 10ssGli@GO Loading	94
3.2.2.2. 5ssGli@GO and 10ssGli@GO Release	97
3.2.2.3. GO-PEI Synthesis	98
3.2.2.4. GO-CoGli and GO-PEI-CoGli Loading	101
3.2.3. Cellular Uptake and Viability	101
3.2.4. Confocal Microscopy	103
3.3. Conclusions and Future Work	104
3.4. Materials and Methods	106
3.4.1. Synthesis and Characterization of Nanoparticles	106
3.4.1.1. AuNP	106
3.4.1.2. GO	108
3.4.2. Loading and Release Experiments	109
3.4.2.1. DNA Functionalization of AuNP	109

	17
3.4.2.2. Characterization of DNA-Functionalized AuNP	111
3.4.2.3. Release of Fluorescently-Labeled DNA from AuNP	112
3.4.2.4. Loading of 5ssGli and 10ssGli @GO	112
3.4.2.5. Release of 5ssGli and 10ssGli from GO	113
3.4.3. Cellular Uptake and Viability	114
3.4.3.1. AuNP	114
3.4.3.2. GO	115
3.4.4. Confocal Microscopy	116
3.4.4.1. AuGliCo	116
3.4.4.2. GO	116
3.4.5. Biological Activity	117
3.4.5.1. Luciferase Assays with AuGliCo	117
REFERENCES	118

APPENDIX A: SYNTHESIS OF CO(ACACEN HA) AND CO-DNA	132
A.1. Synthesis of 6-Azido-7-Iodoheptanoic Acid	132
A.2. Synthesis of 6,7-Diazidoheptanoic Acid	134
A.3. Synthesis of 6,7-Diaminoheptanoic Acid	135
A.4. Synthesis of 6,7-Heptanoicoacetylacetonatoethylenediamine (acacenHA)	136
A.5. Synthesis of [Co^{III}(acacenHA)(L)₂]Cl	137
A.6. Co(acacenHA)-DNA Coupling Reaction	138
A.7. Co-DNA Annealing Reaction (Single Stranded → Double Stranded DNA)	139
APPENDIX B: PURIFICATION AND CHARACTERIZATION OF CO-DNA	141
B.1. Purification of Co-DNA	141
B.1.1. Purification via Analytical-Scale Ion Exchange HPLC	141
B.1.2. Purification via Benchtop Size Exclusion Chromatography	142
B.2. Characterization of Co-DNA	144
B.2.1. Mass Spectrometry	144
B.2.1.1. Matrix-assisted laser desorption ionization time of flight (MALDI-TOF) MS	144
B.2.1.2. Electrospray Ionization (ESI) MS	146
B.2.2. DNA Melting Temperature Analysis	146
B.2.3. Cobalt:DNA Ratio	147
B.2.3.1. Analyzing DNA Concentration by UV/Vis	147
B.2.3.2. Analyzing Co and P Concentrations by ICP-MS	148

APPENDIX C: PROTOCOL FOR CO-DNA**PURIFICATION BY DIONEX ION EXCHANGE HPLC150****APPENDIX D: PRELIMINARY qPCR STUDIES IN ASZ CELLS152****APPENDIX E: PROTOCOL FOR CHELEXING****FBS FOR USE IN ASZ, BSZ CELL CULTURE MEDIA153****APPENDIX F: CULTURING ASZ AND BSZ CELL LINES155****F.1. Cell Growth Media155****F.2. Cell Cryofreezing Media155****F.3. Maintenance and splitting of cells155****APPENDIX G: GOLD NANOPARTICLE SYNTHESIS PROTOCOL 157****G.1. Reaction Equivalents for 13 nm AuNP (Table G.1.) 157****G.2. Equipment and Glassware Needed157****G.3. Procedure158****G.4. Reaction Equivalents for Various AuNP Sizes 159****APPENDIX H: PRELIMINARY WORK****WITH 3D ORGANOTYPIC KERATINOCYTE CULTURES160**

	20
H.1. Experimental Setup	160
H.2. Protocol	161
H.3. qPCR Results	161
APPENDIX I: IACUC-APPROVED IN VIVO STUDY, MOUSE MODEL OF BCC	162
I.1. Rationale and Experimental Approach	162
I.2. Vertebrate Animals Section Information	163
APPENDIX J: ZINC BINDING OF	
S100A7/EPIDERMAL FATTY ACID BINDING PROTEIN	170
J.1. Background and Objectives	170
J.1.1. Psoriasin (S100A7): A Host Defense Peptide	170
J.1.2. Structure and Metal Binding of S100A7	171
J.1.3. S100A7 Complexation with Epidermal Fatty Acid Binding Protein (E-FABP)	172
J.1.4. Scientific Objectives	172
J.2. Specific Aim 1: Isolate S100A7 and S100A7/E-FABP	
from psoriatic cells by methods with literature precedent	173
J.2.1. Protein Isolation Procedure	173
J.2.2. Experimental Challenges and Contingency Plans	174

J.3. Specific Aim 2: Determine zinc binding affinities of S100A7 (uncomplexed) and S100A7/E-FABP (complexed) in various concentrations of calcium. This will be achieved using the ZinPyr4 zinc binding chromophore	174
J.3.1. Determining Zinc Binding Affinities	174
J.3.2. Calcium Competition Studies	175
J.3.3. Experimental Challenges and Contingency Plans	176
J.4. Specific Aim 3: Study behavior of S100A7 and S100A7/E-FABP in live cells, using 2D cultures of primary human keratinocytes and 3D organotypic raft cultures.	176
J.4.1. Primary Keratinocyte Studies	177
J.4.2. 3D Organotypic Skin Cultures	177
J.4.3. Experimental Challenges and Contingency Plans	178
J.5. Conclusions	179
J.6. References for Appendix J	179

List of Figures

Figure 1.38

(a) General chemical structure of a Schiff base, where R1 and R2 can be alkyl groups, aryl groups, or hydrogens, and R3 is an alkyl or aryl group.

(b) General chemical structure of the related hydrazone family of ligands, where R1, R2, R3, and R4 can be alkyl groups, aryl groups, or hydrogens. Sometimes considered a sub-category of Schiff bases, hydrazone ligands demonstrate the same electron donating properties as Schiff bases via the lone pair residing in nitrogen's sp²-hybridized orbital.

Figure 2.43

Schiff base ligands and complexes reported to have promising antimicrobial activity

(a) This series of pyrrole-derived ligands³⁰ was complexed to Co(III) and utilized azido ligands to bind remaining coordination sites, which was hypothesized to increase antimicrobial activity. Co(III) has six coordination sites total, and complexes with (i) followed the form [CoLN₃]₂, while complexes with (ii) and (iii) followed the form [CoL₂(N₃)₂].

(b) The proposed structure of a cobalt complex with large lipophilic ("bulky") ligands, where "bulkiness" was correlated with antimicrobial activity.²³

(c) A rationally designed series of complexes³² modified ciprofloxacin to chelate transition metals, and the complexes were more potent antibacterial agents than ciprofloxacin alone, likely due to increased cell permeability upon complexation.

(d) A series of complexes in which overall antimicrobial activity was correlated with having a halogen or other electrophilic substitution on the ligand.³³ This trend held true in a number of studies,³³⁻³⁶ and warrants further attention as a mechanism of antimicrobial potency.

Figure 3.47

[Co(acacen)L₂]⁺ complexes where axial ligand L = 2-methylimidazole or NH₃ have displayed extraordinary antiviral activity *in vivo*. The complex undergoes dissociative ligand exchange of its labile axial ligands to irreversibly bind His residues in biological settings. This mechanism can be exploited for therapeutic use where His residues are structurally or catalytically necessary for protein function.⁷

Figure 4.52

Schiff base ligands and complexes reported to have promising cytotoxic or DNA-binding activity

(a) A ligand-bridged, polymeric cobalt complex that is a strong intercalator.⁵⁷ Intercalators bind between nucleoside base pairs, and are usually square planar or octahedral complexes with aromatic ligands.

(b) A cobalt complex that binds the minor groove of DNA, evidenced by both experimental and modeling data.⁶¹ Groove binders may be sequence-specific, as different nucleoside combinations have different groove dimensions and properties.

(c) A cobalt complex that surface stacks on DNA via electrostatic interactions, while the free ligand is an intercalator.⁵⁵ While electrostatic interactions are weaker than intercalation and groove binding interactions, surface stackers can still cause DNA cleavage and cytotoxicity.

Figure 5.55

Proposed mechanism of inhibition of ZFTFs by Co(acacen). The complex coordinates to His residues in Cys₂His₂ zinc finger motifs through dissociative ligand exchange of axial ligands. Octahedral Co(acacen) displaces tetrahedrally coordinated Zn(II), disrupting protein structure and DNA binding function.⁴⁶

Figure 6.56

Co(acacen) conjugated to DNA, termed Co(III)-DNA. By conjugating the DNA consensus sequence of particular ZFTF, specific and potent inhibition can be achieved in cells and *in vivo*. The DNA serves as a reversible targeting moiety, while Co(acacen) provides irreversible protein inhibition.

Figure 7.57

NMR data showing the specific binding of Co-acacen to His residues in ZFTF model peptides. Upon treating a ZFTF model peptide (KSCPH CSRAF ADRSN LRAHL QTHSD V) with Co-acacen, the change in resonances of protons in the amino acid side chain were recorded. The $\Delta\delta$ Chemical Shift profile demonstrates Co-acacen's selectivity for His residues, as significant effects were only observed on the His imidazole ¹H.⁴⁶

Figure 8.59

(a) *X. laevis* embryos treated with Co(III)-Ebox show dramatically impaired neural crest formation

and migration. Embryos were injected with Co(III)-Ebox prior to neural crest migration. At stage 25 of embryo development, untreated (top) versus treated (bottom) embryos show that Co(III)-Ebox results in failure of the neural crest cells to migrate. *In situ* hybridization of Twist expression visualizes neural crest formation and cell migration with blue stain, while Co(III)-Ebox is stained red. Normal neural crest development is seen in untreated embryos, while little to no neural crest migration is observed in treated embryos, indicated with black arrows. For related work see ref ⁷⁰.

(b) Co(III)-Ci inhibits Ci ZFTF function in *D. melanogaster* embryos. Embryos treated with Co(III)-Ci show impaired denticle belt formation relative to the untreated control and Co(III)-CiMut. Co(III)-Ci treatments mimics the phenotype of Ci null embryos, indicating that the conjugate disrupts the associated pathway through inhibiting the Ci ZFTF.⁷¹

Figure 9.61

Simplified scheme of Hh pathway without (left) and with (right) Hh ligand-induced signaling. Under normal, inactive conditions the 12-pass transmembrane protein Patched (PTCH) suppresses Smoothed (SMO) and downstream activity. Gli remains in its full-length repressor forms. Under oncologic, overactive conditions suppression of SMO is relieved, allowing for activation of Gli-associated proteins and eventual truncation of Gli into activator forms.

Figure 10.65

(a) CoGli, consisting of Co(acacenHA) coupled to Gli consensus sequence DNA 5'-GACCACCA-3', is used to investigate mammalian Hh pathway signaling.

(b) CoGluFluor consists of CoGli coupled to AlexaFluor 488 dye and is used for visualization of CoGli in confocal microscopy and other studies.

Figure 11. 66

Depiction of EMSA experiment in which labeled DNA (CoGluFluor) is incubated with cell lysate containing the protein of interest. The appearance of a shifted band indicates a change in mobility of the labeled DNA due to being bound by a protein.

Figure 12. 67

EMSA showing CoGluFluor binding its protein target. 9-fold unlabeled Gli consensus sequence DNA is able to off-compete CoGluFluor, while a one base pair mutation sequence (GliMut) is not. This strongly suggests binding of CoGluFluor to Gli protein.

Figure 13. 68

C3H/10T1/2 cell morphology at low and high density (©ATCC).¹ Cells have the elongated shape characteristic of fibroblasts and are very sensitive to chemically-induced differentiation and post-confluence inhibition of cell division.

Figure 14. 69

(a) Hh pathway induction in C3H/10T1/2 cells, as measured by an increase in the concentration of alkaline phosphatase. Over the non-treated control (“0”), Shh protein yields more significant induction than small molecule smoothed agonist SAG.

(b) Concentration-dependent Hh pathway induction with 0-100nM SAG. Results demonstrate that an incubation time of at least 48 h with SAG is necessary for detectable differentiation into osteoblasts.

Figure 15. 70

CoGli inhibits Hh-mediated differentiation of C3H/10T1/2 cells into osteoblasts with statistical significance at 150 nM. CoGli can be transfected using Lipofectamine LTX (left) or Turbofect (right) transfection agent. A concentration-dependent response is not observed, as 50 nM CoGli causes a slight increase in AP levels for both conditions.

Figure 16. 70

(top) NIH/3T3 Shh light II cell morphology at high and low density (©ATCC).¹ Cells have the characteristic elongated shape of fibroblasts and are stably transfected with two luciferase proteins (bottom). The firefly luciferase gene is preceded by tandem repeats of Gli binding site DNA and a TATA box, and is therefore expressed in response to Gli. The Renilla luciferase gene is constitutively expressed under the CMV promoter, and is therefore used for normalization.

Figure 17. 71

Hh pathway induction with 24 h and 48 h incubation of Shh protein in NIH/3T3 Shh light II cells. Induction is concentration-dependent in the range of 0-30 nM Shh, and is typically 2-4-fold from baseline levels. Results are normalized to 1 (baseline) for ease of estimating fold change.

Figure 18. 73

Five small molecule controls were synthesized for use in biological assays.

- (a) Co(acacenHA), the untargeted inhibitory agent.
- (b) Free dsGli consensus sequence DNA. As DNA alone does not inhibit Gli protein, this is not expected to have any biological effect.
- (c) CoGliMut1 has one mutated base pair at a site known to be important for Gli protein-DNA recognition and binding.
- (d) CoGliMut2 has two mutated base pairs at sites known to be important for Gli protein-DNA recognition and binding.
- (e) Co-PolyT consists of the inhibitory agent coupled to a nonsense DNA sequence. Gli family proteins are not known to bind this sequence, so no specificity is expected.

Figure 19. 73

Small molecule Co- and DNA-based controls were tested in NIH/3T3 cells for Gli-responsive luminescence response. All controls for which DNA was transfected, even when no inhibitor was present, led to an apparent decrease in Gli signaling. These results suggest that this cell line is not appropriate for transfection-based studies.

Figure 20. 74

An MTS assay was used to measure relative cell viability for NIH/3T3 Shh light II cells treated with CoGli/Lipofectamine 2000, Lipofectamine 2000 alone, and SAG. No decrease in viability was seen up to 10 μ M CoGli/Lipofectamine 2000 transfection agent. The only statistically significant difference is between the cells treated in full growth media (10% FBS) and those that were not.

Figure 21. 76

NIH/3T3 Shh light II cells were treated with CoGliFluor, transfected with

- (a) no transfection agent (negative control),

(b) Turbofect, a polymeric transfection agent, or

(c) Lipofectamine 2000, a cationic liposomal transfection agent. CoGliFluor is shown in green, while NucRed nuclear stain is shown in red.

Figure 22. 81

Smoothened agonist (SAG, CAS No. 912545-86-9) is a small molecule commonly used to induce Hh pathway signaling. Stock solutions of 5 mM were prepared in DMSO, then further dilutions for tissue culture dosing were prepared in water.

Figure 23. 87

AuGliCo, the nanoconjugate designed for delivery of double-stranded CoGli into cells and tissues. AuGliCo contains a dehybridization sequence of DNA with a low T_m for heat-induced release of CoGli payload. A fluorophore allows for tracking of released payload in cells. The CoGli inhibitory agent contains an ssDNA overhang when released, but the targeting and inhibition moieties remain the same.

Figure 24. 88

A modified SNA nanoconstruct was designed for assessing temperature-induced release of hybridized DNA from the AuNP. The hybridized DNA was fluorescently labeled with TYE 665 fluorophore for easy fluorometric detection of dehybridization. The fluorophore is quenched when proximal to the NP surface, but is unquenched upon release. This same construct was used as a control (“Au-DNA control) in later studies.

Figure 25. 89

Temperature-induced release of fluorescently-labeled DNA from AuNP at RT, 37°C, and 60°C. For this study, a model version of AuGliCo was used, as shown in Figure 24. The T_m appears lower than anticipated for a 10-mer of 100% GC content (5'-CCGGCCCGGG-3'). The observed destabilization can be attributed to the high fraction of hybridized duplexes.

Figure 26. 90

(a) Cellular uptake of AuGliCo and Au-DNA control in BSZ cells after 24 h. Uptake is given in thousands of NP/cell. No statistically significant difference is observed between AuGliCo and Au-DNA control uptake at any concentration.

(b) Cell viability of BSZ after 24 h incubation with AuGliCo and Au-DNA control. No significant toxicity is noted at the studied concentrations. Concentrations of 0.1x, 1x, and 3x NP were used for both experiments, where 1x corresponds to 100 nM CoGli.

Figure 27. 91

Confocal microscopy of Au-DNA control (left) and AuGliCo (right) demonstrate cellular entry of nanoconstructs and release of fluorescently-labeled DNA. TYE 665-labeled DNA is shown in red, while DAPI nuclear stain is shown in blue.

Figure 28. 92

Gli-responsive luminescence decreases in the presence of increasing concentrations of AuGliCo and Au-DNA control. Au-DNA control is not expected to affect Gli activity, so no conclusive inhibition was demonstrated.

Figure 29. 93

CoGli with ssDNA overhangs (termed 5ssCoGli, 10ssCoGli) were generated and adsorbed to GO. The ssDNA overhang (either 5 or 10 nucleotide base pairs) is expected to interact strongly with the GO surface, while the dsDNA Gli consensus sequence is expected to interact poorly with the GO surface.

Figure 30. 94

Design of GO-CoGli and GO-PEI-CoGli. These nanoconjugates rely on noncovalent association of CoGliFluor with the GO nanosheet. GO-CoGli interacts via pi-pi stacking between the fluorophore (AlexaFluor488) and the GO surface. GO-PEI-CoGli interacts electrostatically via positively charged PEI and negatively charged dsDNA.

Figure 31. 96

UV/Vis spectra of supernatants after adsorption of 50 μ M 5ssGli with various concentrations of GO. As expected, the concentration of DNA in the supernatant decreases as the GO reaction concentration increases due to more DNA being bound by GO. Loading values calculated from these results may be artificially low, as GO does not spin down perfectly and is likely increasing absorbance maxima at 260 nm.

Figure 32. 96

5ssGli and 10ssGli loading on GO nanoparticles, calculated from UV/Vis data. Loading is given in terms of mg DNA/g GO; apparent negative values are due to the interference of a small amount GO remaining in the supernatant.

Figure 33. 97

Release of 5ssGli and 10ssGli from GO at 37°C was measured hourly over 6 h. In this intercalative assay, an increase in fluorescence indicates an increase in dsDNA concentration in the supernatant.

Figure 34. 98

An additional timepoint $t = 20$ h was measured to determine whether DNA release would continue to trend upward. The 20 h time point was not significantly higher than the 6 h time point, and in some cases was lower. If desired, additional time points could be taken between $t = 6$ h and $t = 20$ h to ascertain max release time.

Figure 35. 99

IR spectra of GO-COOH and GO-PEI. C=O stretching at 1719 cm^{-1} decreases, while amide stretches at 1616 cm^{-1} and 1571 cm^{-1} increase, indicative of formation of amide bonds. IR data belongs to Meghan Ward.

Figure 36. 100

AFM images of

(a) unmodified GO, and

(b) GO-PEI. The average z heights of unmodified GO and GO-PEI were statistically different at $p = 0.0003$. This further supports that functionalization with PEI was successful.

Figure 37.100

Upon combining CoGliFluor with GO and GO-PEI, a marked decrease in fluorescence was observed for GO-PEI-CoGli (orange) while none was observed for GO-CoGli (blue). This suggests the fluorophore-GO interaction was too weak to facilitate CoGliFluor adsorption, while robust adsorption occurred for GO-PEI-CoGli.

Figure 38. 102

CoGli delivered with GO-PEI (left) or Lipofectamine LTX transfection agent (right) is detectable by ICP-MS for cobalt. In the above scheme, a 1x concentration dose is equal to 200 nM CoGli treatment. Despite the large error bars for GO-PEI-CoGli measurements, concentration-dependent uptake is observable. The large error bars are likely due to heterogeneous resuspension of the GO pellet after harvesting cells.

Figure 39. 103

ASZ cells were dosed with four concentrations of GO-PEI and GO-PEI-CoGli, incubated for 24 h, and were subjected to an MTS cell proliferation assay. Results reveal no significant change in cell viability across the series 0x – 2x (where 1x= 200 nM CoGli).

Figure 40. 104

Mapping analysis of confocal images of three cells per condition, chosen at random.

(a) Cells treated with GO-PEI-CoGli show green fluorescence (CoGliFluor) trending with the presence of NucRed nuclear stain.

(b) Negative control cells treated with NucRed nuclear stain only do not show green fluorescence trending with the presence of NucRed.

Figure 41. 107

(a) UV/Vis absorbance spectrum of 13 nm gold nanoparticles. Peak for unmodified AuNP is expected at 520 nm, actual= 520.8 nm.158

(b) Direct image of AuNP by TEM is the most accurate way to measure AuNP size; this batch had an average diameter of 13 nm ± 2 nm.

(c) DLS is used to measure AuNP size by light scattering in solution. Size distribution by number= 15 nm.

Figure 42. 109

DLS measurements of unmodified GO show a size distribution by intensity of 89.6 – 160.1 nm for an average of 113.6 nm. This roughly corresponds to AFM results, both current and former.

Figure 43. 110

The 3' thiol Modifier 3ThioMC3-D purchased from IDT was attached to the 3' end of the DNA sequence of interest. Using DTT, the disulfide bond is cleaved, leaving the thiol bond available for binding to the Au surface.

Figure 44. 111

The 5' amino modifier C6 (5AmMC6) was used for peptide coupling Gli consensus sequence DNA to Co(acacenHA).

Figure 45.112

Fluorescence calibration curves of TYE 665-modified DNA in DPBS with and without 0.01% Tween 20 detergent. It was determined that the presence of Tween significantly increases fluorescence of TYE 665 DNA, and it is therefore important to ensure the diluent of calibration standards exactly matches that of samples being analyzed.

Figure 46.114

Calibration curves for 5ssGli and 10ssGli. Each has a 17 bp dsDNA region to which Quant-iT fluorophore can bind. Both curve fits have $R^2=0.999$, demonstrating that the Quant-iT HS assay is appropriate for use with these samples.

Figure B.1. 141

Dionex ion exchange HPLC traces of Co-DNA without phosphorothioate bonds (left) and with phosphorothioate bonds (right). The presence of phosphorothioate bonds yields poor separation by ion exchange.

Figure B.2. 143

(a) UV/Vis spectra of eluted CoGli fractions 1-5 from size exclusion chromatography. When comparing against ICP-MS data, fraction 3 was determined to have a Co:DNA ratio close to 1. Spectra were obtained using the 1 mm path length microvolume sample tray, which likely accounts for spectral noise; noise can be decreased by averaging 5-10 scans.

(b) UV/Vis spectra of eluted CoGli fractions 5-13 from size exclusion chromatography. In these scans, the concentration of Co(acacenHA) is higher, accounting for the spectral feature at 340 nm. These fractions contained a stoichiometric excess of Co(acacenHA) and were therefore not used.

Figure B.3. 145

A representative MALDI-MS spectrum of CoGli. The peak at 5322.9 is similar to (but not precisely) the mass of Gli rev= 5309.8. The identity of the peak at 4326.8 is unknown.

Figure B.4. 146

An analysis of six MALDI samples (four dsCoGli and two ssCoGli) demonstrates that while peaks do not exactly match one another or the target mass, common groupings are seen for dsCoGli and ssCoGli. Peak 1 indicates the singly charged species; while Peak 2 indicates the doubly charged species.

Figure B.5.147

Melting temperature analysis of CoGli verifies the double-stranded nature of the DNA. An increase in chromicity at 260 nm is observed with increasing temperature, indicating dehybridization of DNA. “Forward” trace indicates the trend with temperature ramping up, while “Reverse” trace indicates trend with temperature ramping down.

Figure D.1. 152

ASZ cells were serum-starved to induce Hh pathway signaling and treated with CoGli/transfection agent as well as relevant controls (see Figure 18). Treatments were 200 nM unless otherwise indicated. Cells were harvested in TRIzol and analyzed by qPCR for Gli1mRNA levels, normalizing to TUBB. CoGli, Co-PolyT, and CoGliMut2 all decreased Gli1 mRNA levels as much as the known Smo inhibitor cyclopamine. Free dsGli DNA did not exhibit an inhibitory effect, unlike results seen in NIH/3T3 Shh light II cells. While it is unclear why Co-PolyT and CoGliMut are inhibiting so effectively, these preliminary results are promising. Future work will include a concentration-dependent study to determine whether 200 nM is simply too much of any Co(acacenHA) agent.

Figure G.1. 157

Required glassware for AuNP synthesis

Figure G.2. 158

Reflux setup for glassware for AuNP synthesis

Figure H.1. 160

Organotypic cultures of primary keratinocyte (neonatal foreskin). Meade/Perez White/SDRC Collaboration 08-05-2018. 3D Reconstituted Human Skin, Experiment #1. Day 0 (08-05-2018 start of culture at the air-liquid interface [ALI]), Treatments started 08-13-2018, Day 8. PURPOSE: To define parameters for activation of Hh pathway.

Figure H.2. 161

qPCR results for organotypic cultures, were n=2 for each treatment condition. Samples were analyzed for Gli1 mRNA levels and normalized to TUBB.

Figure J.1. 171

(a) Crystal structure of S100A7 homodimer bound to two Ca(II) ions in the EF-hand domains. PDB 1PSR NGL viewer.

(b) Closeup of Zn(II) bound in His3Asp site at homodimer interface with distorted tetrahedral geometry. Also shown is the Cys47/Cys96 disulfide bond.

Figure J.2. 175

Chemical structure of ZinPyr-4. Upon binding zinc ($K_d \sim 0.7$ nM), ZinPyr-4 undergoes a 5-fold increase in fluorescent intensity.

Figure J.3. 176

Chemical structure of FluoZin3. FluoZin3 binds zinc with $K_d = 15$ nM, but can be used as an alternative fluorescent probe for the S100A7/EFABP system.

Figure J.4. 177

Illustration of a 3D organotypic skin culture. Keratinocytes grown at the air-medium interface will differentiate into an epidermis-like structure, useful for studying live skin-like tissue without necessitating patients or animals.

Figure J.5. 179

Confocal microscopy analysis for

(a) E-FABP,

(b) S100A7, and

(c) overlay demonstrating colocalization in keratinocytes.

List of Tables

Table G.1.	157
Reaction Equivalents for 13 nm AuNP	
Table G.2.	159
Gold to NaCitrate Ratio for Synthesizing AuNP of Various Sizes	
Table I.1.	166
Mice needed for proposed in vivo experiment	

List of Schemes

Scheme 1	79
-----------------------	----

EMSA Reaction Conditions and Legend

Scheme A.1.	132
--------------------------	-----

Synthesis scheme for Co(acacenHA). In brief, 6-heptenoic acid is converted to 6-azido-7-iodoheptanoic acid by addition of iodomonochloride and sodium azide. After purification by flash chromatography, the product is converted to 6,7-diazidoheptanoic acid by addition of additional sodium azide. Following extraction in ether, the product is hydrogenated to yield 6,7-diaminoheptanoic acid. A condensation reaction with 2,4-pentadione is then performed to yield the unmetallated acacenHA ligand (6,7-Heptanoicoacetylacetonatoethylenediamine). The ligand is metallated and ammine axial ligands are added to yield the final product Co(acacenHA) which is used for peptide coupling amine-modified DNA.

CHAPTER 1: INTRODUCTION

1.1. Introduction to Cobalt-Schiff Base Complexes

Transition metal complexes offer a diverse array of geometries and oxidation states, making this class an excellent platform for new and innovative therapeutics.^{1,2} Since the discovery of cisplatin as a potent but toxic anticancer drug,³ the field has focused on developing less toxic and increasingly effective transition metal complex therapeutics. One option for mitigating toxicity of transition metal complexes is to choose trace essential metals that humans are known to tolerate well.⁴ Cobalt is one example, and despite its pharmaceutical promise it remains relatively ignored by pharmaceutical chemistry. Several excellent reviews of cobalt-based therapeutic research exist,⁵⁻⁸ but the biological properties of cobalt complexes vary widely depending upon the chelation strategy. As a result, the scope of this introduction is narrowed to cobalt complexes of Schiff bases ligands. However, it is notable that non-Schiff base cobalt complexes are having success as redox-activated prodrugs and drug delivery vehicles.^{9,10}

Schiff bases are a synthetically flexible class of imines typically formed by condensation of a primary amine with an aldehyde or ketone (see Figure 1a below). First described by Hugo Schiff in 1864,¹¹ Schiff bases have since been studied as antifungals, antibacterials, antimalarials, anti-inflammatories, antivirals, and antitumor agents.¹²⁻¹⁴ In addition, Schiff bases are selective metal chelators whose biological properties are often enhanced upon complexation with a transition metal.¹⁵ This chapter will highlight preclinical applications of cobalt-Schiff base complexes as potent antimicrobials, effective antivirals, and specific and non-specific anticancer agents.

1.2. Antimicrobial Activity of Cobalt-Schiff Base Complexes

Metal complexes of Schiff bases have long been of interest as potential antimicrobial agents, including as both antifungals and antibacterials. In 1952, the first biological investigation with cobalt complexes demonstrated bacteriostatic and bactericidal activity in the μM range, while also exhibiting low systemic toxicity in mice.¹⁶ Since then, low-cost methods for testing antifungal and antibacterial activity have become commonplace, and concern over antibiotic-resistant bacteria has increased drastically.¹⁷ This combination of low cost and rising need has yielded a prolific field of research into transition metal-Schiff base complexes as antimicrobial agents.^{15,18} The closely related hydrazone family of ligands (Figure 1b) demonstrates similar electron donating properties as Schiff bases, and hydrazone complexes are mentioned where noteworthy.

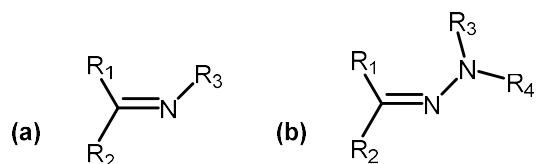


Figure 1. (a) General chemical structure of a Schiff base, where R₁ and R₂ can be alkyl groups, aryl groups, or hydrogens, and R₃ is an alkyl or aryl group. **(b)** General chemical structure of the related hydrazone family of ligands, where R₁, R₂, R₃, and R₄ can be alkyl groups, aryl groups, or hydrogens. Sometimes considered a sub-category of Schiff bases, hydrazone ligands demonstrate the same electron donating properties as Schiff bases via the lone pair residing in nitrogen's sp²-hybridized orbital.

Although Schiff base complexes are well studied as antimicrobial agents, their antimicrobial mechanism is not fully understood. It has been noted that three normal cellular processes are disrupted: (1) enzymatic metal binding site activity, (2) cellular respiration, and (3) protein production.^{19–21} Uncomplexed Schiff bases can affect these processes, but complexation usually enhances their overall cytotoxic effect. This is attributed to Tweedy's chelation theory

which states that chelation allows for electron delocalization and charge sharing between the metal center and its donor ligands,²² and increases the overall lipophilic character of the complex, favoring cell membrane permeability. However, it is important to note that the measured lipophilicity does not always correlate with increased antimicrobial potency, suggesting more complex mechanisms are indicated.²³

The successful evaluation of cobalt-Schiff base complexes as antimicrobials requires understanding the strengths *and* weaknesses of common assay methods. In much of the literature, minimum inhibitory concentrations (MICs) are calculated incorrectly, or are not compared against known positive controls, making it difficult to draw reliable conclusions. To obtain trustworthy and repeatable results, synthetic chemists should work more closely with microbiologists and follow established performance standards in biological assays.²⁴ Section 1.2.1 will introduce these concepts, discussing the methods that are most commonly applied and best practices for assessing antimicrobial activity. Section 1.2.2 will highlight antimicrobial cobalt-Schiff base complexes with demonstrated antimicrobial activity, herein defined as an MIC < 1 mg/mL or favorable comparison with a known positive control. It is important to note that clinical antimicrobial potency cannot be assessed from MIC values independently. Clinical potency depends upon blood concentration levels of the microbe in question. Thus, a clinically potent MIC value varies from species to species.

1.2.1. Common Methods for Measuring Antimicrobial Activity

Methods of measuring antimicrobial activity can be broadly grouped into two categories: diffusion and dilution. While diffusion assays are typically simpler to perform, the results are qualitative and vary widely with materials used. Dilution methods require more product, but

quantify minimum inhibitory concentrations and enable comparisons across studies. However, neither diffusion *nor* dilution techniques are sufficient to clinically distinguish between bacteriostatic and bactericidal mechanisms. To gain more detailed mechanistic insights, time-kill tests and fluorescent flow cytometry are recommended. Time-kill tests provide information on time- *versus* concentration-dependence, and fluorescent flow cytometry assesses the extent of cell damage.²⁵

Diffusion assays are overwhelmingly utilized in the inorganic chemistry laboratory due to their low cost and ease of use.²⁵ In these protocols, agar media is inoculated with bacteria and treated with antimicrobial agent in a localized well or on a paper disk. As antimicrobial agent diffuses out of the treatment site and into the agar, a circular zone of no bacterial growth will result. The radius of the zone of inhibition is measured after 16–24 hours (depending on the microbial species being tested²⁴) and directly correlates with antimicrobial activity.²⁵ Diffusion methods are appropriate for qualitative screening, but should not be used to calculate MIC, as small variations in materials and protocols used yield large differences in radii of zones of inhibition.²⁶

For laboratories without an automated setup, dilution assays are more labor-intensive and require more of the antimicrobial agent. However, they are more accurate for quantitation MIC and are commonly used in clinical settings. In broth dilution protocols, serial dilutions of antimicrobial agent are treated with a fixed number of bacterial cells. Turbidity (indicative of cell growth) is measured after 16–24 hours, and MIC is defined as the lowest concentration of antimicrobial agent that visually inhibits growth.²⁵ Further subculture of non-turbid samples can determine whether small amounts of live bacteria are still present. For both diffusion and dilution assays, careful attention and adherence to standard protocols is required for reproducibility and accuracy.²⁴ Failure to follow standard protocols results in unreliable or unrepeatable results.

In the laboratory, diffusion and dilution methods are generally used to quantify growth inhibition rather than cell death, and do not provide mechanistic insights. To ascertain microbicidal activity, a time-kill curve experiment is recommended, where live bacterial suspensions are treated with antimicrobial agent and assayed for viability at intervals over 24 hours. If a series of concentrations are tested, dilution methods can be used to determine whether the agent acts via a time- or concentration-dependent mechanism. This provides dynamic information about the interaction of microbe with agent over time, and can be used to gage *in vivo* dosing.²⁵

For further mechanistic insight, flow cytometry with appropriate fluorescent dyes is used. Propidium iodide (PI) is an intercalating dye used to determine whether an antimicrobial agent disrupts the bacterial cell membrane. In bacteria with an intact cell membrane, PI is membrane-impermeable and will not be found within cells. However, if an antimicrobial agent compromises cell membrane integrity, PI can permeate and is therefore found intracellularly.²⁷ A complementary technique uses carboxyfluorescein diacetate, a membrane-permeable dye that is only activated within viable cells with esterase function.²⁸ The vast majority of literature citing cobalt-Schiff bases as antimicrobials does not include mechanistic investigations, likely due to lack of cross-talk between the fields of inorganic chemistry and microbiology. This represents a gap in the understanding of fundamental mechanisms and must be addressed by future work.

1.2.2. Preclinical Complexes with Demonstrated Potency

While cobalt-Schiff bases are routinely investigated as antimicrobials, relatively few studies determine MICs and/or compare against known antimicrobial standards. The cobalt complexes mentioned here have potent MICs (defined as < 1 mg/mL²⁹) or were shown to be more effective than an antibacterial or antifungal control. Given that MICs may vary widely depending

on the method used, comparison against an appropriate positive control should be considered the most broadly reliable indicator of potency. While the complexes cited here have not been mechanistically studied, they exploit a variety of ligand types to achieve antimicrobial activity. These types include azido ligands, large lipophilic ligands, modifications of clinically approved agents, and halogen-substituted ligands.

1.2.2.1. Cobalt-Schiff Bases Incorporating Azido Ligands

Two studies have successfully utilized cobalt-Schiff bases with azido ligands as antimicrobials.^{30,31} First, a series of three pyrrole-based ligands (Figure 2a) were prepared and complexed with Co(III); azido ligands were used to chelate the remaining open coordination sites.³⁰ Co(III) has six available coordination sites, most commonly forming octahedral complexes. Thus, ligand (i) formed a dinuclear $[\text{CoLN}_3]_2$ complex with each azido group coordinating both Co(III) centers, while ligands (ii) and (iii) formed mononuclear $[\text{CoL}_2(\text{N}_3)_2]$ complexes. Complexes with ligands (ii) and (iii) had a higher azido:cobalt ratio, and these proved more potent than the complex with ligand (i). Complexes with (ii) and (iii) had MIC values of < 0.25 mg/mL (where potency is typically defined as $\text{MIC} < 1$ mg/mL) for three or more of the bacterial species *S. aureus* and *B. subtilis* (Gram-positive), and *P. aeruginosa* and *E. coli* (Gram-negative). However, the prepared complexes were not more potent than ciprofloxacin. These results suggest that increasing the number of azido ligands per complex increases antimicrobial activity, though variations in complex stability and kinetic lability were not investigated.

In the second study, two bidentate phenol-based ligands were complexed with Co(III) and end-on azido ligands coordinated the axial positions for a composition of $[\text{CoL}_2(\text{N}_3)_2]$.³¹ These two complexes demonstrated excellent antibacterial ability, most potently against *B. subtilis* with MIC

values of 0.004 and 0.009 mg/mL. These MIC values were higher than that of penicillin (0.002 mg/mL) but were lower than sodium azide alone (0.125 mg/mL). Although the experimental conditions and controls used in this study varied from those in the first, the results still suggest that cobalt-Schiff base complexes with two azido ligands are potent antimicrobials.³¹

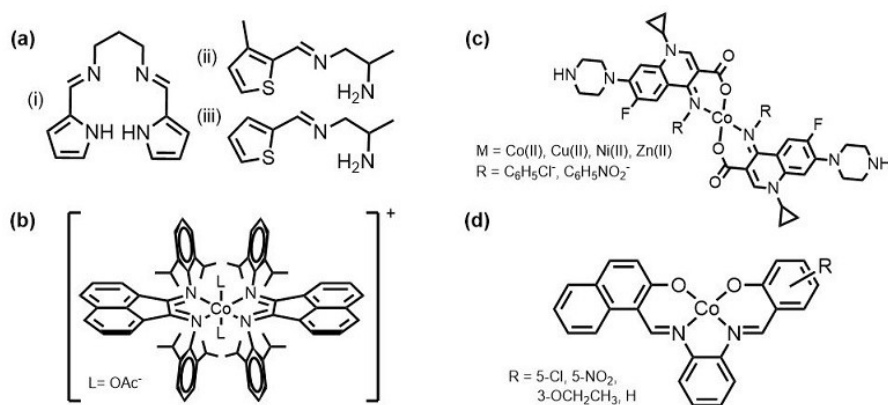


Figure 2. Schiff base ligands and complexes reported to have promising antimicrobial activity: **(a)** This series of pyrrole-derived ligands³⁰ was complexed to Co(III) and utilized azido ligands to bind remaining coordination sites, which was hypothesized to increase antimicrobial activity. Co(III) has six coordination sites total, and complexes with (i) followed the form $[\text{CoLN}_3]_2$, while complexes with (ii) and (iii) followed the form $[\text{CoL}_2(\text{N}_3)_2]$. **(b)** The proposed structure of a cobalt complex with large lipophilic (“bulky”) ligands, where “bulkiness” was correlated with antimicrobial activity.²³ **(c)** A rationally designed series of complexes³² modified ciprofloxacin to chelate transition metals, and the complexes were more potent antibacterial agents than ciprofloxacin alone, likely due to increased cell permeability upon complexation. **(d)** A series of complexes in which overall antimicrobial activity was correlated with having a halogen or other electrophilic substitution on the ligand.³³ This trend held true in a number of studies,^{33–36} and warrants further attention as a mechanism of antimicrobial potency.

1.2.2.2. Cobalt-Schiff Bases with Large Lipophilic Ligands

Ligands that are large and sterically hindered are considered “bulky,” and this property can be exploited to increase antimicrobial activity. Ligands that are both bulky and lipophilic increase the hydrophobicity of the overall complex, thereby enhancing bacterial cell penetration. One

example from the literature that directly correlates the “bulkiess” of Schiff base ligands with antimicrobial activity utilized bulky N-bisimine derivatives (Figure 2b).²³ The orthodisubstituents of these derivatives were found to contribute to antibacterial function, with the most hydrophobic substituent (2,6-diisopropylphenyl) leading to the highest biological activity. The MIC values for Co(III) complexes did not meet the 1 mg/mL limit of potency at 1.9–2.6 mg/mL, depending on the species being tested. However, antibiotic controls had a similar potency range at 1.3–2.5 mg/mL under the conditions used. In fact, the Co(III) complexes outperformed nystatin, ampicillin, and streptomycin in bacterial species, and were only bested by clotrimazole in fungal species.²³ These results suggest that increasing complex lipophilicity through the use of large, sterically hindered ligands is a promising route for developing cobalt-Schiff base complexes as antimicrobials.

1.2.2.3. Cobalt-Schiff Bases Containing Modifications of Clinically Approved Agents

A rational approach to antimicrobial complex design is to chemically modify a clinically approved agent so that it becomes suitable to coordinate a metal. For example, Schiff bases derived from ciprofloxacin have been complexed with a series of transition metals, including Cu(II), Co(II), Ni(II), and Zn(II) (Figure 2c).³² Remarkably, the transition metal complexes (including cobalt) outperformed ciprofloxacin for all antimicrobial species tested.³² This is likely because chelation allows for delocalization of π electrons over the whole chelate ring, increasing the lipophilicity of metal-ciprofloxacin complexes versus ciprofloxacin alone. Increased lipophilicity yields better membrane permeability and better antimicrobial activity.

Similarly, antipyrine-derived Schiff bases have been prepared in two studies.^{37,38} Antipyrine is clinically approved as a nonsteroidal anti-inflammatory, analgesic, and antipyretic agent. Condensing antipyrine with aldehydes or ketones to form Schiff bases has been shown to

yield products with antibacterial properties.³⁷ In the first study, an antipyrine derivative was condensed with benzil, and the resulting Schiff base was complexed with transition metals.³⁷ The transition metal complexes were found to have more antimicrobial activity than free ligand, but less than uncomplexed metal salts alone. This was an unexpected result, but it is likely that the metal salts are better able to inhibit cell respiration and enzymatic processes. In the second study, an antipyrine derivative was condensed with 2-aminophenol and 2-aminothiophenol.³⁸ The resulting Schiff bases and all metal complexes (including cobalt) were more potent than ampicillin and amphotericin in many bacterial species. The antibacterial potency is attributed to lipophilicity of the complexes and hydrogen bonding of the azomethine group with enzymatic centers of activity. Unfortunately, MIC values were not reported in either study, making direct comparisons difficult.

1.2.2.4. The Effect of Halogen Substitution on Cobalt-Schiff Base Antimicrobial Activity

Many studies have found halogen substitution on Schiff base complexes to increase antimicrobial activity. It is postulated that metal complexes with electron-withdrawing groups such as halogens have a higher binding affinity for intracellular oxygen and increased ability to disrupt cellular respiration.³³ In a series of asymmetrical Co(II) complexes (Figure 2d), all four were found to have significant antimicrobial activity. However, the presence of a halogen or other electrophilic group increased potency significantly, fitting the hypothesized mechanism.³³ Using the qualitative disk diffusion assay, cobalt-Schiff bases worked comparably well to chloramphenicol. However, quantitative tests revealed that chloramphenicol had significantly lower MICs in eight of ten bacterial strains studied, while the cobalt-Schiff bases performed better against *E. cloacae* and *B. subtilis*.³³ As these are Gram-negative and Gram-positive strains, respectively, the mechanism is

unclear, but is not related to cell membrane structure.

In a similar study, a series of five Co(II) complexes were prepared and tested for antifungal activity against three species (*A. alternata*, *F. oxysporum*, and *M. roridum*).³⁴ The closely related series displayed a surprisingly wide range of activity (MIC= 0.017 mg/mL to >1 mg/mL), demonstrating the *substantial biological effect of ligand character*. The cobalt-Schiff base series was not more effective than the indofil M-45 standard against two of three species, but the halogen-substituted complex was among the best performing.³⁴ Although the authors did not postulate a mechanism, it is possible that the halogen-substituted complex is once again better able to inhibit cellular respiration.

In line with this trend, a cobalt complex with two halogen substitutions demonstrated antibiotic and antifungal activity at 0.5 mg/mL.³⁵ However, the MIC was estimated based on a diffusion experiment, casting uncertainty on the reported values. Similarly, a cobalt complex with one halogen substitution was more effective than amikacin and ketoconazole in seven of eight bacterial strains tested in a diffusion experiment.³⁶ Halogen substitution was not the primary focus of these studies, and was therefore not mentioned by the authors as being mechanistically important. However, a summary of the literature shows a broader trend: metal complexes of Schiff bases with halogen substitution show rich potential as an antimicrobial class. Future mechanistic investigations of this class are warranted and can enable rational design of antimicrobials going forward.

1.3. Antiviral Activity of Cobalt-Schiff Base Complexes

Despite the extensive body of research employing cobalt-Schiff base complexes as antimicrobial agents, this class of complexes has made significant clinical progress as an antiviral.³⁹⁻⁴¹ CTC-96, a $[\text{Co}(\text{acacen})(\text{L}_2)]^+$ complex (Figure 3) where axial ligand $\text{L} = 2$ -methylimidazole, is the only cobalt-Schiff base to have entered clinical trials. Its synthesis was first described in 1997,³⁹ and it was found to inhibit replication of herpes simplex virus type 1 (HSV-1) in a rabbit eye model at concentrations 1000-fold lower than the clinically approved

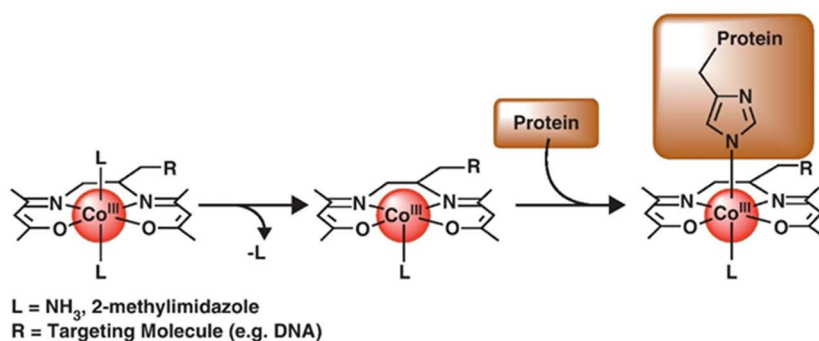


Figure 3. $[\text{Co}(\text{acacen})\text{L}_2]^+$ complexes where axial ligand $\text{L} = 2$ -methylimidazole or NH_3 have displayed extraordinary antiviral activity *in vivo*. The complex undergoes dissociative ligand exchange of its labile axial ligands to irreversibly bind His residues in biological settings. This mechanism can be exploited for therapeutic use where His residues are structurally or catalytically necessary for protein function.⁷

standard.⁴⁰ Just as significantly, a targeted version of this complex demonstrated selectivity toward Sp1 zinc finger transcription factors (ZFTF) for potential implication in treating human immunodeficiency virus (HIV).⁴² Selective targeting against ZFTF proteins drastically increases the potential for pharmaceutical applications of this class of complexes, and this method was later exploited to target pathways implicated in cancer (for mechanism and use in anticancer studies, see Section 1.4.2).

The pharmaceutical properties of $[\text{Co}(\text{acacen})(\text{L}_2)]^+$ complexes have prompted many mechanistic investigations.⁴³⁻⁴⁷ While the antiviral mechanism of CTC-96 is still not fully elucidated, it is known to coordinate histidine (His) residues through dissociative exchange of its labile 2-methylimidazole axial ligands (Figure 3).⁴⁸ Biologically, it is known to inhibit the membrane fusion events that allow for viral penetration of HSV-1.⁴¹ Thus, the most likely antiviral mechanism is via direct targeting of a histidine-containing herpes virus serine protease. For further mechanistic details on $[\text{Co}(\text{acacen})(\text{L}_2)]^+$ complexes, see Section 1.4.2.

1.4. Anticancer Activity of Cobalt-Schiff Base Complexes

Schiff base complexes with anticancer activity can be grouped broadly into two categories: (i) those exhibiting nonspecific cytotoxic activity, and (ii) those that selectively target a cancer-associated protein or pathway. The majority of published literature belongs to the former category, with therapeutic success largely relying upon making fortuitous discoveries as with cisplatin.³ While targeted cobalt-Schiff base complexes comprise a much smaller body of literature, they can be rationally designed for greater likelihood of biological success. Section 1.4.1 will discuss nonspecific cytotoxic cobalt-Schiff bases that are studied for their interaction with DNA, while Section 1.4.2 will discuss targeted complexes that rely on protein recognition for biological specificity.

1.4.1. Nonspecific Cytotoxic Cobalt-Schiff Bases

Metallodrugs have been found to accumulate in cancer cells, a property which contributes to their success as cytotoxic agents.⁸ Accumulation is attributed to cancer cells' requirement for increased concentrations of vitamin B12, which functions as a metallodrug carrier ligand.⁴⁹ Given that preferential accumulation of a drug in cancer cells *versus* normal cells is crucial for therapeutic

success, cytotoxicity should always be tested in cancerous and noncancerous cell lines. Metallodrugs display a wide variety of cytotoxic mechanisms,⁵⁰ but the most commonly studied involve interaction with DNA. In Section 1.4.1.1, the most commonly used methods for assessing DNA interaction will be discussed. In Section 1.4.1.2, several promising examples of cobalt-Schiff base complexes as cytotoxic or DNA-binding agents will be described.

Although beyond the scope of this chapter, excellent work is being done with non-Schiff base cobalt complexes as anticancer prodrugs.⁵¹⁻⁵³ The reduction potential of Co(III) complexes can be tuned for selective release in hypoxic environments, such as the tumor microenvironment, allowing for *activation* of a Co(II) agent, or release of an active ligand into cancerous cells. These agents have been further modified to incorporate fluorophores, allowing visualization of hypoxia selectivity in spheroid cell culture tumor models.⁵⁴

1.4.1.1. Methods for Assessing DNA Interaction Mechanism

Metal complexes can interact with DNA by means of intercalation (between the base pairs), major or minor groove binding (between turns of the double helix), or surface stacking via electrostatic interactions. The least ambiguous way to distinguish between intercalative and non-intercalative interactions is to perform viscosity measurements.⁵⁵ Intercalating agents increase the axial length of DNA as they separate its base pairs. This makes the structure of DNA more rigid, yielding a concomitant increase in viscosity. Partial intercalators, on the other hand, may bend the DNA structure causing shortening and a reduction in viscosity, while groove-binding causes little to no change in viscosity.⁵⁵ Because changes in viscosity result from *physical* changes in the structure of DNA, they provide the most direct information about intercalative vs. non-intercalative binding modes.

Electronic absorption titration can be used to investigate the binding mode when the ligands of interest contain aromaticity. Intercalation allows for strong π - π stacking when aromatic ligands interact with the base pairs of DNA. This causes a hypochromic shift in DNA's absorbance spectrum, and the magnitude of shift is correlated with binding strength.⁵⁶ The binding constant (K_b) can be determined using Equation (1):

$$[\text{DNA}]/(\varepsilon_a - \varepsilon_f) = [\text{DNA}]/(\varepsilon_b - \varepsilon_f) + 1/K_b(\varepsilon_b - \varepsilon_f) \quad (1)$$

where ε_a is the apparent absorption coefficient of the complex, ε_f is the extinction coefficient of the free complex, and ε_b is extinction coefficient of the metal complex fully bound to DNA.⁵⁷ Because electron absorption studies allow for quantitation of K_b , they are considered a gold standard when aromatic ligands are involved.

In an analogous method to electronic absorption titration, fluorescence titration can be used when the metal complex exhibits autofluorescence.⁵⁷⁻⁵⁹ The emission intensity of an intercalating agent increases when titrated with DNA, while emission intensity of a surface stacking agent is quenched. Upon intercalating, a suitable metal complex penetrates into hydrophobic regions of DNA, yielding less quenching from surrounding water and a concomitant increase in emission intensity. Conversely, the fluorescence of a stacking agent is quenched due to electron transfer from DNA to the excited MLCT state of the complex. Depending on the mechanism, equations are available to determine K_b from these experiments.^{55,60}

An alternative fluorescence method exploits the strongly intercalating fluorophore ethidium bromide (EtBr). When pre-incubated with DNA, EtBr can be off-competed by an intercalating complex but not a groove binding or surface stacking complex. Since the emission intensity of EtBr (rather than the complex) is being monitored, this experiment provides indirect

evidence of binding mode, and is therefore useful as a secondary confirmation of prior results.⁵⁷

Circular dichroism (CD) uses circularly polarized light to investigate DNA secondary structure, specifically interrogating changes in base pair stacking interactions and helicity. Free DNA exhibits a positive band near 275 nm and a negative band near 245 nm due to base pair stacking and right-handed helicity, respectively. Intercalators show strong base pair stacking and stabilize the right-handed B conformation of DNA. This causes an increase in intensity at both 275 and 245 nm. Groove binders and surface stackers cause little to no change in CD spectra.^{55,61}

Upon interacting with DNA, some metal complexes will cause DNA cleavage. To assay for cleavage, gel electrophoresis is performed on a pre-incubated solution of DNA and agent. After staining to visualize, multiple bands of DNA indicate that cleavage has occurred. As DNA cleavage is often mediated by oxidation, oxidants and reductants can be added to the reaction to further examine their roles.⁶²

These techniques are routinely used to investigate metal complex-DNA interactions. Viscosity measurements and electronic or fluorescence absorption studies are considered the gold standards, while EtBr competition and CD are often used as secondary techniques to confirm prior results. It is always necessary to employ multiple methods, as this grants greater certainty to the proposed mechanism.

1.4.1.2. Preclinical Complexes with Demonstrated Cytotoxicity or DNA Interaction

A group of hydrazone complexes has been investigated for cytotoxicity in five cell lines: HL-60, Caov-3, HeLa, MCF-7, and MDA-MB-231.⁶³ Cytotoxicity (IC_{50}) is calculated as 50% of the dose required for cell death. A low IC_{50} is obviously desirable, but because nonspecific toxicity is cisplatin's major shortcoming, a lower IC_{50} than that of cisplatin is considered a disadvantage.

Of the studied complexes, a Co(II) complex showed cytotoxic activity against MCF-7 cells ($IC_{50} = 1.8 \mu\text{g/mL}$) that approached that of the anticancer drug tamoxifen ($IC_{50} = 1.5 \mu\text{g/mL}$). Metal chelation was found to slightly inhibit cytotoxic activity in this series, with the free ligand demonstrating a lower IC_{50} than any of its complexes or tamoxifen. Despite demonstrating such toxicity towards MCF-7 cells, little to no activity was observed in other cell lines.⁶³ These results demonstrate the importance of using *multiple* cell lines for preliminary cytotoxicity studies, although this is frequently overlooked in reports of novel complexes.

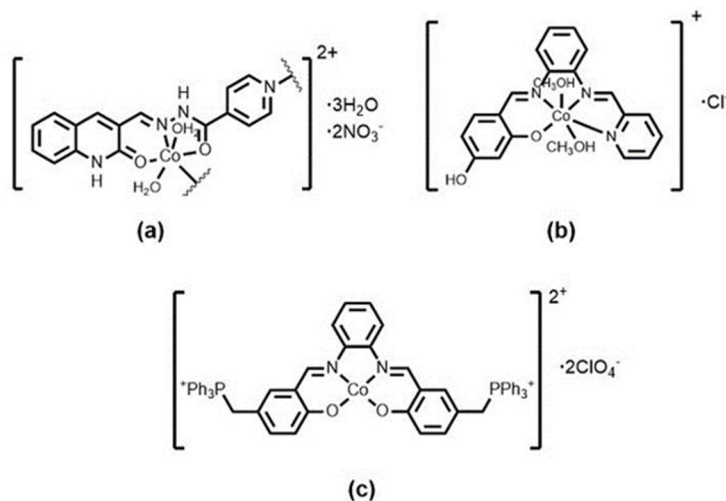


Figure 4. Schiff base ligands and complexes reported to have promising cytotoxic or DNA-binding activity: **(a)** A ligand-bridged, polymeric cobalt complex that is a strong intercalator.⁵⁷ Intercalators bind between nucleoside base pairs, and are usually square planar or octahedral complexes with aromatic ligands. **(b)** A cobalt complex that binds the minor groove of DNA, evidenced by both experimental and modeling data.⁶¹ Groove binders may be sequence-specific, as different nucleoside combinations have different groove dimensions and properties. **(c)** A cobalt complex that surface stacks on DNA via electrostatic interactions, while the free ligand is an intercalator.⁵⁵ While electrostatic interactions are weaker than intercalation and groove binding interactions, surface stackers can still cause DNA cleavage and cytotoxicity.

For most metal complex-DNA interactions it is difficult to predict specific binding mode based on structure alone. Intercalators are nearly ubiquitously square planar or octahedral

complexes with aromatic ligand systems.⁶⁴ Planarity is necessary to meet the steric requirements of intercalation, while aromaticity supplies favorable π - π interactions with base pairs.⁶⁴ One such complex is an octahedral Co(II) coordination polymer (Figure 4a), where each planar aromatic ligand coordinates to the Co(II) center in the next subunit.⁵⁷ Despite the unique polymeric nature of the complex, an intercalative binding mode was confirmed with electronic absorption, fluorescence titration, and EtBr displacement. Moreover, the polymeric complex binds DNA more tightly than does free ligand ($K_b = 5.95 \times 10^5 \text{ M}^{-1}$ versus $2.59 \times 10^4 \text{ M}^{-1}$). The polymer also displayed toxicity against all four cancerous cell lines tested (HeLa, HEp-2, Hep G2, and A431), comparable to or exceeding the toxicity of cisplatin, while showing 100-fold lower toxicity against non-cancerous NIH/3T3 cells.⁵⁷ This study demonstrates that *polymeric* planar aromatic complexes can act as intercalators, and show preferential toxicity in cancerous versus non-cancerous cell lines.

A comparable dinuclear Co(II) complex is an intercalator that was confirmed by viscosity, electronic absorption, and fluorescence titration.⁶⁵ The study performed a head-to-head comparison of the dinuclear Co(II) complex versus a mononuclear Zn(II) complex with the same ligand. The Co(II) complex had a higher K_b than the zinc complex or the free ligand ($K_b = 8.02 \times 10^5 \text{ M}^{-1}$, $4.51 \times 10^5 \text{ M}^{-1}$, and $1.60 \times 10^5 \text{ M}^{-1}$, respectively). DNA cleavage was investigated using gel electrophoresis, and the Co(II) complex showed highest cleavage activity, likely due to higher Lewis acidity of the metal center.⁶⁵ Thus, Lewis acidity should be taken into consideration when designing metal complexes for interaction with DNA.

Unlike intercalators, major and minor groove binders of DNA are often sequence-dependent given that groove dimensions and presenting functional groups vary among the nucleoside base pairings.⁶⁶ For this reason, molecular docking simulations are often used as

verification of groove binding. An octahedral Co(II) complex (Figure 4b) is proposed to strongly bind DNA in the minor groove ($K_b = 3.29 \times 10^5 \text{ mol}^{-1} \text{ dm}$) based on electronic absorption, fluorescence titration, and CD.⁶¹ Molecular docking experiments confirm minor groove binding with the double stranded DNA sequence CGCGAATTCGCG. The complex correspondingly exhibits significant *in vitro* cytotoxicity against three human cancer cell lines ($IC_{50} = 7, 13, \text{ and } 25 \text{ }\mu\text{g/mL}$ against T cell leukemia, ovarian adenocarcinoma, and glioblastoma cells) and only moderate toxicity against noncancerous cells ($IC_{50} > 100 \text{ }\mu\text{g/mL}$).⁶¹ A Co(II) hydrazone complex and its Ni(II) analog were found to be groove binders, but major vs. minor groove binding could not be determined.⁶⁷ Viscosity, electronic absorption, fluorescence titration, and CD all confirmed a groove binding mechanism. The K_b values for the Co(II) and Ni(II) complex were $0.89 \times 10^5 \text{ M}^{-1}$ and $2.2 \times 10^5 \text{ M}^{-1}$ respectively, indicating that the Co(II) complex bound with lower affinity than the Ni(II) complex.⁶⁷ While the sequence specificity of groove binders limits their DNA strand interactions, this has not been shown to negatively impact their cytotoxicity.

Metal complexes that interact with DNA electrostatically via surface stacking are usually driven by *weak* π - π interactions. Based on structure alone, it is difficult to predict metal complexes that preferentially surface stack rather than intercalate as both contain aromaticity. One study found a Co(II)-Schiff base (Figure 4c) to interact with DNA electrostatically, while the same free ligand acted as an intercalator.⁵⁵ The binding modes of both the ligand and the complex were verified with viscosity, electronic absorption, fluorescence titration, and CD, and DNA cleavage was evaluated with gel electrophoresis. As expected, the intercalating free ligand had a higher DNA binding affinity ($K_b = 8.5 \times 10^5 \text{ M}^{-1}$) than the complex ($K_b = 5 \times 10^4 \text{ M}^{-1}$).⁵⁵ Another study investigated a series of Co(II) and Co(III) hydrazone complexes for DNA binding and found all to interact via a surface mechanism, with a K_b range of 1.15 to $5.06 \times 10^4 \text{ M}^{-1}$.⁶² The mechanism was

substantiated with electronic absorption, fluorescence titration, EtBr displacement, and CD. Notably, all complexes in the series efficiently cleaved DNA in the presence of hydrogen peroxide and the reducing agent 2-mercaptoethanol, demonstrating that a complex needs not have high binding affinity in order to cleave DNA.⁶² Complexes that surface stack on DNA, therefore, have potential as cytotoxic anticancer agents.

1.4.2. Histidine-Targeted Cobalt-Schiff Bases

Inspired by the remarkable biological activity of CTC-96 (see Section 1.3), the Meade group has been investigating $[\text{Co}(\text{acacen})\text{L}_2]^+$ complexes as targeted agents in cancer biology. In this context, further mechanistic investigations have enabled rational design of agents for targeting specific proteins and biological pathways. In particular, ZFTF proteins are a target of high interest for cancer research, and they can be specifically inhibited using $[\text{Co}(\text{acacen})\text{L}_2]^+$ complexes. Section 1.4.2.1 will review what is known of the mechanism of inhibition, and Section 1.4.2.2 will discuss *in vitro* and *in vivo* biological studies that demonstrate specificity.

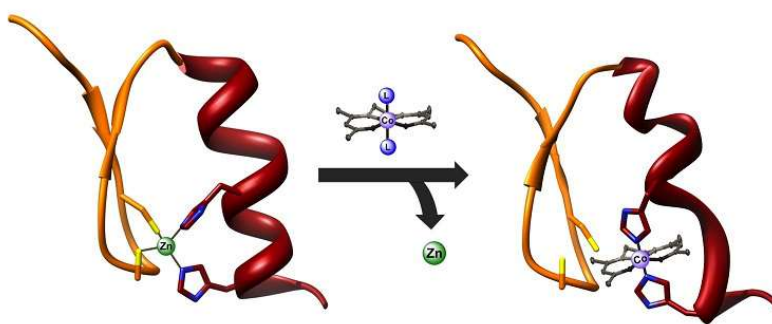


Figure 5. Proposed mechanism of inhibition of ZFTFs by $\text{Co}(\text{acacen})$. The complex coordinates to His residues in Cys_2His_2 zinc finger motifs through dissociative ligand exchange of axial ligands. Octahedral $\text{Co}(\text{acacen})$ displaces tetrahedrally coordinated $\text{Zn}(\text{II})$, disrupting protein structure and DNA binding function.⁴⁶

1.4.2.1. Investigating Mechanism of Action

$[\text{Co}(\text{acacen})\text{L}_2]^+$ complexes selectively inhibit the activities of histidine-containing proteins through dissociative exchange of the labile axial ligands.^{45,48} Therefore, the kinetic and thermodynamic ligand exchange dynamics are important considerations in the rational design of metal-based therapeutics.^{45,68} There is a direct correlation between the observed axial ligand lability of the $[\text{Co}(\text{acacen})\text{L}_2]^+$ derivatives and their ability to inhibit histidine-containing proteins.^{42,44,69–71} Exploiting these findings, inhibitors of Cys₂His₂ ZFTFs have been developed using ammine (NH₃) axial ligands ($[\text{Co}(\text{acacen})(\text{NH}_3)_2]^+$ hereafter termed “Co(acacen)”).

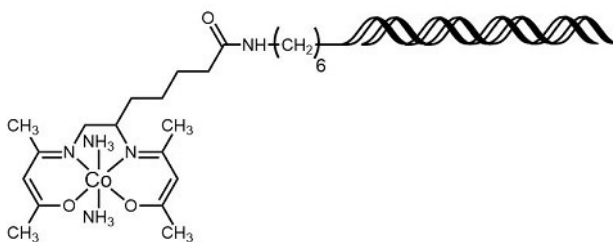


Figure 6. Co(acacen) conjugated to DNA, termed Co(III)-DNA. By conjugating the DNA consensus sequence of particular ZFTF, specific and potent inhibition can be achieved in cells and *in vivo*. The DNA serves as a reversible targeting moiety, while Co(acacen) provides irreversible protein inhibition.

The key roles that ZFTFs play in oncogenesis, tumor proliferation and growth, and metastasis make them highly desirable targets for therapeutic intervention.⁷² A lack of hydrophobic binding pockets makes these proteins difficult to target with traditional organic molecules, but their coordination chemistry can be exploited for potential therapeutic effect.⁷³ A large class of ZFTFs tetrahedrally coordinate Zn(II) ions through a Cys₂His₂ structural motif. Moreover, Zn(II) coordination is required for sequence-specific DNA recognition and gene regulatory function.⁷⁴ Octahedral Co(acacen) complexes are able to displace Zn(II) and bind to the Cys₂His₂ domain,

thereby disrupting protein structure and impairing DNA recognition and transcriptional activity (Figure 5). Since ZFTFs bind their consensus DNA with sequence-specificity, selective targeting can be achieved by conjugating Co(acacen) to oligonucleotides with high affinity for the protein of interest (Figure 6).^{69–71}

To further investigate the mechanism of ZFTF inhibition, model peptides of the zinc finger motif were treated with Co(acacen) and monitored by ¹H NMR and 2D NMR spectroscopy.⁴⁶ Upon treatment with the complex, protons of His residues *but no other residues in the peptides* underwent significant changes in ¹H resonances (>1 ppm) (Figure 7). CD and electronic absorption studies provided confirmation of structural perturbations of the zinc finger motif, supporting the hypothesis that the octahedral Co(III) complex distorts the tetrahedral Zn(II) binding pocket and therefore the local secondary structure. Taken together, these data reveal Co(acacen) complexes inhibit the activity of ZFTFs by coordinating His residues in the zinc finger domain via dissociative ligand exchange, thereby disrupting the structure required for gene regulation.⁴⁶

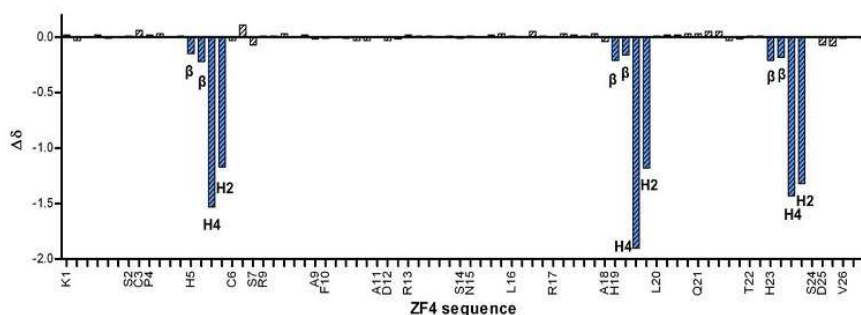


Figure 7. NMR data showing the specific binding of Co-acacen to His residues in ZFTF model peptides. Upon treating a ZFTF model peptide (KSCPH CSRAF ADRSN LRAHL QTHSD V) with Co-acacen, the change in resonances of protons in the amino acid side chain were recorded. The $\Delta\delta$ Chemical Shift profile demonstrates Co(acacen)'s selectivity for His residues, as significant effects were only observed on the His imidazole ¹H.⁴⁶

1.4.2.2. Investigating *In Vitro* and *In Vivo* Biological Activity

Specific inhibition of transcription factors has been achieved by employing a targeting method (Figure 6) where the conjugated oligonucleotide mimics the native binding partner of the protein (targeted complexes termed “Co(III)-DNA”).⁶⁹ The remarkable effectiveness of these agents has been demonstrated *in vivo* with inhibition of the Snail and Ci transcription factors in *Xenopus* and *Drosophila* embryonic models, respectively.^{70,71,75} Inhibiting Snail transcription factors may have a direct impact on epithelial-to-mesenchymal transition (EMT), thought to be a key factor in driving cancer metastasis. Ci transcription factor is the *Drosophila* analog of human Gli proteins, which are known oncogenes for a variety of cancers.

Co(III)-DNA containing the Ebox DNA sequence (Co(III)-Ebox) binds selectively and irreversibly to Snail ZFTFs.⁶⁹ Specificity of binding was investigated using electrophoretic mobility shift assays (EMSA) in *X. laevis* embryo lysates. After overexpressing various control proteins in embryos, the resulting lysates were challenged with ³²P-labeled probes. Co(III)-Ebox bound to the Snail family proteins (Snail1, Snail2, and Sip1), but did not bind a *non-Snail* family ZFTF, a *non-ZFTF* that binds Ebox, or a *non-ZFTF/non-Ebox binding* protein. To investigate the irreversibility of inhibition, ³²P-labeled Co(III)-Ebox was incubated with lysates overexpressing Snail2 protein and challenged with an unlabeled control. Co(III)-Ebox remained bound to Snail2 even after being challenged with 100-fold unlabeled Ebox, while the same ³²P-labeled Ebox without Co(acacen) was displaced after being challenged by 33-fold unlabeled Ebox.⁶⁹

Co(III)-Ebox was subsequently tested *in vivo* with *X. laevis* embryos at varying stages of development to demonstrate its utility in live animals (Figure 8a).⁷⁰ Co(III)-Ebox successfully inhibited known functions of Snail in the formation of neural crest cells and inhibited their migration. Specificity was demonstrated by a series of controls as well as retention of normal

development of the central nervous system and mesoderm formation.⁷⁰ Snail ZFTFs have been linked to the formation of cancer stem cells and mediate EMT, making cancer cells more invasive and migratory. The ability to inhibit Snail ZFTFs *in vivo* is a superb tool for better understanding Snail's roles in cancer, and targeted Co(acacen) complexes hold therapeutic promise as potential metastasis inhibitors.

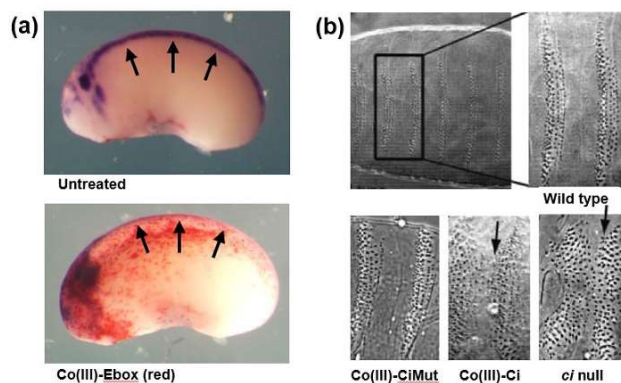


Figure 8. (a) *X. laevis* embryos treated with Co(III)-Ebox show dramatically impaired neural crest formation and migration. Embryos were injected with Co(III)-Ebox prior to neural crest migration. At stage 25 of embryo development, untreated (top) versus treated (bottom) embryos show that Co(III)-Ebox results in failure of the neural crest cells to migrate. *In situ* hybridization of Twist expression visualizes neural crest formation and cell migration with blue stain, while Co(III)-Ebox is stained red. Normal neural crest development is seen in untreated embryos, while little to no neural crest migration is observed in treated embryos, indicated with black arrows. For related work see ref ⁷⁰. (b) Co(III)-Ci inhibits Ci ZFTF function in *D. melanogaster* embryos. Embryos treated with Co(III)-Ci show impaired denticle belt formation relative to the untreated control and Co(III)-CiMut. Co(III)-Ci treatments mimics the phenotype of Ci null embryos, indicating that the conjugate disrupts the associated pathway through inhibiting the Ci ZFTF.⁷¹

Similarly, a Co(acacen) complex targeted to Ci (cubitus interruptus) ZFTF protein (complex termed Co(III)-Ci) was synthesized and tested *in vitro* and in a *Drosophila* embryo model.⁷¹ The ability of Co(III)-Ci to inhibit Ci from binding its DNA target was evaluated *in vitro* with protein extracts and *D. melanogaster* cells (S2 cells). Consistent with the results of Co(III)-

Ebox studies in *X. laevis*, Co(III)-Ci demonstrated potent and specific inhibition of its ZFTF target. Moreover, mutating the targeting sequence by one base pair or replacing it with a different sequence altogether precluded inhibition of DNA binding by Ci. Live cell studies demonstrated inhibition as well, wherein a luciferase reporter gene for Ci's target pathway was used. Co(III)-Ci was able to significantly decrease transcriptional activation by Ci.⁷¹ This is a highly significant result demonstrating the utility of the Co(III)-DNA platform for broader applications. By simply changing the DNA sequence, the strategy can be used for a number of other cancer-associated ZFTF proteins.

Next, *in vivo* studies in developing *D. melanogaster* embryos were performed. In these embryos, Ci plays a major role in denticle belt formation, and genetically mutated *ci*⁹⁴ null exhibits abnormal fusion of the segments. Treatment of embryos with Co(III)-Ci resulted in localized fusion where the agent was injected, mimicking the *ci*⁹⁴ null phenotype (Figure 8b).⁷¹ In a complementary experiment, in which Ci is truncated into its repressor form but retains its ZF binding domain and sequence-specific DNA recognition, Co(III)-Ci could rescue denticle belt segmentation. This demonstrates that Co(III)-Ci can selectively inhibit Ci in both its activator or repressor form in an *in vivo* embryo model.⁷¹

These biological investigations lay the groundwork for significant advances in the field of targeted cancer therapeutics. Both ZFTFs for which selective inhibition has been demonstrated (Snail family and Ci) are implicated in cancer-associated pathways. Overactivity of Snail proteins has been linked to EMT in cancer metastasis, while Ci regulates the hedgehog pathway associated with basal cell carcinoma and medulloblastoma. However, the modularity of the Co(III)-DNA platform allows for targeting of any ZFTF, granting the platform much broader applicability.

CHAPTER 2: HEDGEHOG PATHWAY STUDIES IN MAMMALIAN CELLS

2.1. Background, Hedgehog Pathway

The Hedgehog (Hh) pathway is implicated in a variety of cancers, but is most heavily linked to basal cell carcinoma (BCC), medulloblastoma (MB).⁷⁶⁻⁷⁹ In recent years, the Hh pathway has become a highly desirable target for therapeutic intervention.^{80,81} The mammalian pathway (Figure 9) consists of a family of Hh signaling proteins including sonic hedgehog (Shh), desert hedgehog, and indian hedgehog, the two transmembrane proteins patched (Ptch) and smoothened (Smo), several Gli-associated proteins (not shown), and a family of Gli transcription factors.⁸²⁻⁸⁴ The Gli family transcription factors Gli1, Gli2, and Gli3 serve as transcription repressors in their truncated form (Gli_R) and as transcription activators in their full-length form (Gli_A).^{85,86} Gli1 and Gli2 are most likely to be found in Gli_A form, while Gli3 is most likely to be found in Gli_R form.⁸⁷

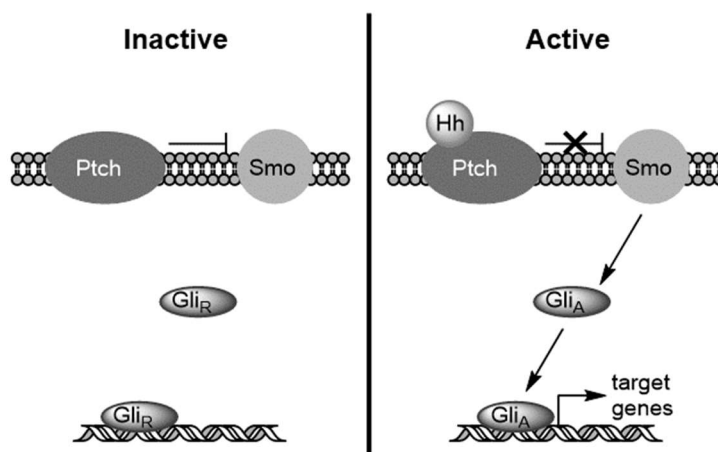


Figure 9. Simplified scheme of Hh pathway without (left) and with (right) Hh ligand-induced signaling. Under normal, inactive conditions the 12-pass transmembrane protein Patched (PTCH) suppresses Smoothened (SMO) and downstream activity. Gli remains in its full-length repressor forms. Under oncologic, overactive conditions suppression of SMO is relieved, allowing for activation of Gli-associated proteins and eventual truncation of Gli into activator forms.

Pathway signaling is initiated by Hh ligand binding to Ptch in the primary cilium; suppression of Smo is then relieved and the downstream pathway is activated.⁸⁸

While Hedgehog signal transduction has been implicated as a contributing factor in a number of tumors, activation of the Gli1 and Gli2 transcription factors by Hh signaling has only been shown to *directly* drive tumor formation in BCC and a subset of MBs.⁷⁷ In keeping with this observation, complexes targeting the Smo protein have shown efficacy in BCC and MB, but have been less effective in other tumors in which the Hh pathway has been implicated. While background on both BCC and MB will be given, BCC is the focus of the presented work, as it provides an excellent context in which to test and refine new complexes and is more physiologically accessible. By investigating delivery and inhibition in the BCC model, these approaches could ultimately be applied to the deadlier and more clinically challenging context of MB.

2.1.1. Hedgehog Pathway and Basal Cell Carcinoma (BCC)

BCC, a tumorous skin cancer usually found on the head and neck, is the most commonly diagnosed cancer. It represents 75% of non-melanoma cases of skin cancer, and 3 in 10 Caucasians will have it in their lifetime.⁸⁹ These cancers rarely metastasize, so the standard treatment method is to surgically excise the entire tumor, which is effective but leaves scarring. Some topical treatments are in clinical use but have not yet gained the same popularity as surgical removal because they are less effective.⁸⁹ A topical treatment that reduces or eliminates BCC tumors successfully would therefore be highly desirable.

BCC tumors are linked to UV exposure and are almost always associated with overactive signaling of the Hedgehog (Hh) pathway.⁹⁰ Thus, development of Hh pathway inhibitors is at the

forefront of BCC-related research. The 7-pass transmembrane protein Smo has thus far proven to be the most “druggable” target in the pathway. A number of small molecule Smo inhibitors are known, including the FDA-approved Vismodegib.⁹¹ However, the Hh pathway can develop resistance to inhibitors via de novo mutations in Smo, amplification of *Gli2* gene, drug efflux by P-glycoprotein, or a number of other downstream interactions, rendering inhibitors ineffective.^{92,93} Clinically, these forms of resistance result in initial tumor shrinkage but ultimate regrowth. This problem has been successfully addressed in mice by targeting the final step in the Hh pathway, Gli zinc finger transcription factor (TF), in conjunction with Smo targeting.^{94,95} More options for Gli inhibitors that address problems of specificity and binding affinity need to be developed in order to increase the likelihood of translation to clinical use.

2.1.2. Hedgehog Pathway and Medulloblastoma (MB)

MB is the most common malignant pediatric brain tumor and represents one of the leading causes of tumor-related death in children.⁹⁶ The annual incidence is higher in children in the first decade of life and significantly higher in males than females.⁹⁷ Current treatment involves surgery followed by craniospinal radiation and/or cytotoxic chemotherapy. Despite multimodal treatment, one-third of patients still succumb to this disease.⁹⁸ Patients that do survive often suffer from devastating consequences, including cognitive deficits and endocrine disorders, which are secondary to both disease and therapy.⁹⁹

Historically, MB has been histologically classified into classic, desmoplastic/nodular, extensive nodularity, and large cell/anaplastic groups.⁹⁸ However, recent studies have demonstrated that MB can also be divided into molecular subgroups, each characterized by distinct genetic alterations, clinical features, and outcomes.¹⁰⁰ The recently published revised fourth

edition of the World Health Organization (WHO) Classification of Tumors of the Central Nervous System discriminates MBs into wingless (WNT), sonic hedgehog (SHH)-TP53-mutant, SHH-TP53-wildtype, and non-WNT/non-SHH groups, which includes extensive nodularity and large cell/anaplastic groups.¹⁰¹ Relapse and leptomeningeal dissemination still pose great challenges and relapsed patients often succumb to their disease due to the absence of curative strategies.⁹⁸

Although survival has improved significantly, the effects of therapy often lead to long-term sequelae.⁹⁸ In addition, therapeutic strategies for MB relapse are lacking. Therefore, more effective and less toxic therapies are urgently required to treat this disease. Identification of tumor subgroup status now allows for development of treatment protocols tailored toward each subgroup and thus sets the stage for trials of new targeted therapies. In particular the Shh-driven subtypes pose an opportunity for pathway-specific intervention, making the Hh pathway a highly desirable therapeutic target.

2.2. Approach for Hedgehog Pathway Inhibition

A critical barrier to progress in developing a Gli inhibitor is that zinc finger TFs are very difficult to target due to lack of hot spots or deep binding sites.¹⁰² These proteins bind to specific regions of DNA, causing or blocking expression of the corresponding gene. Methods to inhibit zinc finger TFs have included decoy oligonucleotides¹⁰³ and peptide aptamers¹⁰⁴ that bind to the TFs and prevent DNA binding, or artificial transcription factors^{105,106} and transcription factor displacers¹⁰⁷ that interfere with the TF binding site on DNA. The primary limitation of these methods is that the binding is reversible, with similar affinities to that of the natural DNA/TF interaction. Thus, large concentrations of the agent are required to achieve the desired inhibition. Accordingly, current Gli inhibitors require large (micromolar) concentrations in order to be

effective.^{108,109} Moreover, specificity of Gli inhibitors needs to be improved, as exemplified by the known off-target effects of a well-studied Gli inhibitor, arsenic trioxide, which activates JNK and p38 MAPK pathways.¹⁰⁹

To overcome the limitations of low binding affinity and low specificity for zinc finger TFs, the Meade lab has developed a series of highly specific transition metal inhibitors that bind to their target irreversibly.⁶⁹⁻⁷¹ As described in section 1.4.2, these inhibitors consist of a cobalt(III)-Schiff base complex (Co(acacenHA)) that irreversibly binds to histidine-containing enzymes where zinc is in the active site. By attaching the oligonucleotide binding sequence of a particular zinc finger TF, the entire complex is targeted to the protein of interest. This work utilizes CoGli (Figure 10) targeted to Gli proteins for investigations in the mammalian Hh pathway system.

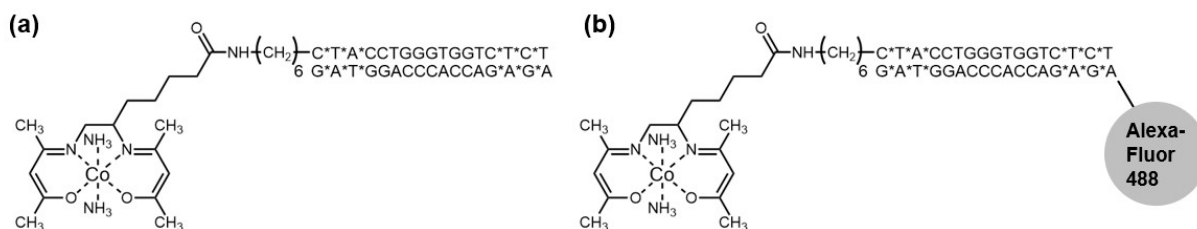


Figure 10. (a) CoGli, consisting of Co(acacenHA) coupled to Gli consensus sequence DNA 5'-GACCACCA-3', is used to investigate mammalian Hh pathway signaling. **(b)** CoGliFluor consists of CoGli coupled to AlexaFluor 488 dye and is used for visualization of CoGli in confocal microscopy and other studies.

This chapter will summarize work with CoGli in mammalian cells and systems delivered with transfection agents. Transfection agents are typically commercially available cationic agents that form liposome-like complexes around DNA and allow it to cross the cell membrane.¹¹⁰ A number of transfection agents have been used to deliver CoGli, including TurboFect, Lipofectamine 2000, Lipofectamine 3000, Lipofectamine LTX, PolyJet, and TurboJet.

Transfection agents are useful for studies in tissue culture but are typically associated with toxicity and are less effective *in vivo*.

CoGli was synthesized according to published protocols⁶⁹⁻⁷¹ with improvements to purification and characterization as described in **Appendix A**, **Appendix B**, and **Appendix C**. To prepare CoGliFluor, Gli consensus sequence DNA modified with AlexaFluor488 was purchased from IDT, then all synthesis proceeded according to the standard protocol with HPLC purification.

2.3. Specificity of CoGli *In Vitro*

An electrophoretic mobility shift assay (EMSA) is used to detect interactions between oligonucleotides and native proteins.¹¹¹ In a standard protocol, cell lysate and labeled oligonucleotide are incubated in a binding buffer then analyzed by gel electrophoresis. On the gel, free oligonucleotide is significantly more mobile than protein-bound oligonucleotide, resulting in two labeled bands on the gel as depicted in Figure 11. Specificity for the protein of interest can be assayed by competition with unlabeled consensus sequence DNA and unlabeled nonsense DNA.

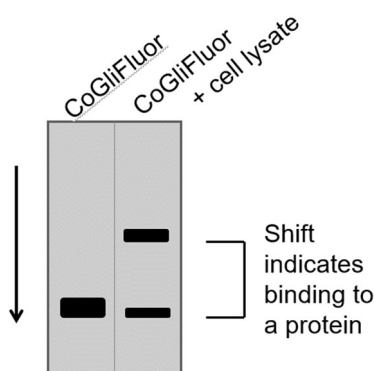


Figure 11. Depiction of EMSA experiment in which labeled DNA (CoGliFluor) is incubated with cell lysate containing the protein of interest. The appearance of a shifted band indicates a change in mobility of the labeled DNA due to being bound by a protein.

CoGliFluor was incubated with lysate from BSZ murine basal cell carcinoma cells for 3 h and analyzed by electrophoresis. Figure 12 shows that CoGliFluor is binding only one protein target; this strongly agrees with the hypothesis that CoGli targets Gli protein with high specificity. Moreover, competition with unlabeled Gli consensus sequence DNA provides compelling evidence that Gli is the identity of the protein being targeted. Upon adding 9-fold unlabeled Gli DNA competitor, the band intensity of protein-bound CoGliFluor is significantly decreased, indicating that it is being off-competed. However, when the competitor DNA sequence is mutated by just one base pair (GliMut DNA), the same concentration of unlabeled probe is unable to off-compete protein-bound CoGliFluor. Thus, Gli is likely the protein being targeted, rather than a nonspecific DNA-binding protein.

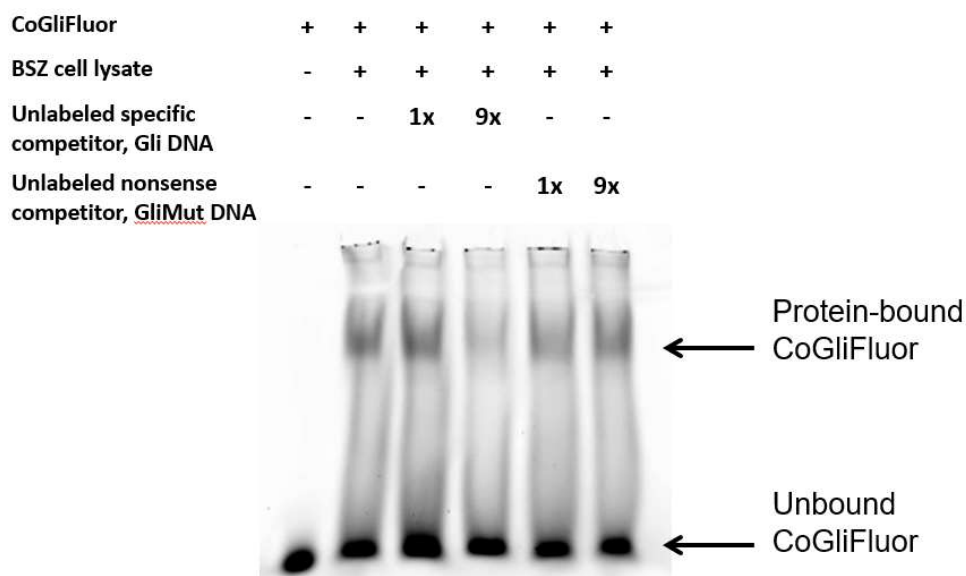


Figure 12. EMSA showing CoGliFluor binding its protein target. 9-fold unlabeled Gli consensus sequence DNA can off-compete CoGliFluor, while a one base pair mutation sequence (GliMut) is not. This strongly suggests binding of CoGliFluor to Gli protein.

2.4. Investigations in C3H/10T1/2 Cells

C3H/10T1/2 cells are pluripotent mouse embryonic fibroblasts. The fibroblasts differentiate into osteoblasts upon chemical induction of the Hh pathway. Osteoblasts have high level of alkaline phosphatase, detectable with a colorimetric assay. For this reason, these cells are commonly used to assay for Hh pathway inhibition.^{112,113} If Hh pathway inhibition is successful, cells will not differentiate into osteoblasts and little to no increase in alkaline phosphatase will be seen over the control. Cell morphology at low and high density can be seen in Figure 13.

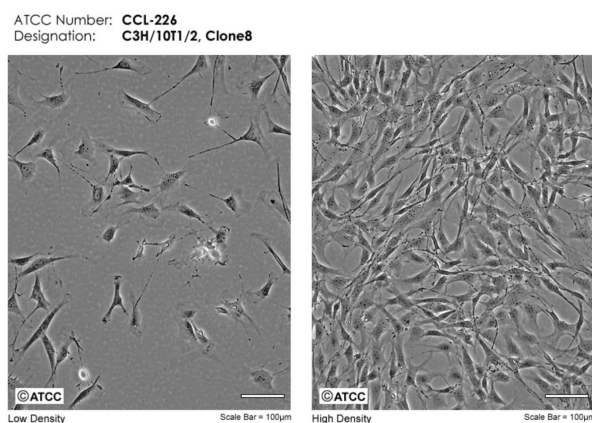


Figure 13. C3H/10T1/2 cell morphology at low and high density (©ATCC).¹¹⁴ Cells have the characteristic elongated shape of fibroblasts and are very sensitive to chemically-induced differentiation and post-confluence inhibition of cell division.

2.4.1. Hh Pathway Induction

The Hh pathway in C3H/10T1/2 cells can be induced using a small molecule smoothed agonist (SAG) or purified Shh protein. As shown in Figure 14, Shh was shown to be a more effective inducer under the conditions tested; however, SAG yields moderate induction and is significantly more cost-effective.

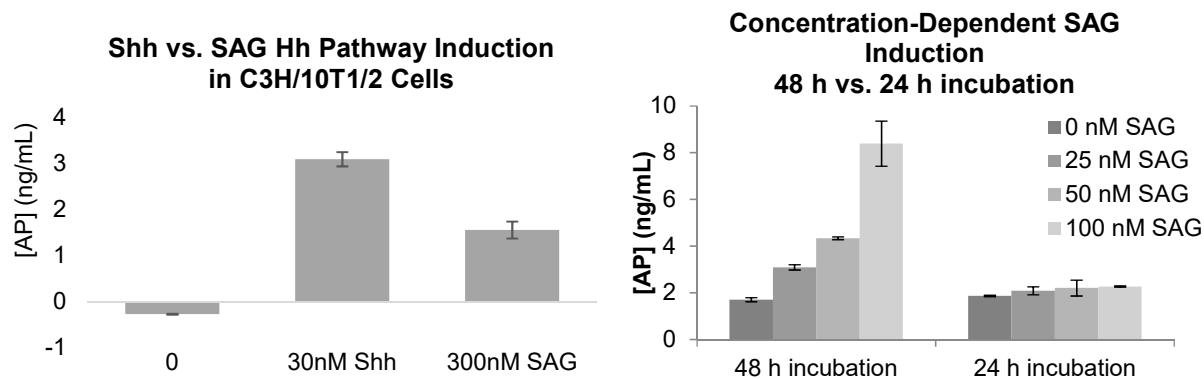


Figure 14. (a) Hh pathway induction in C3H/10T1/2 cells, as measured by an increase in the concentration of alkaline phosphatase. Over the non-treated control (“0”), Shh protein yields more significant induction than small molecule smoothed agonist SAG. **(b)** Concentration-dependent Hh pathway induction with 0-100nM SAG. Results demonstrate that an incubation time of at least 48 h with SAG is necessary for detectable differentiation into osteoblasts.

It is important to note that AP levels vary from passage to passage, even under identical conditions.

The cells are only recommended to be used from passages 5-15, but variations occur even within these parameters. This makes normalization across multiple studies challenging. For this reason, it is important to include positive and negative controls in every assay plate.

2.4.2. Hh Pathway Inhibition by CoGli

By treating C3H/10T1/2 cells with CoGli prior to Hh pathway induction, it is possible to prevent differentiation into osteoblasts. This demonstrates inhibition of the Hh pathway as postulated. Figure 15 shows inhibition with 150 nM CoGli transfected with Lipofectamine LTX or TurboFect. Both results are statistically significant at $p < 0.05$ when comparing against the induced negative control. Interestingly, a concentration-dependent response to CoGli was not observed, and 50 nM CoGli appears to slightly increase Hh signaling under both conditions.

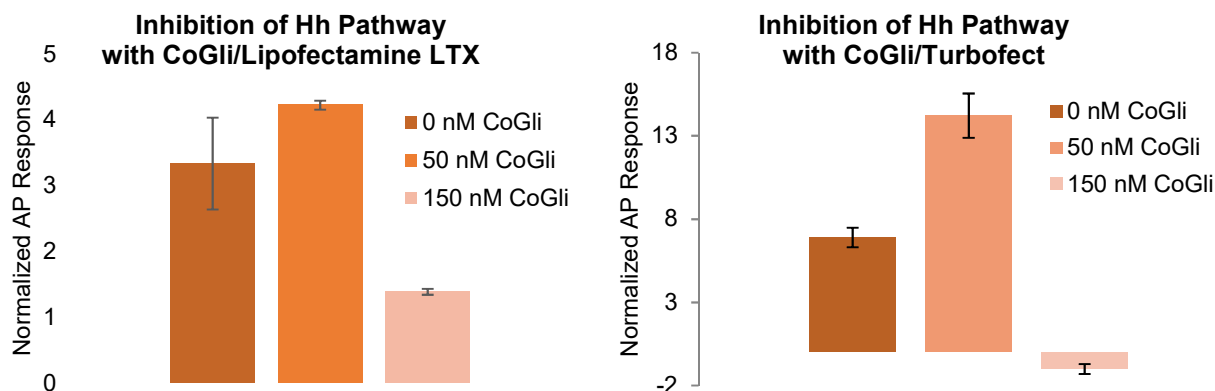


Figure 15. CoGli inhibits Hh-mediated differentiation of C3H/10T1/2 cells into osteoblasts with statistical significance at 150 nM. CoGli can be transfected using Lipofectamine LTX (left) or Turbofect (right) transfection agent. A concentration-dependent response is not observed, as 50 nM CoGli causes a slight increase in AP levels for both conditions.

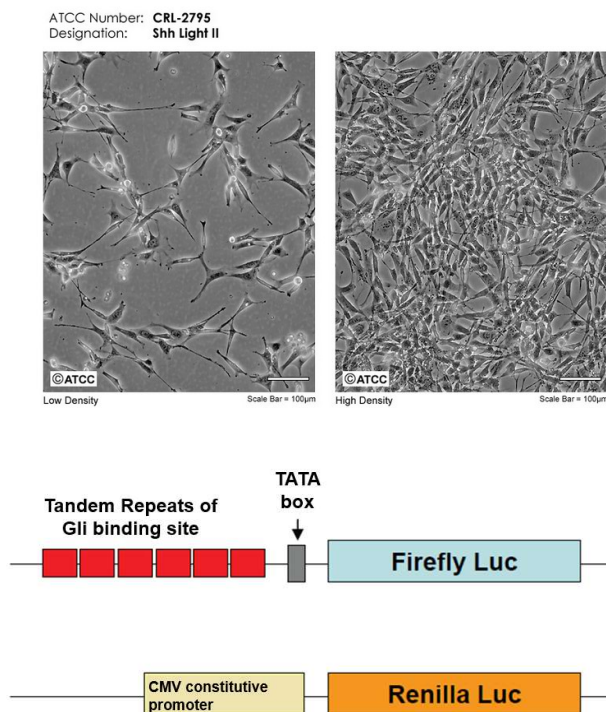


Figure 16. (top) NIH/3T3 Shh light II cell morphology at high and low density (©ATCC).¹¹⁵ Cells have the characteristic elongated shape of fibroblasts and are stably transfected with two luciferase proteins (bottom). The firefly luciferase gene is preceded by tandem repeats of Gli binding site DNA and a TATA box and is therefore expressed in response to Gli. The Renilla luciferase gene is constitutively expressed under the CMV promoter and is therefore used for normalization.

2.5. Investigations in NIH/3T3 Shh Light II Cells

NIH/3T3 Shh light II cells are regularly used to assay for small molecule-mediated Hh pathway induction and inhibition. The cell line is derived from NIH/3T3 cells (ATCC® CRL-1658) stably transfected with Gli-responsive firefly luciferase and the pRL-TK constitutive Renilla luciferase expression vector (Promega).^{87,115} By measuring luminescence of the Gli-responsive firefly luciferase and normalizing against luminescence of constitutively expressed Renilla luciferase, it is possible to determine relative Gli activity. Figure 16 shows cell morphology and a depiction of transfected luciferase genes.

2.5.1. Hh Pathway Induction

Typical Hh pathway induction in NIH/3T3 Shh light II cells is 2-3-fold from baseline with 30 nM Shh or 100 nM SAG. Unlike in C3H/10T1/2 studies, induction does not vary significantly from assay to assay. Hh pathway induction with Shh protein is concentration-dependent in the studied range, as shown in Figure 17. SAG (not shown) also induces in a concentration-dependent manner from 0-100 nM and is equally as effective at Hh pathway induction.

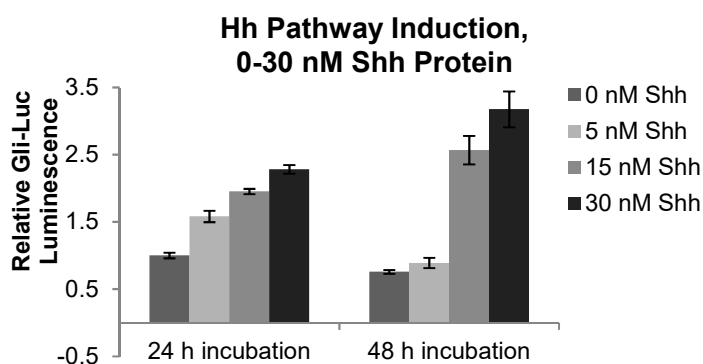


Figure 17. Hh pathway induction with 24 h and 48 h incubation of Shh protein in NIH/3T3 Shh light II cells. Induction is concentration-dependent in the range of 0-30 nM Shh, and is typically 2-4-fold from baseline levels. Results are normalized to 1 (baseline) for ease of estimating fold change.

2.5.2. *Hh Pathway Inhibition by CoGli, Not Conclusively Determined*

In total, five controls were generated and tested in biological assays, depicted in Figure 16. Co(acacenHA) (Figure 18.a.) is the untargeted inhibitory agent. It is possible for it to inhibit Gli proteins, but will also bind other available His residues and will act without specificity. For this reason, it is not expected to demonstrate Gli inhibition at concentrations similar to those of CoGli. Free dsGli consensus sequence DNA (Figure 18.b.) was also used as a control; as no inhibitory agent is present whatsoever, this is the most reliable negative control. It is important to include because transfection of DNA is a biologically harsh process for cells to undergo and may affect viability and assay outputs. CoGliMut1 and CoGliMut2 (Figure 18.c. and 18.d.) contain one and two base pair mutations, respectively, of the Gli consensus sequence. Sequences are GliMut1 (5'-CTACCTGGG**T**AGTCTCT-3') and GliMut2 (5'-CTACCTAGG**T**AGTCTCT-3'), with mutations indicated in bold. The mutated base pairs are known to be important for Gli recognition and binding, so altering them should negatively impact CoGli's ability to specifically inhibit Gli proteins. Co-PolyT (Figure 18.e.) contains a nonsense DNA sequence and should have no specificity for Gli proteins. As with CoGli, all controls utilized three flanking phosphorothioate linkages on either side to protect against degradation by nucleases.

Results for all control studies are shown in Figure 19. Contrary to expectations, all controls in which DNA was transfected (regardless of Co inhibitor) demonstrated a decrease in Gli-responsive luciferase signaling. Rather than being indicative of inhibition across the series, this suggests that NIH/3T3 Shh light II cells are not appropriate for our transfection-based studies.

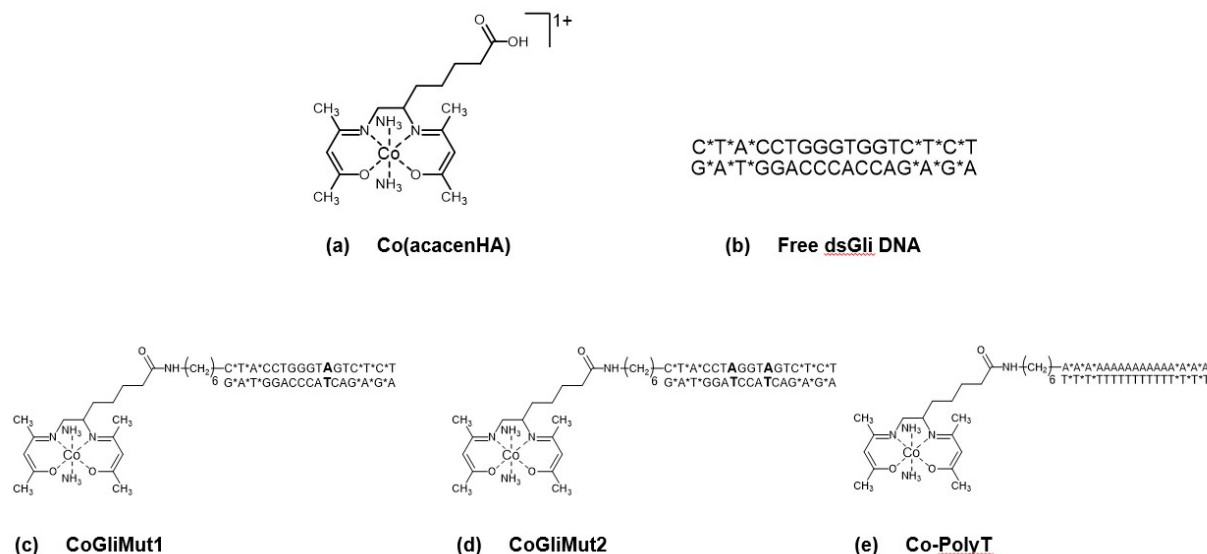


Figure 18. Five small molecule controls were synthesized for use in biological assays. **(a)** Co(acacenHA), the untargeted inhibitory agent. **(b)** Free dsGli consensus sequence DNA. As DNA alone does not inhibit Gli protein, this is not expected to have any biological effect. **(c)** CoGliMut1 has one mutated base pair at a site known to be important for Gli protein-DNA recognition and binding. **(d)** CoGliMut2 has two mutated base pairs at sites known to be important for Gli protein-DNA recognition and binding. **(e)** Co-PolyT consists of the inhibitory agent coupled to a nonsense DNA sequence. Gli family proteins are not known to bind this sequence, so no specificity is expected.

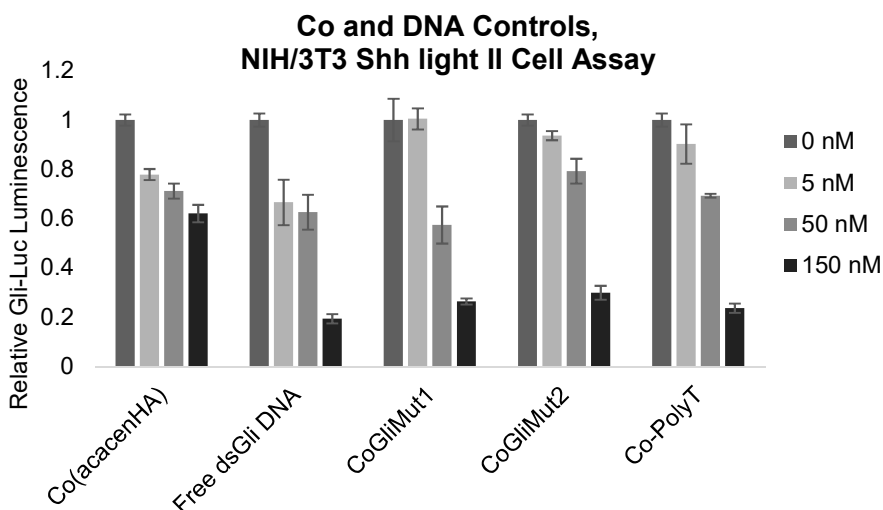


Figure 19. Small molecule Co- and DNA-based controls were tested in NIH/3T3 cells for Gli-responsive luminescence response. All controls for which DNA was transfected, even when no inhibitor was present, led to an apparent decrease in Gli signaling. These results suggest that this cell line is not appropriate for transfection-based studies.

2.5.3. Cell viability

Notably, the change in luciferase signaling is not due to toxicity of CoGli or transfection agent. A viability assay was carried out under identical conditions to the common treatment protocol. CoGli was transfected with Lipofectamine 2000 at concentrations of 10 nM to 10 μ M. Cells were also assayed with Lipofectamine 2000 alone and in the presence and absence of SAG. Figure 20 shows no significant decrease in cell viability was observed with increasing amounts of CoGli/Lipofectamine 2000 or Lipofectamine 2000 alone. However, all conditions showed 30% lower proliferation on average when compared against wells receiving SAG only in full serum conditions; this is unsurprising given that cells in full growth media will proliferate more. Study was performed with varying concentrations of Lipofectamine 2000, and no significant difference between treated and untreated wells was observed, suggesting little to no toxicity.

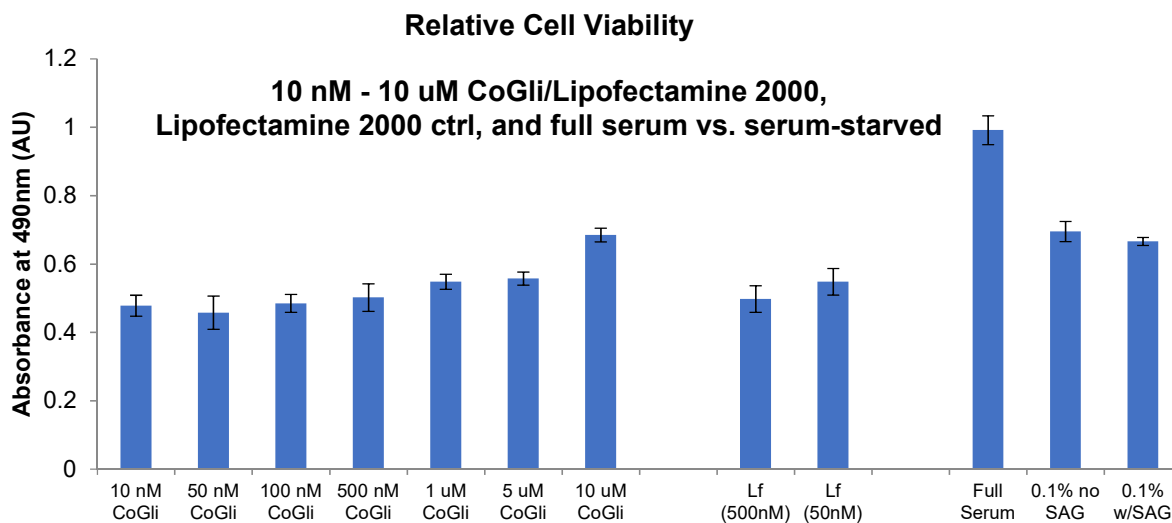


Figure 20. An MTS assay was used to measure relative cell viability for NIH/3T3 Shh light II cells treated with CoGli/Lipofectamine 2000, Lipofectamine 2000 alone, and SAG. No decrease in viability was seen up to 10 μ M CoGli/Lipofectamine 2000 transfection agent. The only statistically significant difference is between the cells treated in full growth media (10% FBS) and those that were not.

2.5.4. Confocal Microscopy

To visualize delivery of CoGli into NIH/3T3 Shh light II cells by various transfection agents, CoGliFluor was prepared and confocal microscopy was performed. Comparing against a negative control, transfection agents that utilize two different delivery mechanisms were investigated. TurboFect is a cationic polymer that forms positively charged complexes with DNA and has minimal toxicity compared to most lipid-based agents. The TurboFect/DNA complexes are endocytosed, and the proton sponge effect leads to endosomal rupture. Lipofectamine 2000 delivers DNA via lipofection, wherein it forms liposomes containing DNA and merges with the cell membrane.

Figure 21 shows that both transfection agents demonstrated at least modest delivery of CoGliFluor into cells over the negative control, along with modest colocalization with nuclear stain (z-stacks not shown). It is unknown whether colocalization with the nucleus is required for biological activity of CoGli given that Hh pathway signaling is initiated in the cytoplasm. Lipofectamine 2000 shows much higher CoGliFluor signal intensity than TurboFect, indicating that liposomal transfection agents are the preferred mechanism of transfection for NIH/3T3 Shh light II cells.

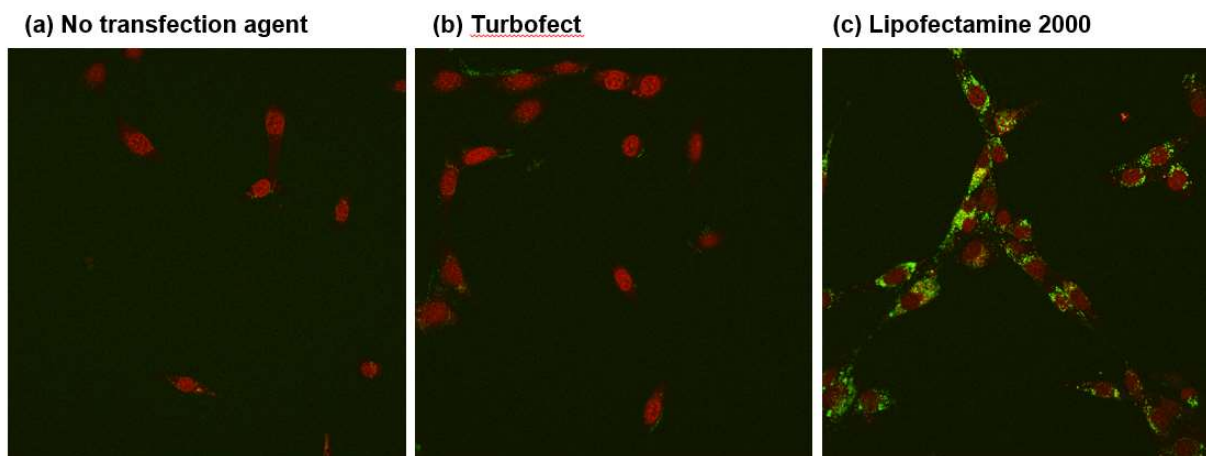


Figure 21. NIH/3T3 Shh light II cells were treated with CoGliFluor, transfected with **(a)** no transfection agent (negative control), **(b)** TurboFect, a polymeric transfection agent, or **(c)** Lipofectamine 2000, a cationic liposomal transfection agent. CoGliFluor is shown in green, while NucRed nuclear stain is shown in red.

2.6. qPCR in ASZ Cells

ASZ and BSZ are mouse basal cell carcinoma (BCC) cell lines. They have inherently high Hh pathway signaling and do not require induction. As keratinocytes are sensitive to calcium concentrations, calcium concentration in the growth media is carefully controlled. To measure Hh signaling levels, RT-qPCR was performed for Gli1 mRNA normalized to TUBB. The preliminary data (shown in Appendix D) suggest that CoGli, CoGliMut2, Co-PolyT, and 300 nM cyclopamine small molecule inhibitor all decrease Hh pathway signaling by 80%. Free dsDNA, however, causes no decrease. At the time of writing, the results are preliminary (n=1) and it is not clear whether inhibition by any of these agents is genuine. The assay will be repeated along with Co(acacenHA) at a variety of concentrations; lower concentrations may be required to observe specificity in this system.

2.7. Conclusions and Future Work

This chapter has introduced CoGli, a Hh pathway inhibitor for use in mammalian systems. CoGli can bind its protein target with specificity *in vitro* under native conditions as demonstrated with EMSA, and successfully inhibits the Hh pathway at nanomolar concentrations in C3H/10T1/2 cells. CoGli can be delivered into mammalian cells using several transfection agents; moderate cell toxicity is observed. Transfection agents also allow for delivery of CoGliFluor for visualization of CoGli in live cells.

Although the NIH/3T3 Shh light II cell line can be excluded from future studies with transfection agents, it is desirable to demonstrate Hh pathway inhibition in more than one cell system. Current work is ongoing to measure Hh pathway inhibition in ASZ murine BCC cells using qPCR for Gli1 mRNA. Preliminary results are shown in Appendix D. Future work could employ NIH/3T3 parent or HEK293 cells transfected with exogenous Gli-responsive luciferase. If reporters are co-transfected with CoGli simultaneously, it may be possible to avoid the DNA transfection issues experienced thus far.

Future work could also investigate the specificity of CoGli for Gli in live cell assays. Specifically, demonstrating Hh pathway inhibition independently of Smo would be highly desirable, as most current Hh pathway inhibitors act upon Smo. To study this, a constitutively activated Smo variant, SmoA1, could be upregulated to increase Hh pathway signaling. Smo-mediated upregulation of the Hh pathway is not expected to affect the inhibition of the Hh pathway by CoGli as it acts downstream of Smo. Moreover, a known mutant of Smo, SMOD477G, is resistant to known Hh-pathway inhibitors GDC-0449 and cyclopamine. SMOD477G could be expressed in cells, then resistance to GDC-0449 and cyclopamine demonstrated. CoGli should still be able to inhibit the Hh pathway in these cells, demonstrating inhibition in a model of drug-

resistant BCC.

To demonstrate targeting of Gli TFs directly, cells can be transfected with low concentrations of Gli expression constructs. Cells transfected with the constructs are expected to display a higher level of constitutive reporter activity as well as additional reporter activity inducible by treatment with Shh. The Smo inhibitor cyclopamine is known to only inhibit Shh-induced reporter activity.^{95,109} CoGli is expected to inhibit both Shh-inducible reporter activity as well as reporter activity resulting from constitutive expression of Gli. This would demonstrate that the activity of CoGli is a result of direct targeting of Gli TFs.

2.8. Materials and Methods

2.8.1. Electrophoretic Mobility Shift Assay (EMSA)

Culture method for BSZ cells can be found in section 2.7.4.1. and is identical to culture method for ASZ cells. BSZ cell lysate for use in EMSA experiments was prepared as follows. A 25 cm² flask of cells at 100% confluence was washed once then incubated at 37°C for 8 min with DPBS. After incubating, DPBS was aspirated and 0.5 mL passive lysis buffer (Promega E1941) was added. Flask was placed on a gentle rocker at 4°C for 15 min, then a cell scraper was used to detach any remaining cells. Flask contents were transferred to a microcentrifuge tube and transferred to a -80°C freezer for later use.

EMSA binding buffer for incubation of cell lysate with CoGliFluor contained 20 mM HEPES, 150 mM KCl, 3 mM MgCl₂, 0.5 mg/mL BSA, 0.2 mM ZnSO₄, and 10% glycerol (v/v). Note that the presence of ZnSO₄ is crucial for native zinc finger proteins to retain their structural integrity and DNA-binding ability. Gel electrophoreses were performed on a native gel containing

5% acrylamide. Tris borate EDTA (TBE) buffer was used for preparing gels (5X) and as mobile phase running buffer (0.5X). The 5X buffer contains 0.446 M Tris base, 0.444 M boric acid, and 0.01 M EDTA. If needed, pH should be adjusted to 8.3; however, the buffer should reach pH 8.3 without adjustment after stirring and allowing to equilibrate for 15 min. The gel was prepared with 7.6 mL mH_2O , 2.4 mL 5X TBE buffer, 2 mL 30% acrylamide, 25 μL 30% w/v ammonium persulfate (APS), and 5 μL TEMED. The stacking gel was prepared with 3.33 mL mH_2O , 1 mL TBE buffer, 0.667 mL 30% acrylamide, 25 μL 30% w/v APS, and 5 μL TEMED. The mobile phase running buffer was 0.5X TBE buffer.

A Pierce™ BCA Protein Assay Kit (ThermoFisher 23225) was used to determine protein concentration in BSZ lysate, and 12.8 μg protein were used per lane. The binding reaction was performed according to Scheme 1. Immediately after final addition at $t = 3\text{h } 20\text{m}$, gel was loaded and electrophoresed for 30 min at 130 V on a pre-charged gel. Fluorescent imaging of gels was performed on a Typhoon 9400 variable mode imager.

Scheme 1: EMSA Reaction Conditions and Legend

time	Lane 1	Lane 2	Lane 3	Lane 4	Lane 5	Lane 6
$t=0\text{ h}$		4 μL BSZ 1.5 μL dI/dC				
$t=15\text{min}$		4.5 μL CoGliFluor				
$t=3\text{h}$	4.5 μL CoGliFluor		0.34 μL unlab. Gli	2.8 μL unlab. Gli	0.24 μL unlab. GliMut1	2.2 μL unlab. GliMut1
$t=3\text{h}20\text{m}$	6 μL buffer	6 μL buffer	6 μL buffer	6 μL buffer	6 μL buffer	6 μL buffer

Name	Description	Concentration
BSZ	BSZ cell lysate	3.2 mg/mL protein
dI/dC	Nonspecific competitor	1 mg/mL
CoGliFluor	CoGli-AlexaFluor488	0.18 μM
Unlab. Gli	Unlabeled Gli consensus	3.4 μM

	sequence DNA	
Unlab GliMut1	Unlabeled Gli consensus sequence DNA with one base pair mutation	2.4 μ M
Buffer	EMSA binding buffer	(see text)

2.8.2. C3H/10T1/2 Cell Assays

2.8.2.1. Culture Method

C3H/10T1/2, Clone 8 cell line was purchased from ATCC® (Cat. No. CCL-226™). Per the catalog's recommendation, the cells were culture in Basal Medium Eagle (BME, Life Technologies 21010046) supplemented with 2 mM L-glutamine and 10% heat-inactivated (HI) FBS (5 mL L-glutamine and 50 mL HI-FBS per 500 mL media). HI-FBS was prepared by incubating FBS at 60°C for one hour. C3H/10T1/2 cells are highly sensitive to post-confluence inhibition of cell division, so care must be taken not to let the cells become confluent.

For assays, cells were plated at 15,000 cells/well in a 24 well plate in full growth media (day 1). On day 2, serum starvation was initiated (swap to BME with 0.1% HI-FBS), Hh pathway inducer was added, and CoGli was transfected. Inducer may be 30 nM Shh protein (R & D Systems 1845-SH-025, recombinant human sonic hedgehog/Shh C24II N-Terminus) or 100 nM SAG (Adipogen AG-CR1-3506). The chemical structure of SAG is shown in Figure 22. A variety of transfection agents were used to deliver CoGli, most commonly Lipofectamine LTX and Plus Reagent (ThermoFisher 15338030). On day 5, the alkaline phosphatase and total protein assays were performed.

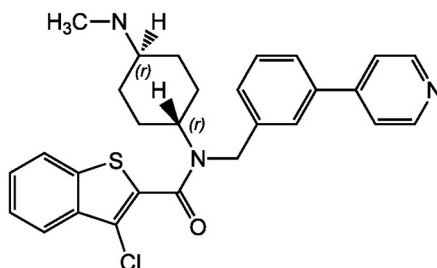


Figure 22. Smoothed agonist (SAG, CAS No. 912545-86-9) is a small molecule commonly used to induce Hh pathway signaling. Stock solutions of 5 mM were prepared in DMSO, then further dilutions for tissue culture dosing were prepared in water.

2.8.2.2. Alkaline Phosphatase Assay

AnaSpec AS-72146, SensoLyte® pNPP Alkaline Phosphatase Assay Kit was used to measure concentrations of alkaline phosphatase in C3H/10T1/2 samples. The assay was performed according to the manufacturer's protocol, with modifications to the preparation of cell extract and to assay volume. To prepare the cell extract, each well was washed twice with 1X assay buffer, then 100 μ L 1X assay buffer containing Triton X-100 (20 μ L per 10 mL 1X assay buffer) was added to each well. The plate was incubated at 4°C for 10 min with vigorous rocking. Cell lysate was then harvested by agitating with a micropipette using gentle scraping and rinsing and placed into a microcentrifuge tube on ice. After all wells were harvested, tubes were centrifuged at 2,500 x g for 10 min at 4°C. The supernatants were used for alkaline phosphatase and total protein assays. Assay volume was 35 μ L each for sample, alkaline phosphatase standard, and *p*-nitrophenyl phosphate (*p*NPP) substrate. Absorbance measurements at 490 nm were performed using a BioTek Synergy 4 multi-mode microplate reader.

2.8.2.3. Total Protein Assay

Pierce™ BCA Protein Assay Kit (ThermoFisher 23225) was used to measure total protein

in each C3H/10T1/2 sample for normalization of alkaline phosphatase levels. The assay was performed according to the manufacturer's protocol. Bovine serum albumin (BSA) solutions of 10 mg/mL to 0.25 mg/mL in water were prepared and used as protein calibration standards. Fresh standards were prepared monthly or as needed when quadratic fit was poor. Absorbance measurements at 562 nm were performed using a BioTek Synergy 4 multi-mode microplate reader.

2.8.3. NIH/3T3 Shh Light II Cell Assays

2.8.3.1. Culture Method

NIH/3T3 Shh light II cells were generously gifted by Prof. Bob Holmgren, and as of this writing are no longer available for purchase from ATCC®. If needed, it may be possible to obtain more cells from Prof. Bert Vogelstein (vogelbe@welch.jhu.edu, bertvog@gmail.com) at John's Hopkins University. The cells were cultured in DMEM supplemented with 4 mM L-glutamine, 0.4 mg/mL geneticin, 0.15 mg/mL zeocin, and 10% calf bovine serum (CBS).

2.8.3.2. Dual Luciferase Assay

For Dual Luciferase assays, cells were plated at 45,000 cells/well in a 24 well plate on day 1. On day 3, serum starvation was initiated (swap to 0.1% CBS DMEM), Hh pathway was induced with 30 nM SAG (Adipogen AG-CR1-3506), and CoGli was transfected. A variety of transfection agents were used to deliver CoGli, most commonly Lipofectamine LTX and Plus Reagent (ThermoFisher 15338030). On day 5, dual luciferase assay was performed.

Promega E1910, Dual-Luciferase® Reporter Assay System was used to measure Renilla and firefly luciferase levels in NIH/3T3 Shh Light II cells. Luminescence measurements were

performed using a BioTek Synergy 4 multi-mode microplate reader in luminescence mode. Cells were washed twice with DPBS, then harvested by incubating with 100 μ L/well 1X passive lysis buffer for 15 min at 4°C with rocking. Well contents were then agitated with a micropipette using gentle scraping and rinsing to harvest into microcentrifuge tubes. Tubes were centrifuged at 4°C on high speed for 2 min, then supernatant was used for assay. In a 96 well plate with opaque walls and bottom, 20 μ L cell lysate supernatant and 50 μ L luciferase assay reagent II (LAR II) were combined and first luminescence measurement was taken. Then 50 μ L Stop & Glo® was added to each well and second luminescence measurement was taken.

2.8.3.3. *MTS Assay for Cell Viability*

For cell viability assays, cells were plated at 12,000 cells/well in a 96 well plate (day 1). On day 2, serum starvation was initiated (swap to 0.1% CBS DMEM) and SAG was added to appropriate wells. On day 5, viability assay was performed.

CellTiter 96® AQueous One Solution Cell Proliferation Assay MTS (Promega G3582) was used to measure relative viability. Assay was performed according to manufacturer's protocol.

2.8.3.4. *Confocal Microscopy for Visualization of CoGliFluor Delivery*

For confocal experiments, NIH/3T3 Shh light II cells were plated in glass bottom dishes (WPI World Precision Instrument FD3510-100) at a density of 30,000 cells/0.5 mL. 24 h after plating, cells were treated with CoGliFluor/transfection agent. Imaging was performed on a Zeiss LSM510 Inverted Confocal microscope at various time point after treatment. One drop per 0.5 mL Nuclear stain NucRed™ Live 647 ReadyProbes™ Reagent (R37106) was added to wells 15 minutes prior to final imaging time point.

2.8.4. qPCR in ASZ cells

2.8.4.1. Culture Method: ASZ and BSZ

ASZ and BSZ cells were purchased from Northwestern's Skin Disease Research Center, Skin Tissue Engineering Core. Cells were cultured in 154CF media (ThermoFisher M154CF500) containing 2% chelexed, heat-inactivated FBS, 0.05 mM calcium chloride, and 1X Pen-Strep. The protocol to chelex FBS can be found in Appendix E. The culture method for these cells differs from most; this protocol can be found in Appendix F.

2.8.4.2. qPCR Culture Method and Primers

For qPCR experiments, ASZ cells were plated at 100,000 cells/well in a 12 well plate in serum starved conditions (0.2% chelexed FBS) on day 1. On day 3, cells were treated with CoGli or other agent; note the ASZ cells need not be induced as Hh pathway signaling is already high in BCC cells. On Day 5, cells were harvested for qPCR by washing 2x in DPBS then adding 200 μ L TRIzol™ reagent (ThermoFisher 15596026) per well and transferring to microcentrifuge tubes. For proper cell growth, cells should be plated in 1 mL media/well on day 1 but can be swapped to 500 μ L media/well on day 3 for conservation of agent.

After cell harvesting, the remaining qPCR protocol and analysis was carried out by collaborator Bethany Sump in the lab of Prof. Jason Brickner.

qPCR primers were purchased from IDT as custom oligos with standard desalting purification. The primer sequences (written 5' to 3') are shown below. Mouse GLI1 was the output gene of interest, while TUBB and GAPDH were used for normalization. Note that GAPDH is

sometimes regulated in keratinocytes and should therefore not typically be used without a secondary reference gene.

Mouse GLI1 primers

Forward: CGCGGGCAGCACTGAGGACTTGTC

Reverse: GCAGGTGTGAGGCCAGGTAGTGACGATG

Mouse TUBB primers

Forward: CAGGCCGGACAGTGTGGCAAC

Reverse: GGCTTCATTATAGTACACAGAGATTCG

Mouse GAPDH primers

Forward: TCACCACCATGGAGAAGGC

Reverse: GCTAAGCAGTTGGTGGTGCA

CHAPTER 3: NANO CONSTRUCTS FOR CELLULAR DELIVERY OF CO-DNA

A major problem faced by Co-DNA conjugates (Co-DNA) is their limited cell permeability due to the negatively charged oligonucleotide. Since Gli and other TFs are activated within the cytoplasm, cell permeability must be achieved for Co-DNA inhibitors to act as viable protein inhibitors. Previous work has studied Co-DNA conjugates transfected into cells for *in vitro* work, or injected directly into animal embryos at various stages of development for *in vivo* work.⁶⁹⁻⁷¹ To address this issue, this work presents two nanoparticle delivery vehicles for Co-DNA into mammalian cells and tissues: DNA-functionalized spherical gold nanoparticles (AuNP) and graphene oxide nanosheets (GO). The work presented here can be applied to investigation of other zinc finger-mediated disease pathways, greatly expanding the potential for use of Co-DNA complexes *in vitro* and *in vivo*.

3.1. DNA-Functionalized Spherical Gold Nanoparticles (AuNP)

3.1.1. Background and Design of Nano Construct

Spherical oligonucleotide-functionalized gold nanoparticles (AuNP) have shown remarkable success in delivering oligonucleotides into live cells and mammals with minimal toxicity.¹¹⁶⁻¹¹⁸ Commonly used for gene regulation via RNA interference or antisense oligonucleotide delivery, spherical nucleic acids (SNAs) have been studied extensively in preclinical and clinical trials for a variety of indications.¹¹⁹⁻¹²¹ Of particular interest to the present work, SNAs have been used successfully to locally deliver oligonucleotides into skin tissue.^{117,122} Most SNAs are designed to deliver a single-stranded oligonucleotide payload. However, Gli

consensus sequence DNA must be double stranded to allow for Gli recognition.¹²³ Thus, the design was modified to allow for release of the double-stranded CoGli agent, as shown in Figure 23. Specific DNA sequences used can be found in section 3.4.2.1. materials and methods.

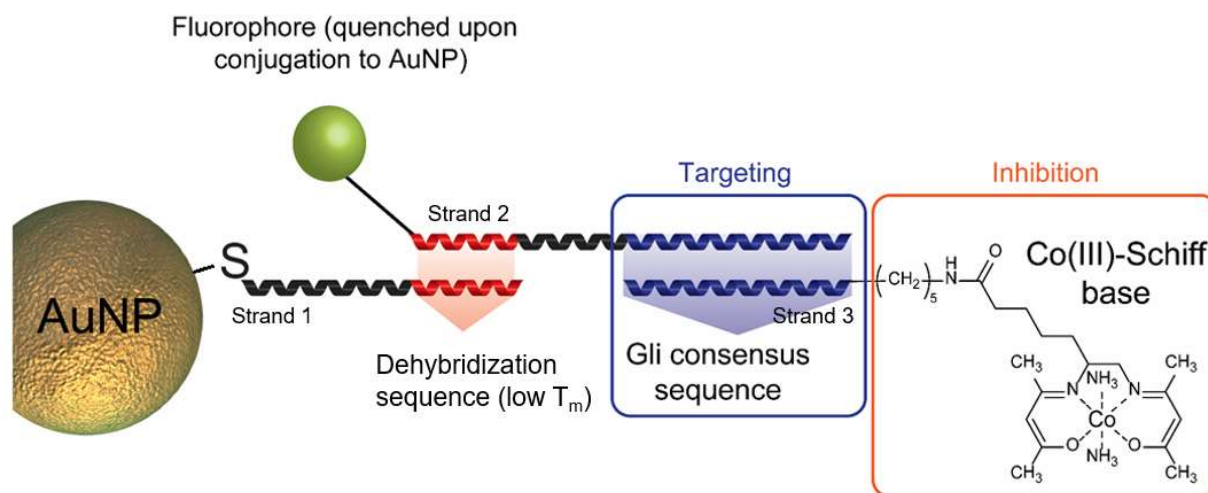


Figure 23. AuGliCo, the nanoconjugate designed for delivery of double-stranded CoGli into cells and tissues. AuGliCo contains a dehybridization sequence of DNA with a low T_m for heat-induced release of CoGli payload. A fluorophore allows for tracking of released payload in cells. The CoGli inhibitory agent contains an ssDNA overhang when released, but the targeting and inhibition moieties remain the same.

3.1.2. DNA Loading and Release from Spherical AuNPs

Following published protocols, AuNP were functionalized with thiol-modified DNA (strand 1) and purified with multiple rounds of centrifugation.^{116,124–127} Using cyanide digestion, loading of thiol-modified DNA was determined to be 134-161 strands of DNA/NP. Fluorophore-modified DNA (strand 2) and Co(acacenHA)-modified DNA (strand 3) were then annealed to the pure product simultaneously. The fluorophore TYE 665 was selected for the current work and is a Cy5 mimic (ex/em 645/665). Loading of annealed strand 2 was 115-170 strands/NP, while loading of annealed strand 3 was 152-182 strands/NP. Only slight stoichiometric discrepancies were

observed, and they can likely be attributed to measurement error across multiple modalities. It is important to note that strands 2 and 3 should not be annealed sequentially; only simultaneous annealing was shown to yield stoichiometric ratios. Moreover, it may be useful to “backfill” the Au surface with thiol-terminated 5-kDa polyethylene glycol (PEG) for stabilization of oligonucleotides.¹²⁸

To investigate temperature-induced release, a truncated nanoconstruct was prepared in which the dehybridization sequence and fluorophore remained identical, but the Gli consensus sequence was not included. The modified construct was incubated at room temperature, 37°C, and 60°C. Fluorescence was measured at 0.5, 1, 2, and 3 hours. Because fluorescence is quenched when the fluorophore is proximal to the NP surface, an increase in fluorescence is indicative of release from the NP construct. This process and the modified construct design are depicted in Figure 24. It was determined that NPs need not be removed from solution for fluorescence measurements; aliquots may simply be removed and measured directly. Upon released from the NP, fluorescence is un-quenched even if free fluorophore and AuNP are still present together in solution.

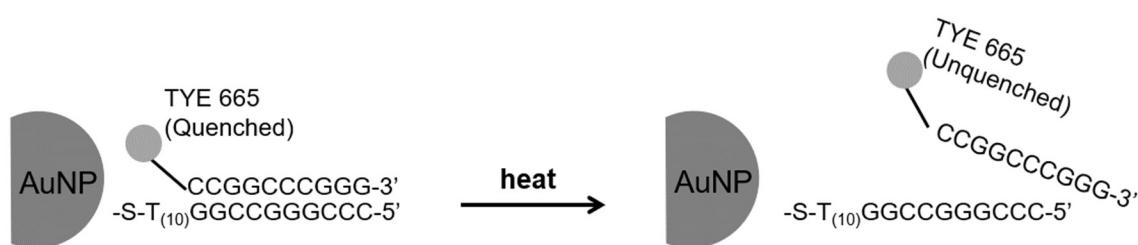


Figure 24. A modified SNA nanoconstruct was designed for assessing temperature-induced release of hybridized DNA from the AuNP. The hybridized DNA was fluorescently labeled with TYE 665 fluorophore for easy fluorometric detection of dehybridization. The fluorophore is quenched when proximal to the NP surface but is unquenched upon release. This same construct was used as a control (“Au-DNA control”) in later studies.

The results (Figure 25) demonstrate that fluorescently labeled DNA is being released very rapidly in solution at 37°C, and 60°C, but not at room temperature. The increase in fluorescence cannot be attributed to temperature alone. Given that the expected T_m of this sequence in solution is expected to be 40°C, the rapid release at 37°C is somewhat surprising. It is even more surprising given that we expect the T_m to increase when near the surface of a gold nanoparticle, given the high local salt concentration.^{129–131} However, Xu and Craig¹³² and Randeria et al.¹³³ demonstrate that DNA hybridization on the surface of 13 nm AuNP is destabilized as the fraction of hybridized DNA increases. This supports the present findings, which suggest that (a) close to 100% of available hybridization sites are occupied by annealed DNA, and (b) the AuNP constructs release up to 55% of their complementary DNA, at which point the remaining hybridized DNA are stabilized and have a higher T_m .

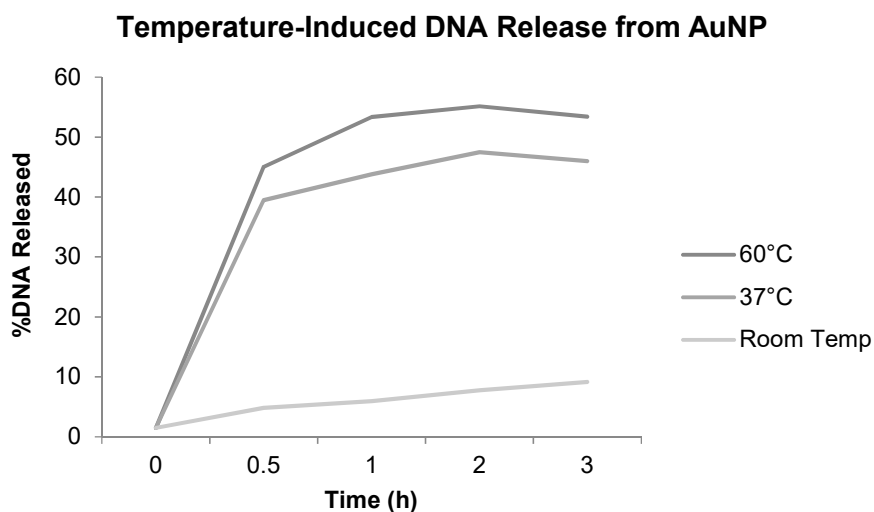


Figure 25. Temperature-induced release of fluorescently-labeled DNA from AuNP at RT, 37°C, and 60°C. For this study, a model version of AuGliCo was used, as shown in Figure 24. The T_m appears lower than anticipated for a 10-mer of 100% GC content (5'-CCGGCCCGGG-3'). The observed destabilization can be attributed to the high fraction of hybridized duplexes.

3.1.3. Cellular Uptake and Viability

Cellular uptake of AuGliCo was measured in BSZ murine basal cell carcinoma cells. Spherical nucleic acid nanoconstructs readily enter cells due to the favorable interaction with class A scavenger receptors and subsequent endocytosis.^{128,134,135} Because CoGli presents on the outside of the spherical nucleic acid nanoconstruct, it was postulated that it may interfere with this interaction and negatively affect cell uptake. Thus, cellular uptake of AuGliCo was compared against a DNA-functionalized AuNP control (“Au-DNA control” design shown in Figure 24). The results (Figure 26.a.) demonstrate no statistically significant difference in uptake after 24 h between AuGliCo and Au-DNA control. Cell viability is not negatively affected by the presence of AuGliCo or Au-DNA control at any concentration (Figure 26.b.).

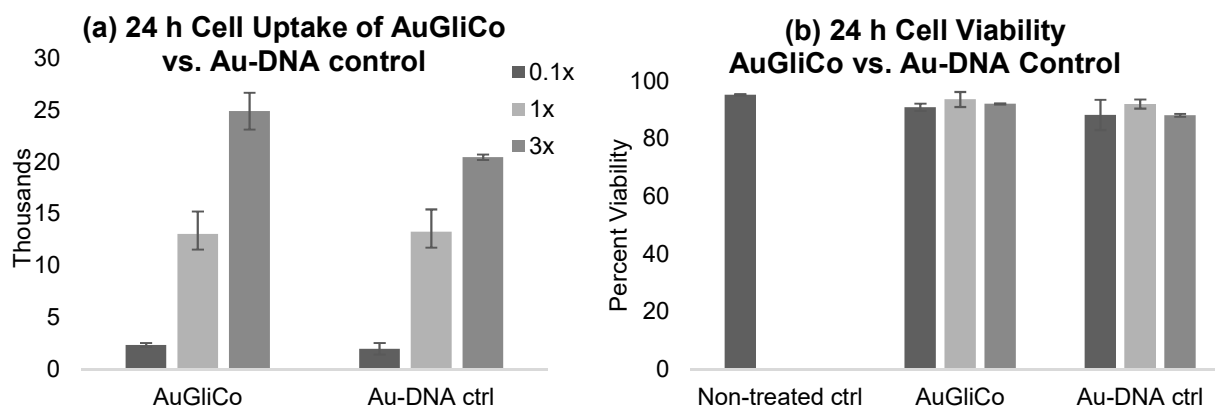


Figure 26. (a) Cellular uptake of AuGliCo and Au-DNA control in BSZ cells after 24 h. Uptake is given in thousands of NP/cell. No statistically significant difference is observed between AuGliCo and Au-DNA control uptake at any concentration. (b) Cell viability of BSZ after 24 h incubation with AuGliCo and Au-DNA control. No significant toxicity is noted at the studied concentrations. Concentrations of 0.1x, 1x, and 3x NP were used for both experiments, where 1x corresponds to 100 nM CoGli.

3.1.4. Confocal Microscopy

To visualize entry of AuGliCo and release of CoGli into cells, confocal microscopy was

performed with BSZ murine basal cell carcinoma cells. AuGliCo was once again compared against an Au-DNA control (Figure 24) for comparison. Results are shown in Figure 27 and demonstrate fluorescence and cellular delivery for both AuGliCo and Au-DNA, as well as some colocalization with the nucleus as seen in z-stacks (not shown).

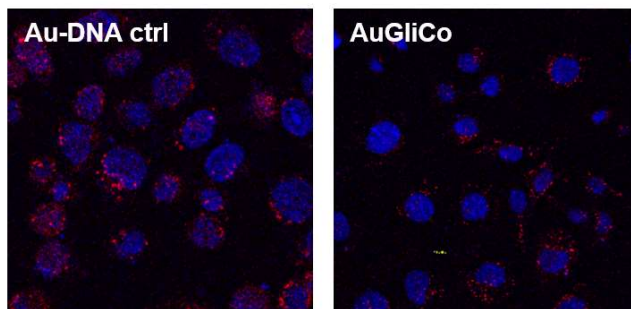


Figure 27. Confocal microscopy of Au-DNA control (left) and AuGliCo (right) demonstrate cellular entry of nanoconstructs and release of fluorescently-labeled DNA. TYE 665-labeled DNA is shown in red, while DAPI nuclear stain is shown in blue.

Despite previous results demonstrating no significant difference in cell uptake, TYE 665-labeled DNA fluorescence is 50% lower in the AuGliCo sample than the Au-DNA control sample. This discrepancy is likely because imaging was performed at $t=3$ h, while uptake measurements were gathered at $t=24$ h. Taken together, the results suggests that AuGliCo is taken into cells more slowly than typical Au-DNA spherical nucleic acids. Placing Co(acacenHA) on the outside of the construct may impact the speed of cellular delivery, but the design is ultimately effective as a delivery agent. Cell uptake experiments at various timepoints are required to determine this conclusively.

3.1.5. *Biological Activity*

To assess whether AuGliCo can deliver CoGli into cells and inhibit the Hh pathway, a dual

luciferase assay was performed with NIH/3T3 Shh light II cells. The cells were induced for Hh pathway activity and treated with AuGliCo or Au-DNA control, the modified nanoconstruct depicted in Figure 24. Au-DNA control contains neither Gli consensus sequence DNA nor the Co(acacenHA) inhibitor, so it is not expected to have any effect on Gli-responsive luciferase signaling. However, the results in Figure 28 show a similar response for both AuGliCo and Au-DNA control. Thus, no conclusive Hh pathway inhibition can be determined with this assay. An alternative method such as qPCR should be used instead. Similar to some transfection agents, DNA-functionalized AuNP enter cells via an endocytotic mechanism,¹³⁴ and this may be the cause of the similar nonspecific decrease in Gli-responsive luciferase.

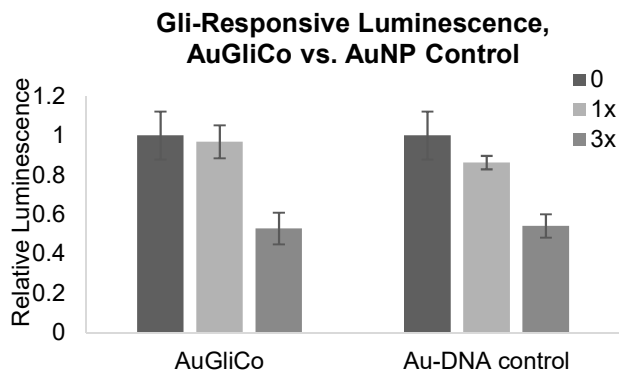


Figure 28. Gli-responsive luminescence decreases in the presence of increasing concentrations of AuGliCo and Au-DNA control. Au-DNA control is not expected to affect Gli activity, so no conclusive inhibition was demonstrated.

3.2. Graphene Oxide (GO) Nanosheets

3.2.1. Background and Designs of Nano Constructs

Graphene oxide nanosheets (GO) have previously been used by the Meade lab to demonstrate remarkable small molecule loading and delivery into cells.¹³⁶ GO are single layer,

carbon-based nanoparticles that are essentially two-dimensional; their surface area:volume ratio approaches the theoretical maximum. They are able to carry significant chemical or biological payloads and deliver them efficiently into living cells.^{137–141} Of particular interest, they have been used to deliver ssDNA into cells for biological effect.^{142–144} GO has highly favorable interactions with ssDNA due to pi stacking of the available purine and pyrimidines, but no notable interaction with dsDNA.¹⁴⁵ For this reason, it was hypothesized that GO would adsorb CoGli with a 5ss or 10ss “sticky” DNA overhang, as depicted in Figure 29. These two nano constructs are termed 5ssGli@GO and 10ssGli@GO, respectively.

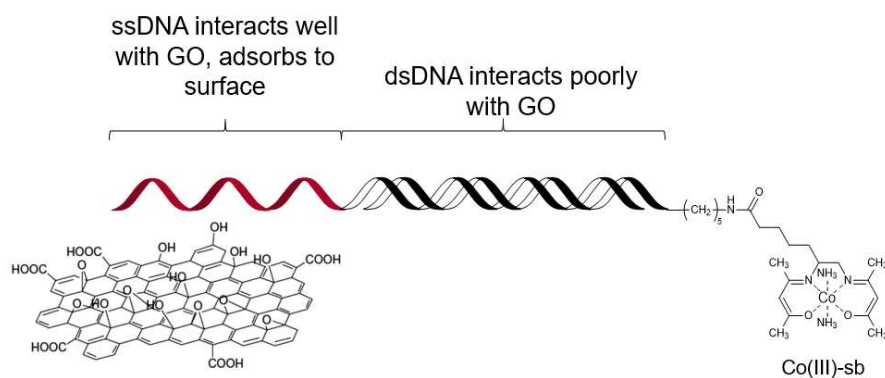


Figure 29. CoGli with ssDNA overhangs (termed 5ssGli, 10ssGli) were generated and adsorbed to GO. The ssDNA overhang (either 5 or 10 nucleotide base pairs) is expected to interact strongly with the GO surface, while the dsDNA Gli consensus sequence is expected to interact poorly with the GO surface.

A second method for delivering CoGli with GO involves functionalization with polyethyleneimine (PEI). PEI is commonly used as a transfection agent in mammalian cells, but is associated with significant toxicity.^{146,147} Adsorbing PEI onto the surface of GO or covalently coupling it to yield GO-PEI has been shown to mitigate PEI’s toxicity while improving GO’s ability to interact with and deliver dsDNA into cells.¹⁴⁸ After being endocytosed, PEI promotes

the proton sponge effect leading to endosomal rupture, allowing dsDNA to be delivered into cells. Thus, the two nanoconjugate designs in Figure 30 were studied, both utilizing CoGliFluor. The first, GO-CoGli, relies on the favorable GO/fluorophore pi-pi interaction for noncovalent association with the GO. This interaction may not be strong enough to facilitate adsorption and is expected to exhibit low loading. The second, Go-PEI-CoGli, relies on the electrostatic interaction between positively charged PEI on the GO surface and negatively charged oligonucleotides. This interaction is expected to be favorable and yield measurable loading. Neither of these designs utilizes ssDNA in the CoGli sequence for binding.

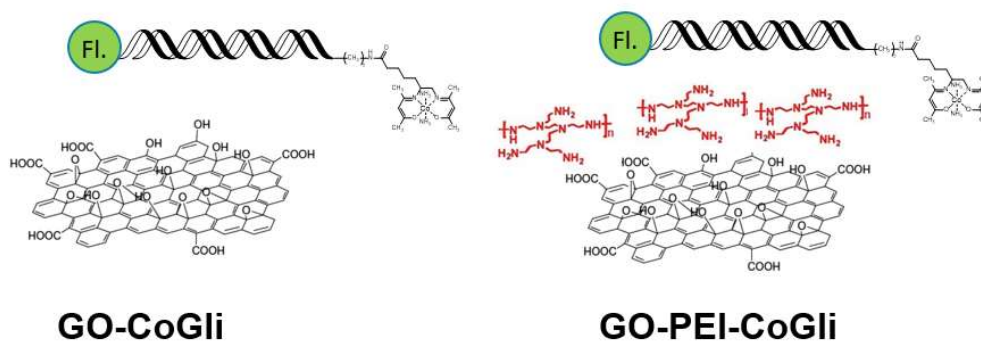


Figure 30. Design of GO-CoGli and GO-PEI-CoGli. These nanoconjugates rely on noncovalent association of CoGliFluor with the GO nanosheet. GO-CoGli interacts via pi-pi stacking between the fluorophore (AlexaFluor488) and the GO surface. GO-PEI-CoGli interacts electrostatically via positively charged PEI and negatively charged dsDNA.

3.2.2. DNA Loading and Release from GO Nanosheets

3.2.2.1. 5ssGli@GO and 10ssGli@GO Loading

Two CoGli@GO nanoconstructs were prepared. The first (5ssCoGli@GO) had a 5 nucleotide base ssDNA overhang, while the second (10ssCoGli@GO) had a 10 nucleotide base

ssDNA overhang. The sequences used were:

Glirev5ss = 5'-TTTTTAGAGACCACCCAGGTAG-3'

Glirev10ss = 5'-TTTTTTTTTTAGAGACCACCCAGGTAG-3'

Sequences with and without flanking phosphorothioate linkages were used. As these constructs were not fluorescently labeled, the most straightforward way to measure GO loading was by measuring DNA concentration in the supernatant via UV/Vis. By comparing the absorbance at 260 nm of the DNA solution before and after adding GO and spinning down, the change in solution-state DNA concentration can be determined.

Representative spectra for 5ssGli are shown in Figure 31. For this experiment, the DNA concentration was held constant, while the concentration of GO was varied from 0.1 – 1.0 mg/mL. As expected, a higher GO:DNA ratio leads to more DNA binding and a concomitant decrease in the 260 nm absorbance band. 10ssGli data showed a similar trend. Using this data, 5ssGli@GO and 10ssGli@GO loading values were calculated to yield the results shown in Figure 32.

Note that the 0.1 mg/mL GO sample has slightly higher $A_{260\text{nm}}$ than does free DNA alone, so the calculated loading values for 0.1 mg/mL samples were negative. This was a consistent trend across experiments and indicates that GO was not entirely removed from solution by centrifugation. GO absorbs strongly in this region; even a small amount remaining in the supernatant would lead to an increase in observed absorbance. Thus, all DNA loading values calculated in these studies are assumed to be artificially low.

Nonetheless, DNA loading of up to 200 mg DNA/g GO was observed. Comparing against values in the literature, this is moderate loading.^{144,149,150} However, given the unique design of this nanoconstruct containing both ssDNA and dsDNA, the values are not directly comparable.

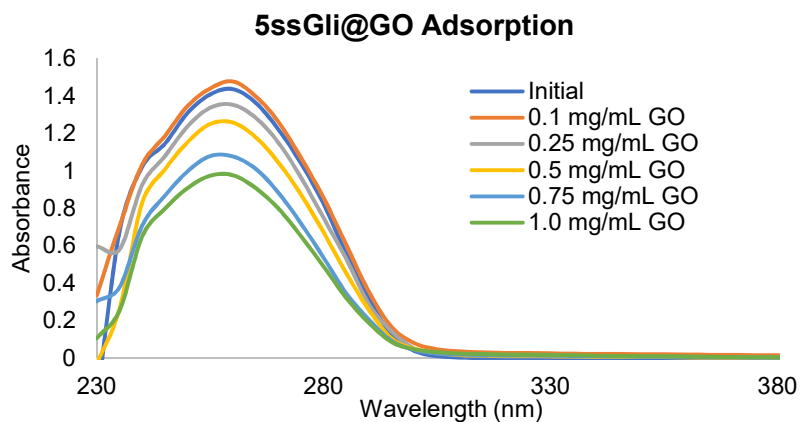


Figure 31. UV/Vis spectra of supernatants after adsorption of 50 μ M 5ssGli with various concentrations of GO. As expected, the concentration of DNA in the supernatant decreases as the GO reaction concentration increases due to more DNA being bound by GO. Loading values calculated from these results may be artificially low, as GO does not spin down perfectly and is likely increasing absorbance maxima at 260 nm.

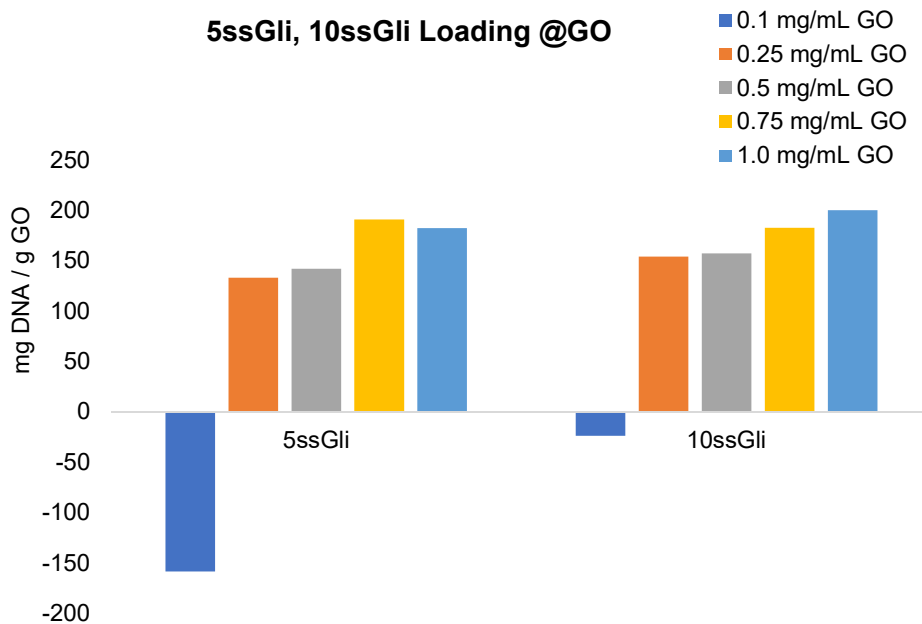


Figure 32. 5ssGli and 10ssGli loading on GO nanoparticles, calculated from UV/Vis data. Loading is given in terms of mg DNA/g GO; apparent negative values are due to the interference of a small amount GO remaining in the supernatant.

3.2.2.2. 5ssGli@GO and 10ssGli@GO Release

The ssGli@GO nanoconstructs are intended to enter cells and release the CoGli payload. For this reason, release at 37°C was measured over 6 h (Figure 33). Aliquots of ssGli@GO were incubated, removed from heat at the appropriate time point, and centrifuged to remove GO. The supernatant was then measured for dsDNA content using the Quant-iT HS dsDNA assay kit. The kit is designed for use with ≥ 50 -mer DNA, so standards of dsGli5ss and dsGli10ss were prepared and concentration was verified with UV/Vis to ensure proper calibration (see materials and methods, section 3.4.2.5). Controls were also performed to ensure that the observed increase in fluorescence was not an effect of temperature.

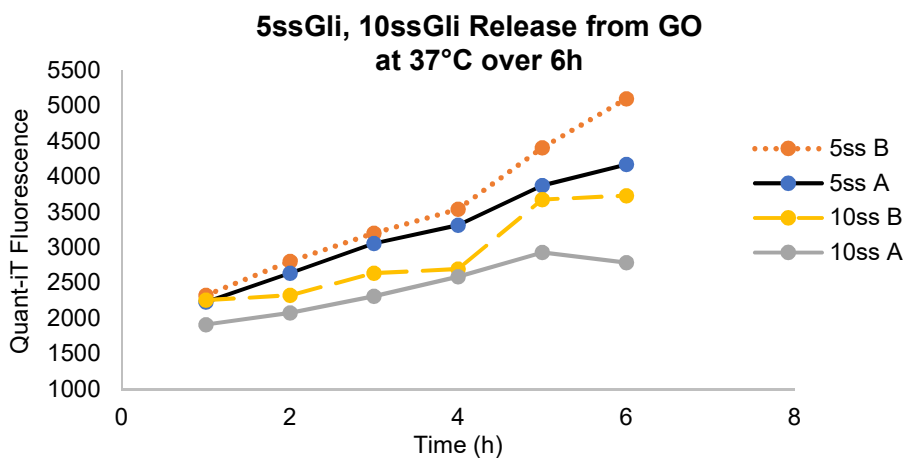


Figure 33. Release of 5ssGli and 10ssGli from GO at 37°C was measured hourly over 6 h. In this intercalative assay, an increase in fluorescence indicates an increase in dsDNA concentration in the supernatant.

An additional measurement was performed at $t = 20$ h, but fluorescence did not increase further (Figure 34), possibly indicating that release had leveled off. Taken together, these results indicate modest release of CoGli from GO in a non-biological system.

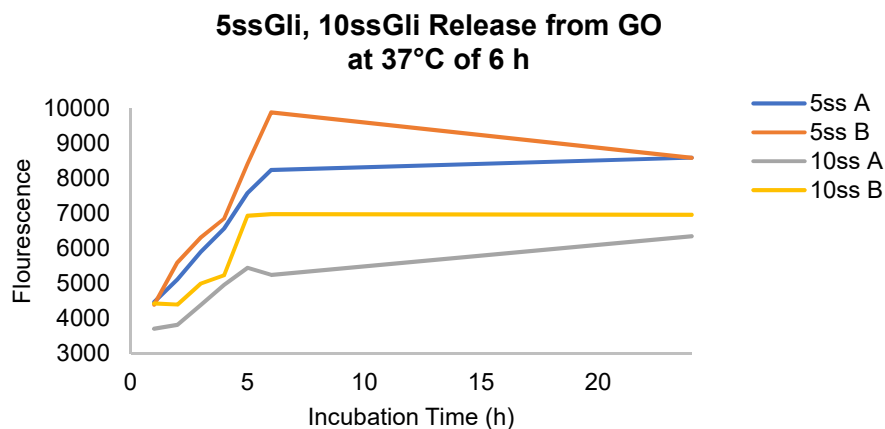


Figure 34. An additional timepoint $t = 20$ h was measured to determine whether DNA release would continue to trend upward. The 20 h time point was not significantly higher than the 6 h time point, and in some cases was lower. If desired, additional time points could be taken between $t = 6$ h and $t = 20$ h to ascertain max release time.

3.2.2.3. GO-PEI Synthesis

A number of procedures for functionalizing GO with PEI exist in the literature.^{146,148,151-153} The protocol published by Feng et al.¹⁴⁸ was attempted, but synthesis was unsuccessful. GO crashed out of solution immediately upon first addition of PEI. Instead, the method published by Song et al.¹⁵³ was modified for small scale use and successfully implemented. In brief, GO is converted to GO-COOH using NaOH and chloroacetic acid. EDC chemistry is then used to covalently couple PEI to carboxyl groups of the GO surface. Horn sonication is performed following the coupling procedure to ensure particles remain small (100-200 nm) and relatively monodisperse. Particles that are not horn sonicated after coupling are large (micron scale) and settle out of solution.

Infrared (IR) spectroscopy was performed to analyze the surface chemistry of GO, GO-COOH, and GO-PEI. Figure 35 shows GO-COOH vs. GO-PEI. The reduction of C=O stretches at

1719 cm^{-1} and growth of amide stretches at 1616 cm^{-1} and 1571 cm^{-1} is indicative of amide bond formation with carboxyl groups and agrees with literature precedent.¹⁵³

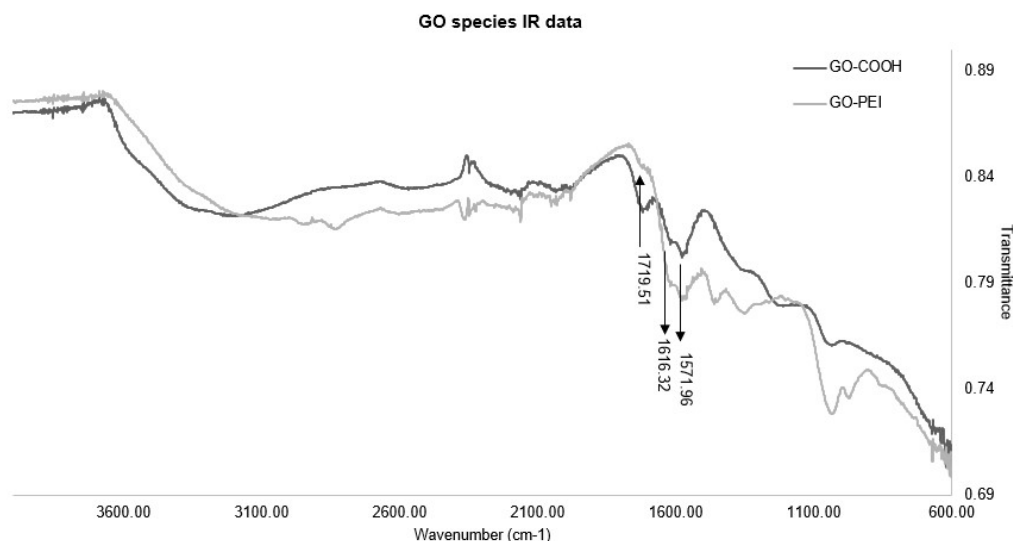


Figure 35. IR spectra of GO-COOH and GO-PEI. C=O stretching at 1719 cm^{-1} decreases, while amide stretches at 1616 cm^{-1} and 1571 cm^{-1} increase, indicative of formation of amide bonds. IR data belongs to Meghan Ward.

Atomic force microscopy (AFM) was used to assess the relative z heights of unmodified GO versus GO-PEI (Figure 36). The heights were determined to be significantly different at $p=0.0003$; GO z height= 6.4 ± 3.7 nm, while GO-PEI z height= 11.5 ± 2.9 nm. This further suggests that functionalization with PEI was successful. Unmodified GO sheets are typically expected to have a smaller z height at 2-3 nm, and indeed 2-3nm particles were more abundant than any other size. However, sample preparation can cause sheets to stack that otherwise would have remained as single sheets in solution. In addition to increasing in z height, GO-PEI also had decrease lateral length when compared to GO. Although it may seem counterintuitive, this agrees with literature precedent and is credited to sheet folding after functionalization.^{146,148,151,153}

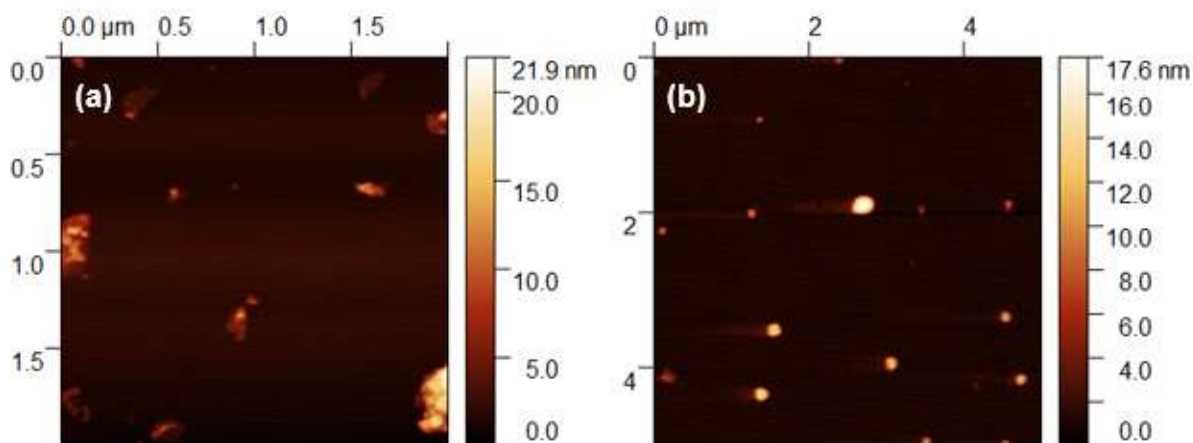


Figure 36. AFM images of (a) unmodified GO, and (b) GO-PEI. The average z heights of unmodified GO and GO-PEI were statistically different at $p= 0.0003$. An increase in z height suggests functionalization with PEI was successful. AFM data belongs to Chris Brue.

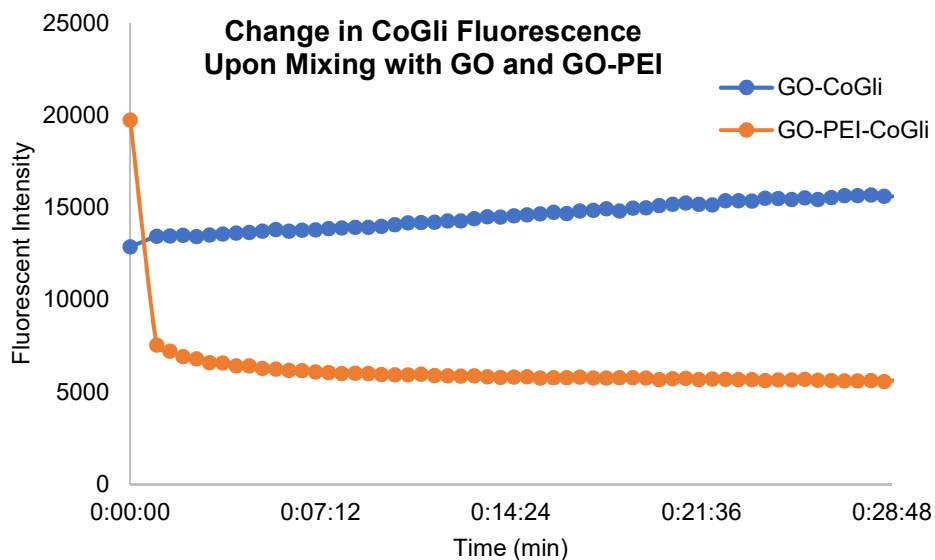


Figure 37. Upon combining CoGliFluor with GO and GO-PEI, a marked decrease in fluorescence was observed for GO-PEI-CoGli (orange) while none was observed for GO-CoGli (blue). This suggests the fluorophore-GO interaction was too weak to facilitate CoGliFluor adsorption, while robust adsorption occurred for GO-PEI-CoGli.

3.2.2.4. *GO-CoGli and GO-PEI-CoGli Loading*

Following a similar adsorption protocol to prior experiments, CoGliFluor was combined in equal volumes with GO and GO-PEI, then AlexaFluor488 fluorescence was observed in a plate reader over 30 min. Because fluorescence is quenched near the GO surface, a decrease in fluorescence is indicative of adsorption. The results in Figure 37 show that GO alone did not successfully adsorb CoGliFluor, while GO-PEI demonstrated robust adsorption. Loading can be quantified by comparing the change in observed fluorescence against an appropriate calibration curve. In this manner, CoGliFluor loading on GO-PEI is calculated as 1,440 mg CoGli/g Go.

Following this assay, a release study was attempted. Samples remained in the plate reader; temperature was set to 37°C and fluorescence was measured every 30 min. No return of fluorescence was observed. It is possible that the fluorophore had undergone too much photobleaching, but more likely that the electrostatic interactions were not overcome and no temperature-induced release occurred.

3.2.3. *Cellular Uptake and Viability*

To measure cellular uptake of GO-PEI-CoGli, cobalt concentration was measured in harvested cell samples. Although delivered cobalt concentrations are low, concentration-dependent uptake is detectable (Figure 38). The LOD of cobalt with ICP-MS is 0.002 ng/mL. If a standard cell sample harvested from a 24 well plate internalizes only 20 nM cobalt, it would yield an increase of 0.008 ng/mL in the sample, just detectable above the LOD. Cell growth media supplemented with 10% serum has roughly 1 μ M cobalt due to the presence of vitamin B12. Given the sensitivity of the measurement, it is therefore important that cell samples for digestion and analysis be suspended in DPBS instead of cell media.

Figure 38 shows increasing levels of intracellular cobalt with increasing concentrations of GO-PEI-CoGli. For comparison, results are displayed next to intracellular cobalt concentrations from a study using Lipofectamine LTX transfection agent to deliver CoGli. Uptake was measured after 24 h incubation with CoGli and delivery agent.

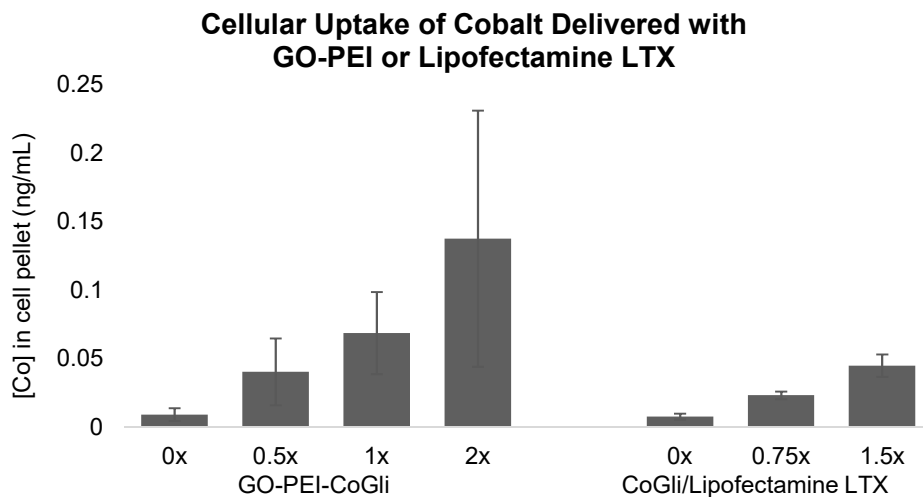


Figure 38. CoGli delivered with GO-PEI (left) or Lipofectamine LTX transfection agent (right) is detectable by ICP-MS for cobalt. In the above scheme, a 1x concentration dose is equal to 200 nM CoGli treatment. Despite the large error bars for GO-PEI-CoGli measurements, concentration-dependent uptake is observable. The large error bars are likely due to heterogeneous resuspension of the GO pellet after harvesting cells.

An MTS cell proliferation assay was performed with four concentrations of GO-PEI and GO-PEI-CoGli in ASZ murine basal cell carcinoma cells (Figure 39). In agreement with similar literature precedent, no change in viability was observed across either series. Moreover, GO-PEI and GO-PEI demonstrated similar viability profiles to one another. A slight proliferative effect can be seen as the concentration increases from 0x to 2x. As in the previous dosing scheme, a 1x dose is equivalent to treating with 200 nM CoGli. The trend, however, is not statistically significant without repetition to verify the proliferative effect.

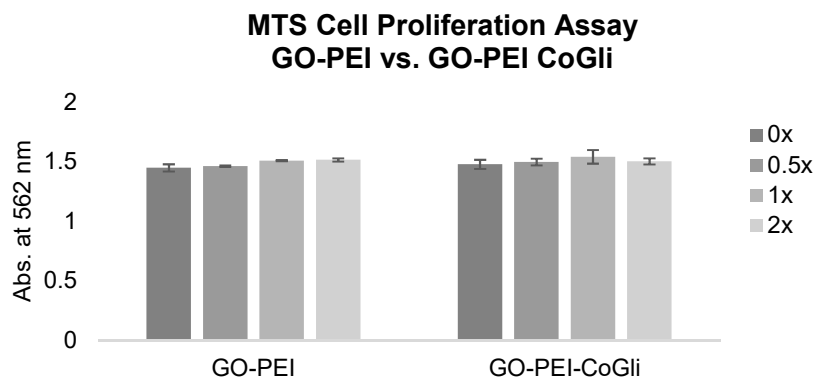


Figure 39. ASZ cells were dosed with four concentrations of GO-PEI and GO-PEI-CoGli, incubated for 24 h, and were subjected to an MTS cell proliferation assay. Results reveal no significant change in cell viability across the series 0x – 2x (where 1x= 200 nM CoGli).

3.2.4. Confocal Microscopy

Confocal microscopy imaging was performed in live cells to visualize CoGliFluor delivered by GO-PEI with 24 h incubation. Cells were co-stained with NucRed nuclear dye prior to imaging. Despite bright signal seen in the positive control sample (CoGliFluor/Lipofectamine LTX), very little CoGliFluor signal was observable in GO-PEI-CoGli treated cells. However, performing a mapping analysis of green vs. red intensities across multiple cells yielded the results seen in Figure 40.

Mapping analysis shows that green fluorescence (CoGliFluor) trends with the presence of cells and NucRed nuclear dye. Despite being difficult to observe in confocal snapshots (not shown), green fluorescence in GO-PEI-CoGli treated cells is substantially greater than that due to biological autofluorescence.

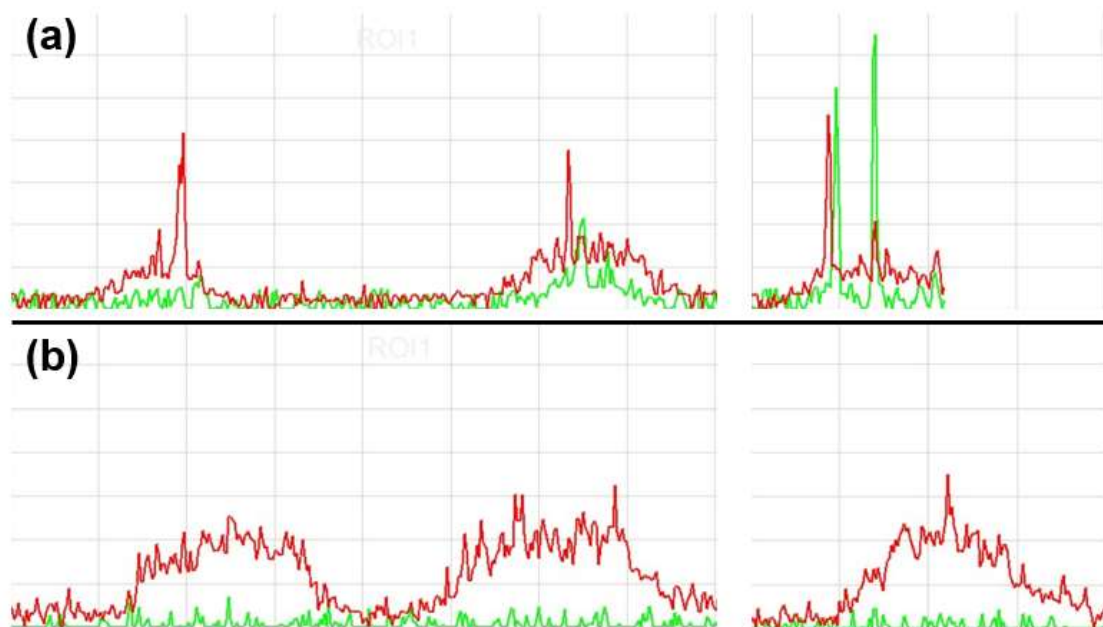


Figure 40. Mapping analysis of confocal images of three cells per condition, chosen at random. **(a)** Cells treated with GO-PEI-CoGli show green fluorescence (CoGliFluor) trending with the presence of NucRed nuclear stain. **(b)** Negative control cells treated with NucRed nuclear stain only do not show green fluorescence trending with the presence of NucRed.

3.3. Conclusions and Future Work

In summary, two successful nanoconjugates for the cellular delivery of CoGli were presented in this chapter. The gold nanoparticle construct AuGliCo incorporates a DNA dehybridization sequence that melts at 37°C to release up to 55% of its CoGli payload. Confocal microscopy and cell uptake experiments verified cell penetration and CoGli release in murine basal cell carcinoma cells. The graphene oxide-PEI nanoconjugate GO-PEI-CoGli was highly effective at binding fluorescently labeled CoGli, whereas unmodified GO was not. GO-PEI-CoGli was also able to deliver CoGli into cells, as seen by ICP-MS uptake experiments for Co and confocal fluorescence intensity mapping.

The nanoconstructs AuGliCo and GO-PEI-CoGli have not yet demonstrated inhibition of

the Hh pathway in live cells, which remains the next major hurdle in the application of these systems for investigating biological systems and disease states. AuGliCo should be tested in more Hh responsive systems beyond the NIH/3T3 Shh light II cell line. Treating ASZ cells with AuGliCo and performing qPCR is a logical next step. For GO-PEI-CoGli, however, it is possible that the presence of GO is negatively impacting mRNA quality in qPCR results. If this is determined to be the case, another assay system should be used. These nanoconjugates hold much promise for overcoming the barriers of cell delivery for the cobalt(III)-Schiff base-DNA class of protein inhibitors.

Work is ongoing to demonstrate delivery of CoGli with nanoconstructs into tissues and tissue models (see Appendix H). This is of great interest particularly with regard to AuGliCo, because SNAs have been demonstrated to deliver oligonucleotides through skin to achieve a therapeutic effect. AuGliCo can be administered at various concentrations on the surface of keratinocyte cultures by various methods including mixing with Aquaphor®, (4:1) corn oil:ethanol, and as a suspension in PBS. Tissue sections can then be removed for quantitative evaluation of CoGli release. The penetration and release of CoGli can be monitored by fluorescence microscopy as well as with laser ablation ICP-MS to determine Co and Au distribution qualitatively. Further, laser capture micro-dissection can be performed and tissue sections can be quantified for Co and Au using ICP-MS. H&E staining can ensure that treatment with AuGliCo does not adversely affect the surrounding tissue. AuGliCo is expected to penetrate tissues further than GO-PEI-CoGli or CoGli alone. Results from these experiments can determine the appropriate concentrations and formulations for in vivo application (see proposed and approved in vivo work, Appendix I).

Future work in refining the AuGliCo delivery system could employ release via laser-induced surface plasmon resonance, creating heat that dehybridizes double-stranded DNA.¹⁵⁴⁻¹⁵⁶

This would provide an effective way to localize delivery of the agent in the area it is needed, confining Hh pathway inhibition to the tissue of interest. Laser-induced agent release is ideally suited for studies in BCC systems because plasmon resonance is most effective near the surface of the skin. The wavelength needed to induce plasmon resonance could be varied by altering the size of the nanoparticle.

Should it be necessary, locked nucleic acid (LNA) sequences could be used to flank the Gli consensus sequence instead of phosphorothioate bonds. LNAs would provide increased stability of the consensus sequence against heat-induced dehybridization and against intracellular endonucleases. LNA sequences have been shown to have high thermal stability with their complementary strand and are more stable than phosphorothioate linkages.¹⁵⁷ Using this design, plasmon resonance or external heat at previously reported dehybridization temperatures would not dehybridize the crucial consensus sequence.

3.4. Materials and Methods

3.4.1. Synthesis and Characterization of Nanoparticles

3.4.1.1. AuNP

A detailed procedure for synthesizing AuNP can be found in Appendix G. In brief, all glassware was washed with aqua regia (1:3 HNO₃:HCl) and dried in oven. When glassware was dry and cool, Teflon tape was wrapped around stopper and condenser joints. 197 mg gold(III) chloride trihydrate was quantitatively transferred into round bottom flask, then total volume was brought to 500 mL mH₂O. Contents of round bottom flask were boiled and vigorously stirred.

1.148 g sodium citrate tribasic dihydrate were dissolved in 1.68 mL mH_2O and added to boiling round bottom flask all at once while vigorously stirring. The flask was closed with a stopper, boiled for 15-30 more minutes, then removed from heat. Solution changed from yellow to black to purple to red.

Gold nanoparticle size was estimated with UV/Vis and measured more accurately by dynamic light scattering (DLS), and transmission electron microscopy (TEM). Results are shown in Figure 41. TEM is considered the most direct and reliable method of assessing size.

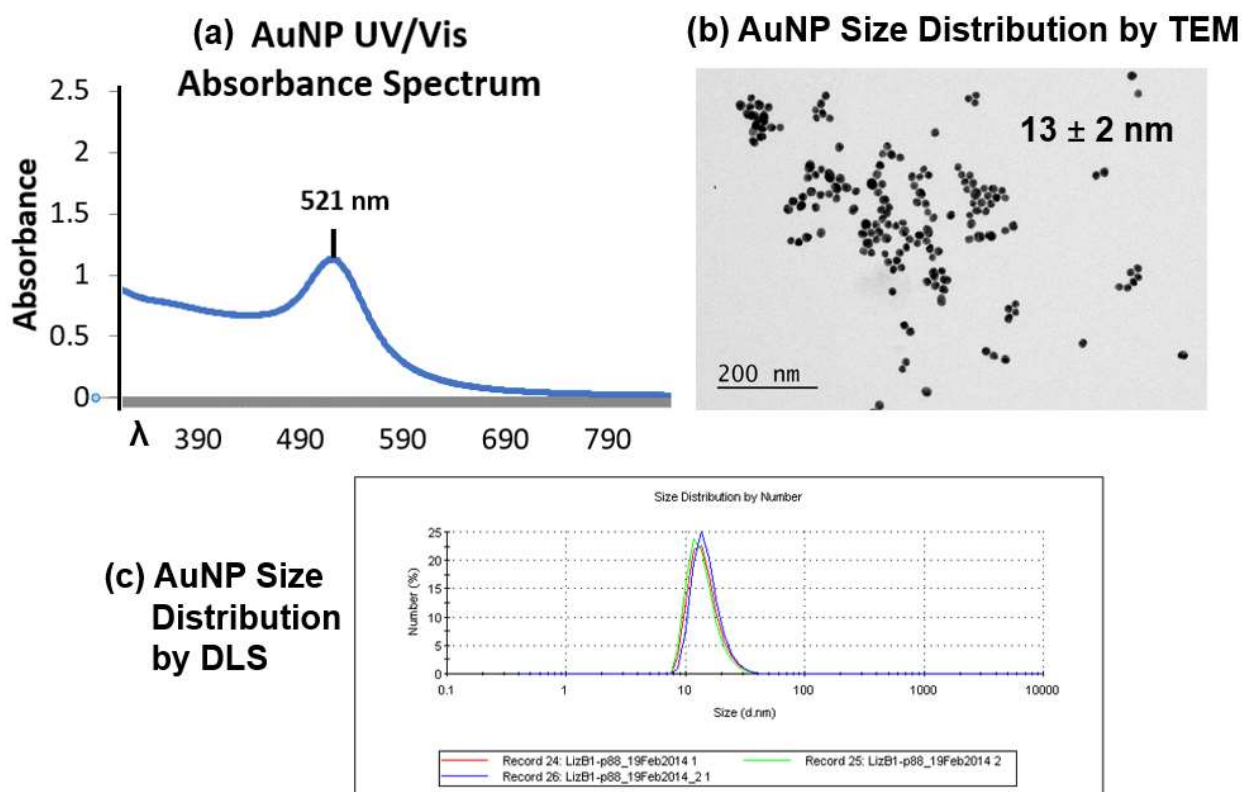


Figure 41. **(a)** UV/Vis absorbance spectrum of 13 nm gold nanoparticles. Peak for unmodified AuNP is expected at 520 nm, actual= 520.8 nm.¹⁵⁸ **(b)** Direct image of AuNP by TEM is the most accurate way to measure AuNP size; this batch had an average diameter of 13 nm \pm 2 nm. **(c)** DLS is used to measure AuNP size by light scattering in solution. Size distribution by number= 15 nm.

Using the size determined by TEM, ICP-MS was used to determine the concentration of AuNP in solution. To prepare ICP samples, 200 μL HCl, 200 μL HNO₃, and 5 μL AuNP solution were combined. After swirling to digest AuNP sample, mH₂O was added up to a total volume of 10 mL. From this solution, 1 mL was taken forward and combined with 180 μL HCl, 180 μL HNO₃, and 8640 μL mH₂O. This was the sample used for analysis by ICP-MS. The atomic mass of Au (197.97 g/mol), density of solid Au (19.32 g/mL), and radius of AuNP (determined by TEM) were then used to calculate AuNP concentration in the original stock solution.

3.4.1.2. GO

GO nanosheets were prepared by Andy Hung, a previous Meade lab graduate student, according to published protocols.^{136,159} In brief, a modified Hummer method was used in which GO was prepared from graphite flakes with sulfuric acid and KMnO₄. A slurry in water and H₂O₂ was prepared, vacuum filtered, and washed with 1:10 HCl solution. The GO was then resuspended and purified with multiple rounds of centrifugation, resuspending the GO pellet in water each time. The purified GO was then probe sonicated with a Fisher Scientific model 500 Sonic Dismembrator with a 1/2 in. tip for 1 h at 50% amplitude (~55 W). This resulted in mostly single layer GO sheets with a characteristic lateral length of 150 nm. GO was characterized by DLS (Figure 42) on a Malvern Instruments Ltd, Nano ZS Zetasizer and by AFM on Bruker Dimension FastScan® Atomic Force Microscope.

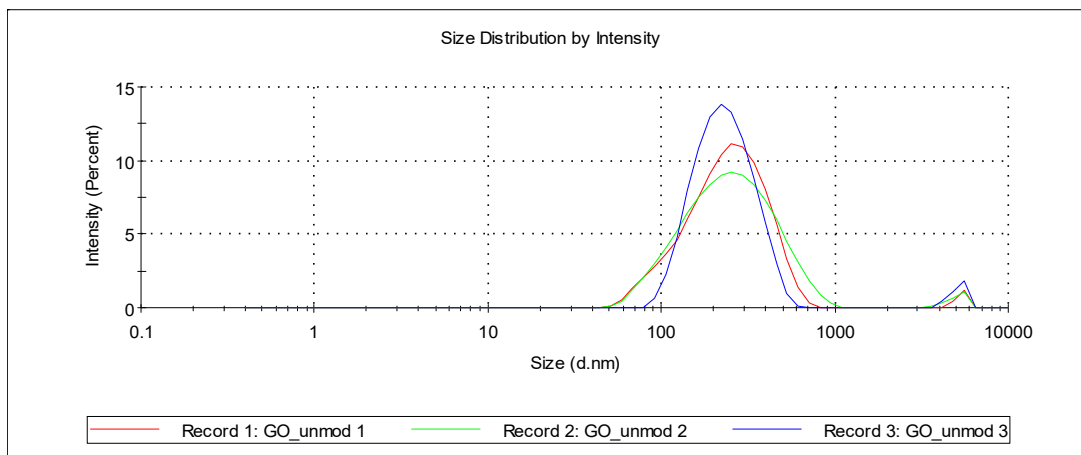


Figure 42. DLS measurements of unmodified GO show a size distribution by intensity of 89.6 – 160.1 nm for an average of 113.6 nm. This roughly corresponds to AFM results, both current and former.¹³⁶

3.4.2. Loading and Release Experiments

3.4.2.1. DNA Functionalization of AuNP

The NP was first functionalized with thiolated DNA (Figure 43). The DNA sequence (“strand 1”) purchased from IDT was 5'-CCCGGGCCGGTTTTTTTTTT/3ThioMC3-D/-3'. To deprotect the thiol bond prior to functionalization, DNA was combined with an excess of 15 mg/mL dithiothreitol (DTT) solution in phosphate buffer and mixed for 1 h. To remove DTT and byproducts, the reaction was purified using an illustra NAP-5 column (GE Life Sciences 17085301) eluting with phosphate buffer. After collecting small fractions in microcentrifuge tubes, the fractions were analyzed by UV/Vis to determine DNA content and purity. Note that some fractions contain an impurity that absorbs below 260 nm; these fractions will cause AuNP to crash out of solution and should not be used.

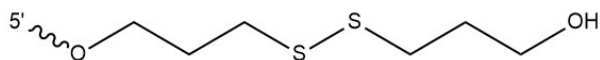


Figure 43. The 3' thiol Modifier 3ThioMC3-D purchased from IDT was attached to the 3' end of the DNA sequence of interest. Using DTT, the disulfide bond is cleaved, leaving the thiol bond available for binding to the Au surface.

A “salt aging” procedure was used to carry out functionalization of AuNP. Pure DNA fractions were combined with AuNP in a molar ratio of 300:1 DNA:AuNP, and Tween 20 solution was added for a final concentration of 0.01% Tween 20 (v/v). Subsequently the salt concentration was incrementally increased over 2.5 – 5 h for a final salt concentration of 0.6 M Na⁺. This was executed by preparing an aqueous solution containing 4.7 M NaCl, 10 mM phosphate buffer, and 10% Tween 20, and adding 5 aliquots over several hours. The high salt concentration is necessary for shielding of repulsive forces between DNA strands on the AuNP surface.^{118,124} Functionalized AuNP were purified via multiple rounds of centrifugation, resuspending the AuNP pellet each time with fresh DPBS containing 0.01% Tween 20.

To anneal subsequent strands of DNA onto the AuNP, 1.1 equivalents of DNA were added to the functionalized AuNP sample and heated with shaking at 60°C (or at least 10°C above T_m of DNA sequence) for 1 hour. Samples were cooled slowly in Styrofoam overnight and purified with centrifugation as before. The DNA sequence used for testing of fluorescently-labeled DNA release (“strand 2a”) was 5’-/5TYE665/CCGGCCCGGG-3’. Strand 2a is complementary to strand 1, non-palindromic, and is modified with 5’ TYETM 665, a proprietary fluorophore with ex/em 645/665 nm. The DNA sequences used for preparing the entire AuGliCo construct (“strand 2” and “strand 3”) were 5’-/5TYE665/CCGGCCCGGGTTTTTTTTTTA*G*A*GACCACCCA-GG*T*A*G-3’ and 5’-/5AmMC6/C*T*A*CCTGGGTGGTC*T*C*T-3’. In these sequences, * indicates a

phosphorothioate bond and 5AmMC6 indicates 5' amino modifier C6 (Figure 44). Strands 2 and 3 contain the Gli consensus sequence, and the amino modifier on strand 3 is used for peptide coupling to Co(acacenHA). When preparing the entire AuGliCo construct, it is necessary to anneal both strands 2 and 3 to the NP simultaneously. It is also useful to backfill with OEG thiol (Nanoscience CMT009) after functionalizing with strand 1 DNA, as this has been shown to increase reproducibility. After salt aging with strand 1 but before purifying, 2 μL of 10 mg/mL OEG thiol were added to 3 mL DNA-functionalized AuNP and turned end-on-end for 6 h. Purification and subsequent steps then proceeded normally.

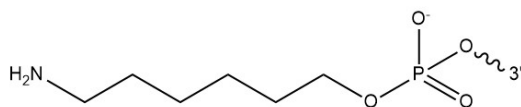


Figure 44. The 5' amino modifier C6 (5AmMC6) was used for peptide coupling Gli consensus sequence DNA to Co(acacenHA).

3.4.2.2. Characterization of DNA-Functionalized AuNP

To determine DNA loading on AuNPs, 100 μL functionalized and purified AuNP sample was treated with 5 μL 1 M potassium cyanide (KCN). The sample was incubated at 37°C for one hour or until solution was colorless and sample was completely digested. DNA loading was measured after the initial functionalization step as well as subsequent annealing steps. To measure loading of strand 1 only, a digested AuNP sample without DNA was used as a blank, and absorbance of sample was measured at 260 nm to determine DNA concentration and calculate loading. To measure loading of subsequent DNA strands, KCN digestion was performed as before, then digested sample was measured via fluorescence spectroscopy (if fluorophore present) or via

Quant-iT™ dsDNA Assay Kit, high sensitivity (ThermoFisher Q33120) to measure [dsDNA].

3.4.2.3. Release of Fluorescently-Labeled DNA from AuNP

To measure heat-induced release, samples were incubated at 37°C or 60°C. At pre-specified timepoints, 100 µL aliquots were removed, diluted, and fluorescence was measured with a Hitachi F-4500 fluorescence spectrophotometer at ex/em 645/665 nm. To quantify release, calibration curves of TYE 665-labeled DNA were prepared and measured in identical diluent to sample. For preparing calibration standards, it is important to note that the presence of Tween® 20 detergent (Sigma-Aldrich P9416) significantly affects fluorescence of 5' TYE™ 665-modified DNA (Figure 45).

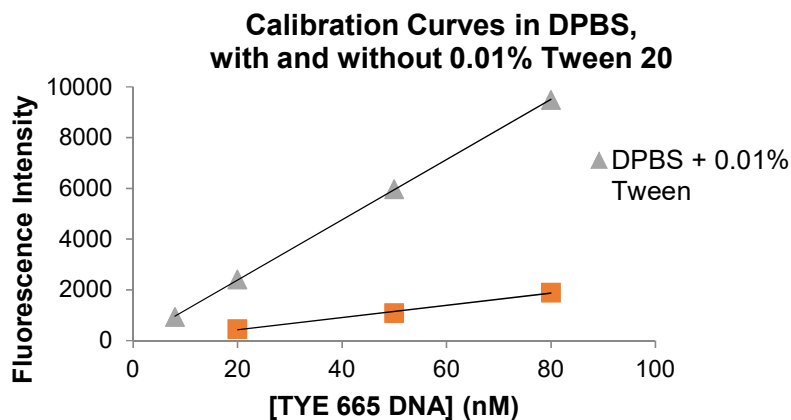


Figure 45. Fluorescence calibration curves of TYE 665-modified DNA in DPBS with and without 0.01% Tween 20 detergent. It was determined that the presence of Tween significantly increases fluorescence of TYE 665 DNA, and it is therefore important to ensure the diluent of calibration standards exactly matches that of samples being analyzed.

3.4.2.4. Loading of 5ssGli and 10ssGli @GO

The adsorption protocol was modified from that of previously published work.¹³⁶ 75 µL each of ~100 µM DNA in nuclease-free duplex buffer (IDT Cat. No. 11-05-01-03) and 1 mg/mL

GO in water were combined and left undisturbed for 15 min. Subsequently, 250 μL MEM with 10% FBS was added and reaction was rotated end-on-end for 1-2 h. The reaction is then purified with multiple rounds of centrifugation (high speed, 30 min each), washing with 400 μL 5:3 MEM:H₂O each time. The presence of MEM is needed for GO pelleting during centrifugation.

UV/Vis was used to determine the change in DNA concentration in solution before and after loading on GO nanoparticles. For these calculations, the following extinction coefficients were used:

$$\varepsilon_{\text{ds5ss}} = 325,526 \text{ L}/(\text{mol}\cdot\text{cm})$$

$$\varepsilon_{\text{ds10ss}} = 366,026 \text{ L}/(\text{mol}\cdot\text{cm})$$

The above values were calculated using an online calculator¹⁶⁰ to determine $\varepsilon = 285,026 \text{ L}/(\text{mol}\cdot\text{cm})$ for the double stranded sequence CTACCTGGGTGGTCTCT. Then contributions of 40,500 and 81,000 were added to the values for 5ss and 10ss, respectively. This accounts for increased chromicity of the single stranded overhang.

3.4.2.5. Release of 5ssGli and 10ssGli from GO

After adsorbing 5ssCoGLi@GO and 10ssCoGLi@GO as described above, 8 aliquots of each adsorbed solution were placed in a water bath at 37°C. Aliquots were removed from heat at time points $t = 0.5, 1, 2, 3, 4, 5,$ and 6 h. The final aliquot was left in the water bath at 37°C overnight. Upon removing aliquots from the water bath, they were immediately centrifuged at high speed to prevent re-adsorption onto GO. The supernatants were removed and stored at -80°C for later analysis.

To analyze dsDNA release from GO, the Quant-iT HS dsDNA assay kit was used. A fresh calibration curve was made for each sample (5ssGli and 10ssGli), and assay was performed

according to manufacturer's protocol. Calibration curves for 5ssGli and 10ssGli are shown in Figure 46 and demonstrate that the assay can be used with 17bp dsDNA.

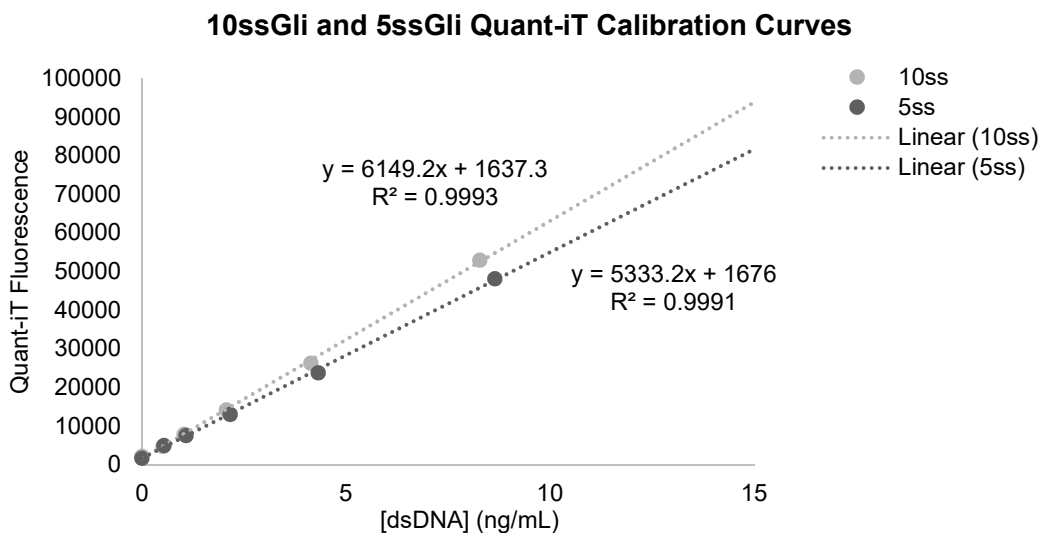


Figure 46. Calibration curves for 5ssGli and 10ssGli. Each has a 17 bp dsDNA region to which Quant-iT fluorophore can bind. Both curve fits have $R^2=0.999$, demonstrating that the Quant-iT HS assay is appropriate for use with these samples.

3.4.3. Cellular Uptake and Viability

3.4.3.1. AuNP

BSZ cells were treated with AuNP constructs AuGliCo and Au-DNA control, and cellular uptake and viability were measured after 24 h. On day 1, cells were plated at 30,000 cells/well in a 24 well plate. Cells were treated with three concentrations of NPs (0.1x, 1x, and 3x, where 1x corresponds to 100 nM CoGli) on day 2 and harvested for assays on day 3 at $t=24$ h. To harvest cells, each well was washed 2x with DPBS, trypsinized, and harvested into microcentrifuge tubes. Cells were pelleted with centrifugation and washed again in DPBS to ensure removal of non-

internalized particles associated with the cell membrane. After resuspending cell pellets in growth media, a 30 μL aliquot was used for measuring cell viability and a 130 μL aliquot was used for quantifying Au uptake via ICP-MS.

Cell viability and counting were performed on a Guava EasyCyte Mini flow cytometer. 30 μL cell suspension was combined with 170 μL Guava Viacount Reagent (EMD Millipore 4000-0040) for analysis.

Cellular uptake of AuNP was measured using ICP-MS to detect Au in cell samples. 130 μL cell suspension was combined with 100 μL trace metal grade HNO_3 and digested for ≥ 4 h. After digestion, sample was diluted to 3 mL total with mH_2O . Samples were analyzed with computer-controlled (Plasmalab software) Thermo X series II ICP-MS (Thermo Fisher Scientific, Waltham, MA, USA). Cell counting results were used to determine Au uptake/cell.

3.4.3.2. GO

Cellular uptake of GO-CoGli and CoGli/Lipofectamine LTX was performed as above (section 3.4.3.1.), using ICP-MS to detect Co. DPBS rather than media was used to resuspend the final cell pellet for analysis because cell media supplemented with 10% serum contains ~ 1 μM Co in the form of vitamin B12. 170 μL cell suspension in DPBS was digested in 110 μL HNO_3 , then the final sample was diluted to 3.5 mL with mH_2O . For GO-CoGli, ASZ cells were plated at 30,000 cells/well. For CoGli/Lipofectamine LTX, NIH/3T3 Shh light II cells were plated at 45,000 cells/well in a 24 well plate on day 1. On day 2, cells were treated with varying concentrations of CoGli/Lipofectamine LTX (0, 150, and 300 nM CoGli). On day 4, cells were harvested for assay (48 h total incubation with CoGli).

Relative cell viability was assessed with a CellTiter 96® AQueous One Solution Cell

Proliferation MTS Assay (Promega G3582). Assay was performed according to manufacturer's protocol.

3.4.4. Confocal Microscopy

3.4.4.1. AuGliCo

Confocal microscopy of AuGliCo in BSZ was performed on a Zeiss LSM510 Inverted Confocal microscope. BSZ cells were plated in glass-bottomed Fluorodishes at 30,000 cells/dish. On day 3, cells were treated with AuGliCo and Au-DNA control 3 h prior to imaging and treated with DAPI stain (Invitrogen SlowFade® Gold Antifade Reagent With DAPI) 10 min prior to imaging. In order to match conditions for biological activity assays, concentrations of NP used were equivalent to the amount needed to deliver 200 nM CoGli.

3.4.4.2. GO

Confocal microscopy of GO-PEI-CoGli in ASZ was performed on a Leica SP5 confocal microscope. ASZ cells were plated in glass-bottomed Fluorodishes at 50,000 cells/dish. On day 2, cells were treated with GO-PEI-CoGli and CoGli/Lipofectamine LTX for a 24 h imaging time point. On day 3, cells were treated with NucRed Live 647 Probe at $t = 15$ min prior to imaging. Concentrations of GO-PEI-CoGli used were equivalent to the amount needed to deliver 20 nM CoGli.

3.4.5. Biological Activity

3.4.5.1. Luciferase Assays with AuGliCo

NIH/3T3 Shh light II cells were treated with AuGliCo and assayed for Gli-responsive luciferase activity. Culture method for these cells can be found in section 2.7.3.1. and further luciferase assay details can be found in section 2.7.3.2. Cells were plated on day 1 at 45,000 cells/well in a 24 well plate. On day 3, serum starvation was initiated (swap to 0.1% CBS DMEM) and induction with 15 nM SAG was performed. On day 4, cells were treated with AuGliCo and Au-DNA control (see Figure 24). On day 6, the luciferase assay was performed. Assay was performed according to protocol described in section 2.7.3.2., with the exception that lysates were centrifuged for 30 min to pellet AuNP and remove them from the supernatant to avoid interference with luminescence.

REFERENCES

- (1) Haas, K. L.; Franz, K. J. Application of Metal Coordination Chemistry To Explore and Manipulate Cell Biology. *Chem Rev* **2009**, *109* (10), 4921–4960.
- (2) Meggers, E. Targeting Proteins with Metal Complexes. *Chem Commun Camb. U K* **2009**, No. 9, 1001–1010.
- (3) Rosenberg, B.; VanCamp, L.; Trosko, J. E.; Mansour, V. H. Platinum Compounds: A New Class of Potent Antitumor Agents. *Nature* **1969**, *222* (5191), 385–386.
- (4) Donaldson, J. D.; Beyersmann, D. Cobalt and Cobalt Compounds. In *Ullmann's Encyclopedia of Industrial Chemistry*; Wiley-VCH Verlag GmbH & Co. KGaA, 2000.
- (5) Chang, E. L.; Simmers, C.; Knight, D. A. Cobalt Complexes as Antiviral and Antibacterial Agents. *Pharm. Basel* **2010**, *3* (6), 1711–1728.
- (6) Hall, M. D.; Failes, T. W.; Yamamoto, N.; Hambley, T. W. Bioreductive Activation and Drug Chaperoning in Cobalt Pharmaceuticals. *Dalton Trans* **2007**, No. 36, 3983–3990.
- (7) MC Heffern; N Yamamoto; RJ Holbrook; AL Eckermann; Meade TJ. Cobalt Derivatives as Promising Therapeutic Agents. *Curr. Opin. Chem. Biol.* **2013**, *17*, 189–196.
- (8) Munteanu, C. R.; Suntharalingam, K. Advances in Cobalt Complexes as Anticancer Agents. *Dalton Trans* **2015**, *44* (31), 13796–13808.
- (9) Graf, N.; Lippard, S. J. Redox Activation of Metal-Based Prodrugs as a Strategy for Drug Delivery. *Adv. Drug Deliv. Rev.* **2012**, *64* (11), 993–1004.
- (10) Jungwirth, U.; Kowol, C. R.; Keppler, B. K.; Hartinger, C. G.; Berger, W.; Heffeter, P. Anticancer Activity of Metal Complexes: Involvement of Redox Processes. *Antioxid. Redox Signal.* **2011**, *15* (4), 1085–1127.
- (11) Schiff, H. Mittheilungen Aus Dem Universitätslaboratorium in Pisa: Eine Neue Reihe Organischer Basen. *Justus Liebigs Ann. Chem.* **1864**, *131* (1), 118–119.
- (12) da Silva, C. M.; da Silva, D. L.; Modolo, L. V.; Alves, R. B.; de Resende, M. A.; Martins, C. V. B.; de Fátima, Â. Schiff Bases: A Short Review of Their Antimicrobial Activities. *J. Adv. Res.* **2011**, *2* (1), 1–8.
- (13) Isloor, A. M.; Kalluraya, B.; Shetty, P. Regioselective Reaction: Synthesis, Characterization and Pharmacological Studies of Some New Mannich Bases Derived from 1,2,4-Triazoles. *Eur J Med Chem* **2009**, *44* (9), 3784–3787.
- (14) Przybylski, P.; Huczynski, A.; Pyta, K.; Brzezinski, B.; Bartl, F. Biological Properties of Schiff Bases and Azo Derivatives of Phenols. *Curr Org Chem* **2009**, *13* (2), 124–148.

- (15) Abu-Dief, A. M.; Mohamed, I. M. A. A Review on Versatile Applications of Transition Metal Complexes Incorporating Schiff Bases. *Beni-Suef Univ. J. Basic Appl. Sci.* **2015**, *4* (2), 119–133.
- (16) Dwyer, F. P.; Gyarfas, E. C.; Rogers, W. P.; Koch, J. H. Biological Activity of Complex Ions. *Nat. Lond. U K* **1952**, *170*, 190–191.
- (17) Antibiotic Resistance Fact Sheet. World Health Organization (WHO) November 2017.
- (18) Al Zoubi, W. Biological Activities of Schiff Bases and Their Complexes: A Review of Recent Works. *Int. J. Org. Chem.* **2013**, *3*, 73–95.
- (19) Tumer, M.; Koksall, H.; Sener, M. K.; Serin, S. Antimicrobial Activity Studies of the Binuclear Metal Complexes Derived from Tridentate Schiff Base Ligands. *Transit. Met Chem Dordr. Neth* **1999**, *24* (4), 414–420.
- (20) Raman, N.; Raja, S. J.; Sakthivel, A. Transition Metal Complexes with Schiff-Base Ligands: 4-Aminoantipyrine Based Derivatives—a Review. *J Coord Chem* **2009**, *62* (5), 691–709.
- (21) Bagihalli, G. B.; Avaji, P. G.; Patil, S. A.; Badami, P. S. Synthesis, Spectral Characterization, in Vitro Antibacterial, Antifungal and Cytotoxic Activities of Co(II), Ni(II) and Cu(II) Complexes with 1,2,4-Triazole Schiff Bases. *Eur J Med Chem* **2008**, *43* (12), 2639–2649.
- (22) Tweedy, B. G. Possible Mechanism for Reduction of Elemental Sulfur by *Monilinia fructicola*. *Phytopathology* **1964**, *55*, 910–914.
- (23) El-Ayaan, U.; Abdel-Aziz, A. A. M. Synthesis, Antimicrobial Activity and Molecular Modeling of Cobalt and Nickel Complexes Containing the Bulky Ligand: Bis[N-(2,6-Diisopropylphenyl)Imino]Acenaphthene. *Eur J Med Chem* **2005**, *40* (12), 1214–1221.
- (24) *Performance Standards for Antimicrobial Susceptibility Testing; Sixteenth Informational Supplement*; Clinical and Laboratory Standards Institute: Wayne, PA, 2006; Vol. CLSI document M100-S16CLSI.
- (25) Balouiri, M.; Sadiki, M.; Ibsouda, S. K. Methods for in Vitro Evaluating Antimicrobial Activity: A Review. *J. Pharm. Anal.* **2016**, *6* (2), 71–79.
- (26) Reller, L. B.; Weinstein, M.; Jorgensen, J. H.; Ferraro, M. J. Antimicrobial Susceptibility Testing: A Review of General Principles and Contemporary Practices. *Clin. Infect. Dis.* **2009**, *49* (11), 1749–1755.
- (27) Ramani, R.; Ramani, A.; Wong, S. J. Rapid Flow Cytometric Susceptibility Testing of *Candida Albicans*. *J Clin Microbiol* **1997**, *35* (9), 2320–2324.
- (28) Paparella, A.; Taccogna, L.; Aguzzi, I.; Chaves-Lopez, C.; Serio, A.; Marsilio, F.; Suzzi, G. Flow Cytometric Assessment of the Antimicrobial Activity of Essential Oils against *Listeria Monocytogenes*. *Food Control* **2008**, *19* (12), 1174–1182.

- (29) Aligiannis, N.; Kalpotzakis, E.; Mitaku, S.; Chinou, I. B. Composition and Antimicrobial Activity of the Essential Oils of Two Origanum Species. *J Agric Food Chem* **2001**, *40*, 4168–4170.
- (30) Bandyopadhyay, D.; Layek, M.; Fleck, M.; Saha, R.; Rizzoli, C. Synthesis, Crystal Structure and Antibacterial Activity of Azido Complexes of Cobalt(III) Containing Heteroaromatic Schiff Bases. *Inorg Chim Acta* **2017**, *461*, 174–182.
- (31) Zhu, Y.; Li, W.-H. Syntheses, Crystal Structures and Antibacterial Activities of Azido-Bridged Cobalt(III) Complexes with Schiff Bases. *Transit. Met Chem Dordr. Neth* **2010**, *35* (6), 745–749.
- (32) Imran, M.; Iqbal, J.; Iqbal, S.; Ijaz, N. In Vitro Antibacterial Studies of Ciprofloxacin-Imines and Their Complexes with Cu(II), Ni(II), Co(II), and Zn(II). *Turk J Biol* **2007**, *31* (2), 67–72.
- (33) Nejo, A. A.; Kolawole, G. A.; Nejo, A. O. Synthesis, Characterization, Antibacterial, and Thermal Studies of Unsymmetrical Schiff-Base Complexes of Cobalt(II). *J Coord Chem* **2010**, *63* (24), 4398–4410.
- (34) Hothi, H. S.; Makkar, A.; Sharma, J. R.; Manrao, M. R. Synthesis and Antifungal Potential of Co(II) Complexes of 1-(2'-Hydroxyphenyl)Ethylideneanilines. *Eur J Med Chem* **2006**, *41* (2), 253–255.
- (35) Patel, N. H.; Parekh, H. M.; Patel, M. N. Synthesis, Characterization and Biological Evaluation of Manganese(II), Cobalt(II), Nickel(II), Copper(II), and Cadmium(II) Complexes with Monobasic (NO) and Neutral (NN) Schiff Bases. *Transit. Met Chem Dordr. Neth* **2005**, *30* (1), 13–17.
- (36) Anitha, C.; Sheela, C. D.; Tharmaraj, P.; Sumathi, S. Spectroscopic Studies and Biological Evaluation of Some Transition Metal Complexes of Azo Schiff-Base Ligand Derived from (1-Phenyl-2,3-Dimethyl-4-Aminopyrazol-5-One) and 5-((4-Chlorophenyl)Diazenyl)-2-Hydroxybenzaldehyde. *Spectrochim Acta Part A* **2012**, *96*, 493–500.
- (37) Raman, N.; Kulandaisamy, A.; Jeyasubramanian, K. Synthesis, Spectral, Redox, and Antimicrobial Activity of Schiff Base Transition Metal(II) Complexes Derived from 4-Aminoantipyrine and Benzil. *Synth React Inorg Met-Org Chem* **2002**, *32* (9), 1583–1610.
- (38) Raman, N.; Kulandaisamy, A.; Thangaraja, C.; Jeyasubramanian, K. Redox and Antimicrobial Studies of Transition Metal(II) Tetradentate Schiff Base Complexes. *Transit. Met Chem Dordr. Neth* **2003**, *28* (1), 29–36.
- (39) A Bottcher; T Takeuchi; KI Hardcastle; TJ Meade; HB Gray; D Cwikel; M Kapon; Z Dori. Spectroscopy and Electrochemistry of Cobalt(III) Schiff Base Complexes. *Inorg Chem* **1997**, *36* (12), 2498–2504.

- (40) Asbell, P. A.; Epstein, S. P.; Wallace, J. A.; Epstein, D.; Stewart, C. C.; Burger, R. M. Efficacy of Cobalt Chelates in the Rabbit Eye Model for Epithelial Herpetic Keratitis. *Cornea* **1998**, *17* (5), 550–557.
- (41) Schwartz, J. A.; Lium, E. K.; Silverstein, S. J. Herpes Simplex Virus Type 1 Entry Is Inhibited by the Cobalt Chelate Complex CTC-96. *J Virol* **2001**, *75* (9), 4117–4128.
- (42) Louie, A. Y.; Meade, T. J. A Cobalt Complex That Selectively Disrupts the Structure and Function of Zinc Fingers. *Proc Natl Acad Sci U S A* **1998**, *95* (12), 6663–6668.
- (43) Blum, O.; Haiek, A.; Cwikel, D.; Dori, Z.; Meade, T. J.; Gray, H. B. Isolation of a Myoglobin Molten Globule by Selective Cobalt(III)-Induced Unfolding. *Proc Natl Acad Sci U S A* **1998**, *95* (12), 6659–6662.
- (44) Takeuchi, T.; Boettcher, A.; Quezada, C. M.; Simon, M. I.; Meade, T. J.; Gray, H. B. Selective Inhibition of Human α -Thrombin by Cobalt(III) Schiff Base Complexes. *J Am Chem Soc* **1998**, *120* (33), 8555–8556.
- (45) LM Manus; RJ Holbrook; TA Atesin; MC Heffern; AS Harney; AL Eckermann; TJ Meade. Axial Ligand Exchange of N-Heterocyclic Cobalt(III) Schiff Base Complexes: Molecular Structure and NMR Solution Dynamics. *Inorg Chem* **2013**, *52*, 1069–1076.
- (46) Heffern, M. C.; Kurutz, J. W.; Meade, T. J. Spectroscopic Elucidation of the Inhibitory Mechanism of Cys2His2 Zinc Finger Transcription Factors by Cobalt(III) Schiff Base Complexes. *Chem - Eur J* **2013**, *19* (50), 17043–17053.
- (47) Heffern, M. C.; Reichova, V.; Coomes, J. L.; Harney, A. S.; Bajema, E. A.; Meade, T. J. Tuning Cobalt(III) Schiff Base Complexes as Activated Protein Inhibitors. *Inorg. Chem.* **2015**, *54* (18), 9066–9074.
- (48) Takeuchi, T.; Bottcher, A.; Quezada, C. M.; Meade, T. J.; Gray, H. B. Inhibition of Thermolysin and Human α -Thrombin by Cobalt(III) Schiff Base Complexes. *Bioorg Med Chem* **1999**, *7* (5), 815–819.
- (49) Gueant, J.-L.; Caillerez-Fofou, M.; Battaglia-Hsu, S.; Alberto, J.-M.; Freund, J.-N.; Dulluc, I.; Adjalla, C.; Maury, F.; Merle, C.; Nicolas, J.-P.; et al. Molecular and Cellular Effects of Vitamin B12 in Brain, Myocardium and Liver through Its Role as Co-Factor of Methionine Synthase. *Biochimie* **2013**, *95* (5), 1033–1040.
- (50) Ndagi, U.; Mhlongo, N.; Soliman, M. E. Metal Complexes in Cancer Therapy – an Update from Drug Design Perspective. *Drug Des. Devel. Ther.* **2017**, *11*, 599–616.
- (51) Green, B. P.; Renfrew, A. K.; Glenister, A.; Turner, P.; Hambley, T. W. The Influence of the Ancillary Ligand on the Potential of Cobalt(III) Complexes to Act as Chaperones for Hydroxamic Acid-Based Drugs. *Dalton Trans.* **2017**, *46* (45), 15897–15907.

- (52) Renfrew, A. K.; Bryce, N. S.; Hambley, T. W. Delivery and Release of Curcumin by a Hypoxia-Activated Cobalt Chaperone: A XANES and FLIM Study. *Chem. Sci.* **2013**, *4* (9), 3731–3739.
- (53) Ware, D. C.; Denny, W. A.; Clark, G. R. [N,N-Bis(2-Chloroethyl)-1,2-Ethanediamine-N,N']Bis(3-Methyl-2,4-Pentanedionato-O,O')Cobalt(III) Perchlorate: A Potential Hypoxia Selective Anticancer Agent. *Acta Crystallogr. C* **1997**, *53* (8), 1058–1059.
- (54) Kim, B. J.; Hambley, T. W.; Bryce, N. S. Visualising the Hypoxia Selectivity of Cobalt(III) Prodrugs. *Chem. Sci.* **2011**, *2* (11), 2135–2142.
- (55) Shahabadi, N.; Kashanian, S.; Darabi, F. DNA Binding and DNA Cleavage Studies of a Water Soluble Cobalt(II) Complex Containing Dinitrogen Schiff Base Ligand: The Effect of Metal on the Mode of Binding. *Eur J Med Chem* **2010**, *45* (9), 4239–4245.
- (56) Barton, J. K.; Danishefsky, A.; Goldberg, J. Tris(Phenanthroline)Ruthenium(II): Stereoselectivity in Binding to DNA. *J Am Chem Soc* **1984**, *106* (7), 2172–2176.
- (57) Raja, D. S.; Bhuvanesh, N. S. P.; Natarajan, K. A Novel Water Soluble Ligand Bridged Cobalt(II) Coordination Polymer of 2-Oxo-1,2-Dihydroquinoline-3-Carbaldehyde (Isonicotinic) Hydrazone: Evaluation of the DNA Binding, Protein Interaction, Radical Scavenging and Anticancer Activity. *Dalton Trans* **2012**, *41* (15), 4365–4377.
- (58) Kirsch-De Mesmaeker, A.; Orellana, G.; Barton, J. K.; Turro, N. J. Ligand-Dependent Interaction of Ruthenium(II) Polypyridyl Complexes with DNA Probed by Emission Spectroscopy. *Photochem Photobiol* **1990**, *52* (3), 461–472.
- (59) Pollard, T. D. A Guide to Simple and Informative Binding Assays. *Mol. Biol. Cell* **2010**, *21* (23), 4061–4067.
- (60) Thordarson, P. Determining Association Constants from Titration Experiments in Supramolecular Chemistry. *Chem Soc Rev* **2011**, *40* (3), 1305–1323.
- (61) Shokohi-Pour, Z.; Chiniforoshan, H.; Sabzalian, M. R.; Esmaeili, S.-A.; Momtaziborojeni, A. A. Cobalt (II) Complex with Novel Unsymmetrical Tetradentate Schiff Base (ON) Ligand: In Vitro Cytotoxicity Studies of Complex, Interaction with DNA/Protein, Molecular Docking Studies, and Antibacterial Activity. *J Biomol Struct Dyn* **2017**, Ahead of Print.
- (62) Ghosh, K.; Mohan, V.; Kumar, P.; Singh, U. P. DNA Binding, Nuclease and Superoxide Scavenging Activity Studies on Mononuclear Cobalt Complexes Derived from Tridentate Ligands. *Polyhedron* **2013**, *49* (1), 167–176.
- (63) Chan, M.-H. E.; Crouse, K. A.; Tahir, M. I. M.; Rosli, R.; Umar-Tsafe, N.; Cowley, A. R. Synthesis and Characterization of Cobalt(II), Nickel(II), Copper(II), Zinc(II) and Cadmium(II) Complexes of Benzyl N-[1-(Thiophen-2-Yl)Ethylidene] Hydrazine Carbodithioate and Benzyl N-[1-(Thiophen-3-Yl)Ethylidene] Hydrazine Carbodithioate and the X-Ray Crystal Structure of

- Bis{benzyl N-[1-(Thiophen-2-Yl)Ethylidene] Hydrazine Carbodithioate}nickel(II). *Polyhedron* **2008**, *27* (4), 1141–1149.
- (64) Deo, K. M.; Pages, B. J.; Ang, D. L.; Gordon, C. P.; Aldrich-Wright, J. R. Transition Metal Intercalators as Anticancer Agents-Recent Advances. *Int J Mol Sci* **2016**, *17* (11), 1818/1-1818/17.
- (65) Liu, H.; Shi, X.; Xu, M.; Li, Z.; Huang, L.; Bai, D.; Zeng, Z. Z. Transition Metal Complexes of 2,6-Di((Phenazonyl-4-Imino)Methyl)-4-Methylphenol: Structure and Biological Evaluation. *Eur J Med Chem* **2011**, *46* (5), 1638–1647.
- (66) Nanjunda, R.; Wilson, W. D. Binding to the DNA Minor Groove by Heterocyclic Dications: From AT Specific Monomers to GC Recognition with Dimers. *Curr. Protoc. Nucleic Acid Chem. Ed. Serge Beaucage Al* **2012**, CHAPTER, Unit8.8-Unit8.8.
- (67) Xu, Z.-H.; Chen, F.-J.; Xi, P.-X.; Liu, X.-H.; Zeng, Z.-Z. Synthesis, Characterization, and DNA-Binding Properties of the Cobalt(II) and Nickel(II) Complexes with Salicylaldehyde 2-Phenylquinoline-4-Carboylhydrazone. *J Photochem Photobiol A* **2008**, *196* (1), 77–83.
- (68) Matosziuk, L. M.; Holbrook, R. J.; Manus, L. M.; Heffern, M. C.; Ratner, M. A.; Meade, T. J. Rational Design of [Co(Acacen)L₂]⁺ Inhibitors of Protein Function. *Dalton Trans* **2013**, *42* (11), 4002–4012.
- (69) Harney, A. S.; Lee, J.; Manus, L. M.; Wang, P.; Ballweg, D. M.; La Bonne, C.; Meade, T. J. Targeted Inhibition of Snail Family Zinc Finger Transcription Factors by Oligonucleotide-Co(III) Schiff Base Conjugate. *Proc Natl Acad Sci U S A* **2009**, *106* (33), 13667–13672, S13667/1-S13667/3.
- (70) AS Harney; TJ Meade; C LaBonne. Targeted Inactivation of Snail Family EMR Regulatory Factors by a Co(III)-Ebox Conjugate. *PLoS ONE* **2012**, *7* (2), e32318.
- (71) Hurtado, R. R.; Harney, A. S.; Heffern, M. C.; Holbrook, R. J.; Holmgren, R. A.; Meade, T. J. Specific Inhibition of the Transcription Factor Ci by a Cobalt(III) Schiff Base-DNA Conjugate. *Mol Pharm.* **2012**, *9* (2), 325–333.
- (72) Anzellotti, A. I.; Farrell, N. P. Zinc Metalloproteins as Medicinal Targets. *Chem. Soc. Rev.* **2008**, *37* (8), 1629–1651.
- (73) Quintal, S. M.; de Paula, Q. A.; Farrell, N. P. Zinc Finger Proteins as Templates for Metal Ion Exchange and Ligand Reactivity. Chemical and Biological Consequences. *Metallomics* **2011**, *3* (2), 121–139.
- (74) Brayer, K. J.; Segal, D. J. Keep Your Fingers off My DNA: Protein-Protein Interactions Mediated by C₂H₂ Zinc Finger Domains. *Cell Biochem Biophys* **2008**, *50* (3), 111–131.

- (75) Vistain, L. F.; Yamamoto, N.; Rathore, R.; Cha, P.; Meade, T. J. Targeted Inhibition of Snail Activity in Breast Cancer Cells by Using a CoIII-Ebox Conjugate. *ChemBioChem* **2015**, *16* (14), 2065–2072.
- (76) Skoda, A. M.; Simovic, D.; Karin, V.; Kardum, V.; Vranic, S.; Serman, L. The Role of the Hedgehog Signaling Pathway in Cancer: A Comprehensive Review. *Bosn. J. Basic Med. Sci.* **2018**, *18* (1), 8–20.
- (77) Hanna, A.; Shevde, L. A. Hedgehog Signaling: Modulation of Cancer Properties and Tumor Microenvironment. *Mol. Cancer* **2016**, *15* (1), 24.
- (78) Wu, F.; Zhang, Y.; Sun, B.; McMahon, A. P.; Wang, Y. Hedgehog Signaling: From Basic Biology to Cancer Therapy. *Cell Chem. Biol.* **2017**, *24* (3), 252–280.
- (79) Evangelista, M.; Tian, H.; Sauvage, F. J. de. The Hedgehog Signaling Pathway in Cancer. *Clin. Cancer Res.* **2006**, *12* (20), 5924–5928.
- (80) Rubin, L. L.; Sauvage, F. J. Targeting the Hedgehog Pathway in Cancer. *Nat Rev Drug Discov* **2006**, *5*.
- (81) Gupta, S.; Takebe, N.; LoRusso, P. Targeting the Hedgehog Pathway in Cancer. *Ther Adv Med Oncol* **2010**, *2* (4), 237–250.
- (82) Marigo, V.; Johnson, R. L.; Vortkamp, A.; Tabin, C. J. Sonic Hedgehog Differentially Regulates Expression of GLI and GLI3 during Limb Development. *Dev Biol* **1996**, *180* (1), 273–283.
- (83) Varjosalo, M.; Taipale, J. Hedgehog Signaling. *J. Cell Sci.* **2007**, *120* (1), 3–6.
- (84) Ingham, P. W.; McMahon, A. P. Hedgehog Signaling in Animal Development: Paradigms and Principles. *Genes Dev* **2001**, *15* (23), 3059–3087.
- (85) Ruppert, J. M.; Kinzler, K. W.; Wong, A. J.; Bigner, S. H.; Kao, F. T.; Law, M. L.; Seuanez, H. N.; O'Brien, S. J.; Vogelstein, B. The GLI-Kruppel Family of Human Genes. *Mol Cell Biol* **1988**, *8* (8), 3104–3113.
- (86) Ruppert, J. M.; Vogelstein, B.; Arheden, K.; Kinzler, K. W. GLI3 Encodes a 190-Kilodalton Protein with Multiple Regions of GLI Similarity. *Mol Cell Biol* **1990**, *10* (10), 5408–5415.
- (87) Sasaki, H.; Hui, C.-C.; Nakafuku, M.; Kondoh, H. A Binding Site for Gli Proteins Is Essential for HNF-3 β Floor Plate Enhancer Activity in Transgenics and Can Respond to Shh in Vitro. *Dev. Camb. U K* **1997**, *124* (7), 1313–1322.
- (88) Zeng, H.; Jia, J.; Liu, A. Coordinated Translocation of Mammalian Gli Proteins and Suppressor of Fused to the Primary Cilium. *PLoS ONE* **2010**, *5* (12), e15900.

- (89) M Nakayama; K Tabuchi; Y Nakamura; A Hara. Basal Cell Carcinoma of the Head and Neck. *J. Skin Cancer* **2011**, 2011, Article ID 496910.
- (90) S Sahebjam; LL Siu; AA Razak. The Utility of Hedgehog Signaling Pathway Inhibition for Cancer. *Oncologist* **2012**, 17, 1090–1099.
- (91) S Peukert; K Miller-Moslin. Small-Molecule Inhibitors of the Hedgehog Signaling Pathway as Cancer Therapeutics. *ChemMedChem* **2010**, 5, 500–512.
- (92) Yauch, R. L.; Dijkgraaf, G. J.; Alicke, B.; Januario, T.; Ahn, C. P.; Holcomb, T.; Pujara, K.; Stinson, J.; Callahan, C. A.; Tang, T. Smoothed Mutation Confers Resistance to a Hedgehog Pathway Inhibitor in Medulloblastoma. *Science* **2009**, 326.
- (93) S Buonamici; J Williams; M Morrissey; A Wang; R Guo; A Vattay; K Hsiao; J Yuan; J Green; B Ospina; et al. Interfering with Resistance to Smoothed Antagonists by Inhibition of the PI3K Pathway in Medulloblastoma. *Sci Transl Med* **2012**, 2, 51ra70.
- (94) M Kasper; R Toftgard. Smoothing Out Drug Resistance. *Cancer Cell* **2013**, 23, 3–5.
- (95) J Kim; BT Aftab; JY Tang; D Kim; AH Lee; M Rezaee; J Kim; B Chen; EM King; A Borodovsky; et al. Itraconazole and Arsenic Trioxide Inhibit Hedgehog Pathway Activation and Tumor Growth Associated with Acquired Resistance to Smoothed Antagonists. *Cancer Cell* **2013**, 23, 23–34.
- (96) Ward, E.; DeSantis, C.; Robbins, A.; Kohler, B.; Jemal, A. Childhood and Adolescent Cancer Statistics, 2014. *CA Cancer J Clin* **2014**, 64 (2), 83–103.
- (97) Peris-Bonet, R.; Martinez-Garcia, C.; Lacour, B.; Petrovich, S.; Giner-Ripoll, B.; Navajas, A.; Steliarova-Foucher, E. Childhood Central Nervous System Tumours--Incidence and Survival in Europe (1978-1997): Report from Automated Childhood Cancer Information System Project. *Eur J Cancer* **2006**, 42 (13), 2064–2080.
- (98) Massimino, M.; Biassoni, V.; Gandola, L.; Garre, M. L.; Gatta, G.; Giangaspero, F.; Poggi, G.; Rutkowski, S. Childhood Medulloblastoma. *Crit Rev Oncol Hematol* **2016**, 105, 35–51.
- (99) MacDonald, T. J.; Aguilera, D.; Castellino, R. C. The Rationale for Targeted Therapies in Medulloblastoma. *Neuro Oncol* **2014**, 16 (1), 9–20.
- (100) Northcott, P. A.; Korshunov, A.; Pfister, S. M.; Taylor, M. D. The Clinical Implications of Medulloblastoma Subgroups. *Nat Rev Neurol* **2012**, 8 (6), 340–351.
- (101) Louis, D. N.; Perry, A.; Reifenberger, G.; von Deimling, A.; Figarella-Branger, D.; Cavenee, W. K.; Ohgaki, H.; Wiestler, O. D.; Kleihues, P.; Ellison, D. W. The 2016 World Health Organization Classification of Tumors of the Central Nervous System: A Summary. *Acta Neuropathol* **2016**, 131 (6), 803–820.

- (102) PA Konstantinopoulos; AG Papavassiliou. Seeing the Future of Cancer-Associated Transcription Factor Drug Targets. *J. Am. Med. Assoc.* **2011**, *305*, 2349–2350.
- (103) PL Leong; GA Andrews; DE Johnson; KF Dyer; S Xi; JC Mai; PD Robbins; S Gadiparthi; NA Burke; SF Watkins; et al. Targeted Inhibition of Stat3 with a Decoy Oligonucleotide Abrogates Head and Neck Cancer Cell Growth. *PNAS* **2003**, *100*, 4138–4143.
- (104) M Wiederkehr-Adam; P Ernst; K Mueller; E Bieck; FO Gombert; J Ottl; P Graff; F Grossmueller; MH Heim. Characterization of Phosphopeptide Motifs Specific for the Src Homology 2 Domains of Signal Transducer and Activator of Transcription 1 (STAT1) and STAT3. *J. Biol. Chem.* **2003**, *278*, 16117–16128.
- (105) AZ Ansari; AK Mapp. Modular Design of Artificial Transcription Factors. *Curr. Opin. Chem. Biol.* **2002**, *6*, 765–772.
- (106) R Yaghmai; GR Cutting. Optimized Regulation of Gene Expression Using Artificial Transcription Factors. *Mol. Ther.* **2002**, *5*, 685–694.
- (107) JM Gottesfeld; L Neely; JW Trauger; EE Baird; PB Dervan. Regulation of Gene Expression by Small Molecules. *Nature* **1997**, *387*, 202–205.
- (108) Lauth, M.; Bergstrom, A.; Shimokawa, T.; Toftgard, R. Inhibition of GLI-Mediated Transcription and Tumor Cell Growth by Small-Molecule Antagonists. *Proc Natl Acad Sci U S A* **2007**, *104*.
- (109) Kim, J.; Tang, J. Y.; Gong, R.; Kim, J.; Lee, J. J.; Clemons, K. V.; Chong, C. R.; Chang, K. S.; Fereshteh, M.; Gardner, D.; et al. Itraconazole, a Commonly Used Antifungal That Inhibits Hedgehog Pathway Activity and Cancer Growth. *Cancer Cell* **2010**, *17* (4), 388–399.
- (110) Kim, T. K.; Eberwine, J. H. Mammalian Cell Transfection: The Present and the Future. *Anal. Bioanal. Chem.* **2010**, *397* (8), 3173–3178.
- (111) Hellmann, L. Electrophoretic Mobility Shift Assay (EMSA) for Detecting Protein-Nucleic Acid Interactions. *Nat Protoc* **2007**, *2* (8), 1849–1861.
- (112) Pepinsky, R. B.; Zeng, C.; Wen, D.; Rayhorn, P.; Baker, D. P.; Williams, K. P.; Bixler, S. A.; Ambrose, C. M.; Garber, E. A.; Miatkowski, K.; et al. Identification of a Palmitic Acid-Modified Form of Human Sonic Hedgehog. *J Biol Chem* **1998**, *273* (22), 14037–14045.
- (113) Athar, M.; Li, C.; Tang, X.; Chi, S.; Zhang, X.; Kim, A. L.; Tying, S. K.; Kopelovich, L.; Hebert, J.; Epstein, E. H.; et al. Inhibition of Smoothed Signaling Prevents Ultraviolet B-Induced Basal Cell Carcinomas through Regulation of Fas Expression and Apoptosis. *Cancer Res* **2004**, *64* (20), 7545–7552.
- (114) ATCC. C3H/10T1/2, Clone 8 (ATCC® CCL-226™), Characteristics <https://atcc.org/Products/All/CCL-226.aspx#characteristics> (accessed Oct 8, 2018).

- (115) Product Sheet (ATCC® JHU68™). American Type Culture Collection (ATCC®) 2015.
- (116) David A. Giljohann; Dwight S. Seferos; Weston L. Danial; Matthew D. Massich; Pinal C. Patel; Chad A. Mirkin. Gold Nanoparticles for Biology and Medicine. *Angew Chem Int Ed* **2010**, *49*, 3280–3294.
- (117) D Zheng; DA Giljohann; DL Chen; MD Massich; X-Q Wang; H Iordanov; CA Mirkin; AS Paller. Topical Delivery of SiRNA-Based Spherical Nucleic Acid Nanoparticle Conjugates for Gene Regulation. *PNAS* **2012**, *109*, 11975–11980, S11975/1-S11975/24.
- (118) Cutler, J. I.; Auyeung, E.; Mirkin, C. A. Spherical Nucleic Acids. *J Am Chem Soc* **2012**, *134* (3), 1376–1391.
- (119) Barnaby, S. N.; Sita, T. L.; Petrosko, S. H.; Stegh, A. H.; Mirkin, C. A. Therapeutic Applications of Spherical Nucleic Acids. In *Nanotechnology-Based Precision Tools for the Detection and Treatment of Cancer*; Mirkin, C. A., Meade, T. J., Petrosko, S. H., Stegh, A. H., Eds.; Cancer Treatment and Research; Springer International Publishing: Cham, 2015; pp 23–50.
- (120) Kanasty, R.; Dorkin, J. R.; Vegas, A.; Anderson, D. Delivery Materials for SiRNA Therapeutics. *Nat. Mater.* **2013**, *12* (11), 967–977.
- (121) Rosi, N. L.; Giljohann, D. A.; Thaxton, C. S.; Lytton-Jean, A. K. R.; Han, M. S.; Mirkin, C. A. Oligonucleotide-Modified Gold Nanoparticles for Intracellular Gene Regulation. *Science* **2006**, *312* (5776), 1027–1030.
- (122) Randeria, P. S.; Seeger, M. A.; Wang, X.-Q.; Wilson, H.; Shipp, D.; Mirkin, C. A.; Paller, A. S. SiRNA-Based Spherical Nucleic Acids Reverse Impaired Wound Healing in Diabetic Mice by Ganglioside GM3 Synthase Knockdown. *Proc. Natl. Acad. Sci.* **2015**, *112* (18), 5573–5578.
- (123) Pavletich, N. P.; Pabo, C. O. Crystal Structure of a Five-Finger GLI-DNA Complex: New Perspectives on Zinc Fingers. *Sci. Wash. C 1883-* **1993**, *261* (5129), 1701–1707.
- (124) Elghanian, R.; Storhoff, J. J.; Mucic, R. C.; Letsinger, R. L.; Mirkin, C. A. Selective Colorimetric Detection of Polynucleotides Based on the Distance-Dependent Optical Properties of Gold Nanoparticles. *Science* **1997**, *277* (5329), 1078–1081.
- (125) Hurst, S. J.; Lytton-Jean, A. K. R.; Mirkin, C. A. Maximizing DNA Loading on a Range of Gold Nanoparticle Sizes. *Anal Chem* **2006**, *78* (24), 8313–8318.
- (126) Prigodich, A. E.; Seferos, D. S.; Massich, M. D.; Giljohann, D. A.; Lane, B. C.; Mirkin, C. A. Nano-Flares for mRNA Regulation and Detection. *ACS Nano* **2009**, *3* (8), 2147–2152.
- (127) Nicholls, F. J.; Rotz, M. W.; Ghuman, H.; MacRenaris, K. W.; Meade, T. J.; Modo, M. DNA-Gadolinium-Gold Nanoparticles for in Vivo T1 MR Imaging of Transplanted Human Neural Stem Cells. *Biomaterials* **2016**, *77*, 291–306.

- (128) Barnaby, S. N.; Lee, A.; Mirkin, C. A. Probing the Inherent Stability of siRNA Immobilized on Nanoparticle Constructs. *Proc. Natl. Acad. Sci. U. S. A.* **2014**, *111* (27), 9739–9744.
- (129) Lytton-Jean, A. K. R.; Mirkin, C. A. A Thermodynamic Investigation into the Binding Properties of DNA Functionalized Gold Nanoparticle Probes and Molecular Fluorophore Probes. *J. Am. Chem. Soc.* **2005**, *127* (37), 12754–12755.
- (130) Jin, R.; Wu, G.; Li, Z.; Mirkin, C. A.; Schatz, G. C. What Controls the Melting Properties of DNA-Linked Gold Nanoparticle Assemblies? *J. Am. Chem. Soc.* **2003**, *125* (6), 1643–1654.
- (131) Zwanikken, J. W.; Guo, P.-J.; Mirkin, C. A.; Olvera de la Cruz, M. Local Ionic Environment around Polyvalent Nucleic Acid-Functionalized Nanoparticles. *J Phys Chem C* **2011**, *115* (33), 16368–16373.
- (132) Xu, J.; Craig, S. L. Thermodynamics of DNA Hybridization on Gold Nanoparticles. *J. Am. Chem. Soc.* **2005**, *127* (38), 13227–13231.
- (133) Randeria, P. S.; Jones, M. R.; Kohlstedt, K. L.; Banga, R. J.; Olvera de la Cruz, M.; Schatz, G. C.; Mirkin, C. A. What Controls the Hybridization Thermodynamics of Spherical Nucleic Acids? *J. Am. Chem. Soc.* **2015**, *137* (10), 3486–3489.
- (134) Patel, P. C.; Giljohann, D. A.; Daniel, W. L.; Zheng, D.; Prigodich, A. E.; Mirkin, C. A. Scavenger Receptors Mediate Cellular Uptake of Polyvalent Oligonucleotide-Functionalized Gold Nanoparticles. *Bioconjugate Chem* **2010**, *21* (12), 2250–2256.
- (135) Choi, C. H. J.; Hao, L.; Narayan, S. P.; Auyeung, E.; Mirkin, C. A. Mechanism for the Endocytosis of Spherical Nucleic Acid Nanoparticle Conjugates. *Proc. Natl. Acad. Sci. U. S. A.* **2013**, *110* (19), 7625–7630.
- (136) Hung, A. H.; Holbrook, R. J.; Rotz, M. W.; Glasscock, C. J.; Mansukhani, N. D.; MacRenaris, K. W.; Manus, L. M.; Duch, M. C.; Dam, K. T.; Hersam, M. C.; et al. Graphene Oxide Enhances Cellular Delivery of Hydrophilic Small Molecules by Co-Incubation. *ACS Nano* **2014**, *8* (10), 10168–10177.
- (137) Cao, Y.; Yang, T.; Feng, J.; Wu, P. Decoration of Graphene Oxide Sheets with Luminescent Rare-Earth Complexes. *Carbon* **2011**, *49* (4), 1502–1504.
- (138) Pandey, H.; Parashar, V.; Parashar, R.; Prakash, R.; Ramteke, P. W.; Pandey, A. C. Controlled Drug Release Characteristics and Enhanced Antibacterial Effect of Graphene Nanosheets Containing Gentamicin Sulfate. *Nanoscale* **2011**, *3* (10), 4104–4108.
- (139) Zhang, M.; Yin, B.-C.; Wang, X.-F.; Ye, B.-C. Interaction of Peptides with Graphene Oxide and Its Application for Real-Time Monitoring of Protease Activity. *Chem. Commun. Camb. Engl.* **2011**, *47* (8), 2399–2401.

- (140) Sun, X.; Liu, Z.; Welsher, K.; Robinson, J. T.; Goodwin, A.; Zaric, S.; Dai, H. Nano-Graphene Oxide for Cellular Imaging and Drug Delivery. *Nano Res.* **2008**, *1* (3), 203–212.
- (141) Zhang, L.; Xia, J.; Zhao, Q.; Liu, L.; Zhang, Z. Functional Graphene Oxide as a Nanocarrier for Controlled Loading and Targeted Delivery of Mixed Anticancer Drugs. *Small Weinh. Bergstr. Ger.* **2010**, *6* (4), 537–544.
- (142) Lu, C.-H.; Zhu, C.-L.; Li, J.; Liu, J.-J.; Chen, X.; Yang, H.-H. Using Graphene to Protect DNA from Cleavage during Cellular Delivery. *Chem. Commun.* **2010**, *46* (18), 3116–3118.
- (143) Lu, C.-H.; Yang, H.-H.; Zhu, C.-L.; Chen, X.; Chen, G.-N. A Graphene Platform for Sensing Biomolecules. *Angew. Chem. Int. Ed Engl.* **2009**, *48* (26), 4785–4787.
- (144) Wu, M.; Kempaiah, R.; Huang, P.-J. J.; Maheshwari, V.; Liu, J. Adsorption and Desorption of DNA on Graphene Oxide Studied by Fluorescently Labeled Oligonucleotides. *Langmuir* **2011**, *27* (6), 2731–2738.
- (145) Lu, C.; Huang, P.-J. J.; Liu, B.; Ying, Y.; Liu, J. Comparison of Graphene Oxide and Reduced Graphene Oxide for DNA Adsorption and Sensing. *Langmuir* **2016**, *32* (41), 10776–10783.
- (146) Kim, H.; Namgung, R.; Singha, K.; Oh, I.-K.; Kim, W. J. Graphene Oxide–Polyethylenimine Nanoconstruct as a Gene Delivery Vector and Bioimaging Tool. *Bioconjug. Chem.* **2011**, *22* (12), 2558–2567.
- (147) Longo, P. A.; Kavran, J. M.; Kim, M.-S.; Leahy, D. J. Transient Mammalian Cell Transfection with Polyethylenimine (PEI). *Methods Enzymol.* **2013**, *529*, 227–240.
- (148) Feng, L.; Zhang, S.; Liu, Z. Graphene Based Gene Transfection. *Nanoscale* **2011**, *3* (3), 1252.
- (149) Fakhri, A. Adsorption Characteristics of Graphene Oxide as a Solid Adsorbent for Aniline Removal from Aqueous Solutions: Kinetics, Thermodynamics and Mechanism Studies. *J. Saudi Chem. Soc.* **2017**, *21* (Supplement 1), S52–S57.
- (150) Park, J. S.; Goo, N.-I.; Kim, D.-E. Mechanism of DNA Adsorption and Desorption on Graphene Oxide. *Langmuir* **2014**, *30* (42), 12587–12595.
- (151) Fan, Z.; Po, K. H. L.; Wong, K. K.; Chen, S.; Lau, S. P. Polyethylenimine-Modified Graphene Oxide as a Novel Antibacterial Agent and Its Synergistic Effect with Daptomycin for Methicillin-Resistant Staphylococcus Aureus. *ACS Appl. Nano Mater.* **2018**, *1* (4), 1811–1818.
- (152) Chen, B.; Liu, M.; Zhang, L.; Huang, J.; Yao, J.; Zhang, Z. Polyethylenimine-Functionalized Graphene Oxide as an Efficient Gene Delivery Vector. *J. Mater. Chem.* **2011**, *21* (21), 7736–7741.

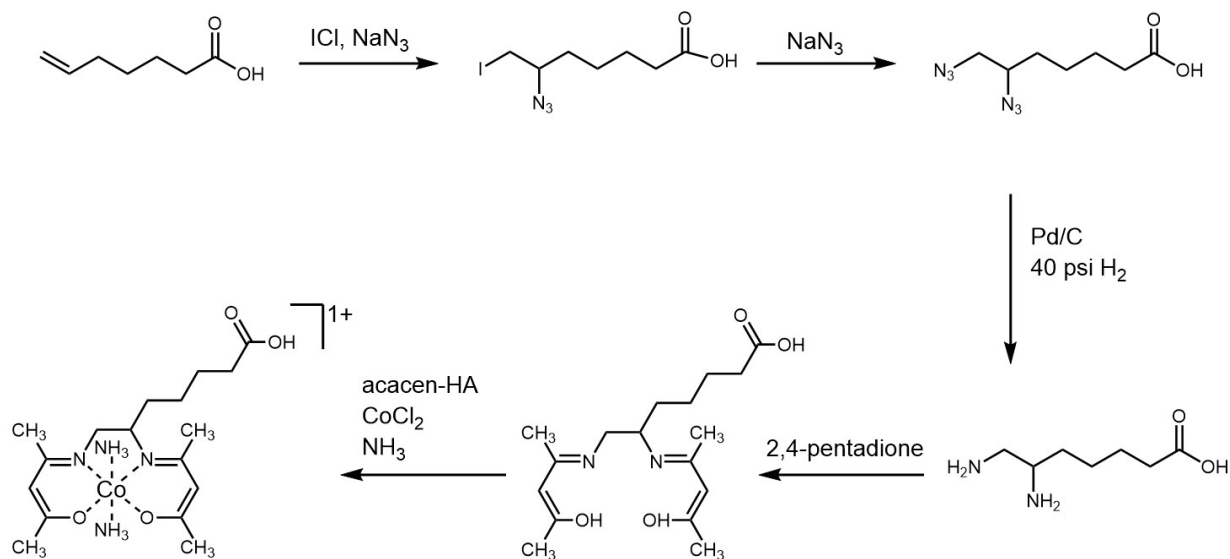
- (153) Song, M.; Xu, J. Preparation of Polyethylenimine-Functionalized Graphene Oxide Composite and Its Application in Electrochemical Ammonia Sensors. *Electroanalysis* **2013**, *25* (2), 523–530.
- (154) Andy Wijaya; Stefan B. Schaffer; Ivan G. Pallares; Kimberly Hamad-Schifferli. Selective Release of Multiple DNA Oligonucleotides from Gold Nanorods. *ACS Nano* **2009**, *3* (1), 80–86.
- (155) Gary B. Braun; Alessia Pallaoro; Guohui Wu; Dimitris Missirlis; Joseph A. Zasadzinski; Matthew Tirrell; Norbert O. Reich. Laser-Activate Gene Silencing *via* Gold Nanoshell-SiRNA Conjugates. *ACS Nano* **2009**, *3* (7), 2007–2015.
- (156) A Barhoumi; R Huschka; R Bardhan; MW Knight; NJ Halas. Light-Induced Release of DNA from Plasmon-Resonant Nanoparticles: Towards Light-Controlled Gene Therapy. *Chem Phys Lett* **2009**, *482*, 171–179.
- (157) Sakari Kauppinen; Birte Vester; Jesper Wengel. Locked Nucleic Acid (LNA): High Affinity Targeting of RNA for Diagnostics and Therapeutics. *Drug Discov. Today Technol.* **2005**, *2* (3), 287–290.
- (158) Daniel, M.-C.; Astruc, D. Gold Nanoparticles: Assembly, Supramolecular Chemistry, Quantum-Size-Related Properties, and Applications toward Biology, Catalysis, and Nanotechnology. *Chem. Rev.* **2004**, *104* (1), 293–346.
- (159) Chowdhury, I.; Duch, M. C.; Mansukhani, N. D.; Hersam, M. C.; Bouchard, D. Colloidal Properties and Stability of Graphene Oxide Nanomaterials in the Aquatic Environment. *Environ. Sci. Technol.* **2013**, *47* (12), 6288–6296.
- (160) Čermák, V. DNA Calculator <http://www.molbiotools.com/dnacalculator> (accessed Oct 17, 2017).
- (161) Mancuso, M.; Pazzaglia, S.; Tanori, M.; Hahn, H.; Merola, P.; Rebessi, S.; Atkinson, M. J.; Di Majo, V.; Covelli, V.; Saran, A. Basal Cell Carcinoma and Its Development: Insights from Radiation-Induced Tumors in Ptc1-Deficient Mice. *Cancer Res* **2004**, *64* (3), 934–941.
- (162) Aszterbaum, M.; Epstein, J.; Oro, A.; Douglas, V.; LeBoit, P. E.; Scott, M. P.; Epstein, E. H. Ultraviolet and Ionizing Radiation Enhance the Growth of BCCs and Trichoblastomas in Patched Heterozygous Knockout Mice. *Nat Med N* **1999**, *5* (11), 1285–1291.
- (163) Frauke Nitzki; Marco Becker; Anke Frommhold; Walter Schulz-Schaeffer; Heidi Hahn. Patched Knockout Mouse Models of Basal Cell Carcinoma. *J. Skin Cancer* **2012**, *2012*, Article ID 907543.
- (164) Hameyer, D.; Loonstra, A.; Eshkind, L.; Schmitt, S.; Antunes, C.; Groen, A.; Bindels, E.; Jonkers, J.; Krimpenfort, P.; Meuwissen, R.; et al. Toxicity of Ligand-Dependent Cre Recombinases and Generation of a Conditional Cre Deleter Mouse Allowing Mosaic Recombination in Peripheral Tissues. *Physiol Genomics* **2007**, *31* (1), 32–41.

(165) Zibat, A.; Uhmann, A.; Nitzki, F.; Wijgerde, M.; Frommhold, A.; Heller, T.; Armstrong, V.; Wojnowski, L.; Quintanilla-Martinez, L.; Reifenberger, J.; et al. Time-Point and Dosage of Gene Inactivation Determine the Tumor Spectrum in Conditional Ptch Knockouts. *Carcinogenesis* **2009**, *30* (6), 918–926.

(166) Vooijs, M.; Jonkers, J.; Berns, A. A Highly Efficient Ligand-Regulated Cre Recombinase Mouse Line Shows That LoxP Recombination Is Position Dependent. *EMBO Rep* **2001**, *2* (4), 292–297.

APPENDIX A: SYNTHESIS OF CO(ACACEN HA) AND CO-DNA

Adapted from prior lab protocols (N. Yamamoto)



Scheme A.1. Synthesis scheme for Co(acacenHA). In brief, 6-heptenoic acid is converted to 6-azido-7-iodoheptanoic acid by addition of iodomonochloride and sodium azide. After purification by flash chromatography, the product is converted to 6,7-diazidoheptanoic acid by addition of additional sodium azide. Following extraction in ether, the product is hydrogenated to yield 6,7-diaminoheptanoic acid. A condensation reaction with 2,4-pentadione is then performed to yield the unmetallated acacenHA ligand (6,7-Heptanoicoacetylacetonatoethylenediamine). The ligand is metallated and ammine axial ligands are added to yield the final product Co(acacenHA) which is used for peptide coupling amine-modified DNA.

A.1. Synthesis of 6-Azido-7-Iodoheptanoic Acid

1.00 mL 6-heptenoic acid (0.946g = 7.38 mmol = 1 equiv, MW= 128.17 g/mol)

0.74 mL iodomonochloride (ICl) (14.8 mmol = 2 equiv, MW= 65.01 g/mol)

~35 mL dry MeCN (solvent system)

Expected yield= 2.19 g

Training: NMR, Flash Chromatography, Extractions, Handling ICL, Rotovap

Preparation:

An appropriately-size RB flask (100 mL), magnetic stir bar, a dropper and a needle for MeCN are placed in the oven for drying. A 1 L solution of 5% (w/w) sodium thiosulfate ($\text{Na}_2\text{S}_2\text{O}_3$) is prepared (to quench ICl). Remove ICl from the refrigerator, slightly unscrew lid, and carefully heat with a heat gun, ensuring both polymorphs are melted (mp= 27.3°C and 19.3°C).

Reaction:

1. NaN_3 is combined in an RB flask (fitted for a dropper) with 10 mL dry MeCN, and cooled to 0°C (ice bath) as the flask is flushed with N_2 .
2. ICl (measured out quickly with a micropipette) is diluted in 15 mL of dry MeCN (solvent system) and transferred to the dropper.

Note: make sure the micropipette is cleaned after use. Quench any materials containing ICl with the $\text{Na}_2\text{S}_2\text{O}_3$ solution until the color goes away.

3. Add the ICl solution to the NaN_3 suspension dropwise over 20 minutes at 0°C under N_2 .
4. Add 2 mL of dry MeCN to wash the dropper and warm the reaction mixture to RT.
5. 6-heptenoic acid is dissolved in 5 mL dry MeCN and transferred to the dropper, then added dropwise to the reaction mixture very, very slowly (over a few hours).
6. Reaction overnight, monitoring the reaction with TLC (1:1 or 3:2 Ethyl Acetate:Hexanes, using bromocresol green stain).

7. 20 mL water is added to dissolve precipitates and prepare for extractions.
8. The water layer is extracted with rounds of 20 mL diethyl ether (cold) until the water layer is clear (collect ether layers).

9. The ether layer is quenched with 50 mL rounds of $\text{Na}_2\text{S}_2\text{O}_3$ until the ICl is completely quenched (usually 1-2X).
10. The ether layer is washed 2X with 50 mL water
11. The ether layer is dried for 1-2 hours over MgSO_4 .
12. The MgSO_4 is filtered off, and the solvents are rotovapped off, leaving the crude product behind. (Note: if any water is left behind with the crude product, it must be rotovapped off with hi-vac.)
13. NMR of the crude product is obtained before proceeding to column.
14. Crude product is purified by flash chromatography (1:1 or 3:2 Ethyl Acetate:Hexanes, TLC against dilute starting material and crude product, staining with bromocresol green).
15. Rotovap in pre-weighed flask to obtain a pale yellow oil.
16. NMR of purified product is obtained.

A.2. Synthesis of 6,7-Diazidoheptanoic Acid

1 equiv of 6-azido-7-iodoheptanoic acid (MW= 297 g/mol)

2.25 equiv of sodium azide (NaN_3) (MW= 65.01 g/mol)

About 15 mL dry DMF

Preparation:

An appropriately-sized RB flask (100 mL), magnetic stir bar, and a needle for DMF are placed in the oven for drying. The oil bath is set to 55°C (This can take some time, make sure it is stable because reaction is sensitive to overheating).

Reaction:

1. NaN_3 is added to an RB flask and flushed with N_2 .
2. 6-azido-iodoheptanoic acid (dried under vacuum) is transferred into the flask with the DMF.
3. The reaction mixture is stirred overnight at 55°C , monitored with 3:2 EtOAc/Hexanes.

4. The reaction mixture is cooled to RT and 50 mL of water is added to dissolve the solids.
5. The mixture is extracted about 4X with 20 mL of ether, and washed 2X with 50 mL of water.
6. The mixture is dried over MgSO_4 for at least half an hour.
7. The sample is separated from the MgSO_4 with a frit, rotovapped in a pre-weighed flask, and analyzed by NMR. Product MW= 212.1 g/mol.

A.3. Synthesis of 6,7-Diaminoheptanoic Acid

6,7-diazidoheptanoic acid (MW= 212.1 g/mol)

1 scoop Pd/C per gram of sample

About 50 mL of MeOH

40-50 psi H_2

Training: Hydrogenator

Preparation:

Sign up to use the hydrogenator

Reaction:

1. 6,7-diazidoheptanoic acid is dissolved in MeOH and transferred to hydrogenator reaction vessel.
2. Pd/C is added to the vessel slowly (bubble reaction mixture with N₂ to avoid sparks).
3. The mixture is reacted at 40-50 psi H₂ overnight
4. Make sure items containing palladium are washed in the palladium waste.

5. The contents of the flask are filtered through a frit with celite on filter paper (about 1/2 inch).
6. The flask is washed through with MeOH and the filtrate is rotovapped at high vacuum in a pre-weighed flask.
7. The crude product is not isolated (difficult to remove MeOH) before proceeding to the subsequent reaction.

A.4. Synthesis of 6,7-Heptanoicoacetylacetonatoethylenediamine (acacenHA)

6,7-diaminoheptanoic acid (assume 1 equivalent of 100% yield from preceding reaction)

2,4-pentadione (2.2 equivalents to 6,7-diazidoheptanoic acid)

About 20 mL of 2:3 MeOH:EtOH

Reaction:

1. 2,4-pentadione is dissolved in half of the MeOH/EtOH in reaction flask fitted for a dropper and cooled to 0°C

2. 6,7-diaminoheptanoic acid is dissolved and transferred with half of the MeOH/EtOH mixture and transferred to a dropper and added to 2,4-pentadione dropwise, as slow as possible (polymerization very likely to happen at this stage if added too quickly, the more dilute the better). Side product is a brown oil that will stick to the wall of the flask.
3. The mixture is warmed to RT and solvent evaporated as much as possible.
4. Recrystallized with hot toluene ---> RT ---> Ice bath/Freezer for maximum recovery.
Note: This recrystallization typically produced very low yield; work is ongoing in the Meade lab to improve this step.

A.5. Synthesis of $[\text{Co}^{\text{III}}(\text{acacenHA})(\text{L})_2]\text{Cl}$

acacenHA (0.20 g = 0.60 mmol = 1 equiv, MW= 324.2 g/mol)

CoCl₂·6H₂O (0.14 g = 0.74 mmol = 1.2 equiv, MW= 237.93 g/mol)

L = NH₃ = 5 mL MeOH bubbled with NH₃

About 20 mL MeOH from the solvent system + 5 mL for the axial ligand solution

Preparation:

Swell sephadex beads (about 6 g) in H₂O overnight

Reaction:

1. Cobalt and acacenHA are combined in a 2- or 3-neck RB flask (100 mL) and purged with nitrogen (3 cycles of N₂/vacuum)
2. 10 mL of the MeOH was added to the flask and heated at 55°C under nitrogen for 30 min

3. 5 mL of MeOH is bubbled with NH₃ gas for 5 min to saturate the solution (or use NH₃ in MeOH premade solution)
4. The NH₃ solution is injected into the reaction vessel and the reaction mixture is stirred for another 2 h at 55°C under N₂
5. The reaction vessel is opened to air and stirred overnight at RT

6. The final product is purified by an SP-Sephadex C25 column, eluting with H₂O, then the collected fractions are lyophilized. Sephadex beads can be evaporated to dryness, then re-dissolved in H₂O.

A.6. Co(acacenHA)-DNA Coupling Reaction

200 equiv of [Co(acacen-HA)(NH₃)₂]Cl (MW= 415 g/mol)

600 equiv of NHS (N-Hydroxysuccinimide) (MW= 115.09 g/mol) *located in C4 bin

600 equiv of DCC (1,3-Dicyclohexylcarbodiimide) (MW=206.33 g/mol) *located in freezer

dry DMF (from solvent system), 400 μL per 100 nmol Gli_{fwd}

1 equiv of Gli_{fwd} (amine-modified)

0.1 M MES Buffer pH 6.0, 540 μL per 100 nmol Gli_{fwd}

Nonbinding Eppendorf tubes (LoBind)

Eppendorf, cat. no. 022431048

Coupling Reaction:

1. Weigh out cobalt complex in a nonbinding tube (nuclease-free LoBind); weigh out NHS and DCC on weigh paper. Combine all three in nonbinding tube.

2. Add dry DMF
3. Parafilm the capped tube and turn end-on-end for 2 hours.
4. Add 1 equiv of the forward strand (with sterile pipette) and the appropriate amount of MES buffer. Re-parafilm and turn end-on-end overnight.

5. Centrifuge the reaction tube at high speed for 10 min. Solid that crashes out is reaction byproduct (urea) and is undesired for next step.
6. Transfer supernatant to a 15 mL falcon tube and centrifuge again as above. Transfer this supernatant into a second 15 mL falcon tube, and that supernatant into a 50 mL falcon tube. Also wash the original Eppendorf tube with 100 μ L sterile water, transferring to each subsequent tube to ensure quantitative transfer of product and maximal removal of solid byproduct.
7. Freeze sample in liquid N₂, then remove solvent via Schlenk line.

A.7. Co-DNA Annealing Reaction (Single Stranded \rightarrow Double Stranded DNA)

1.1 equiv of Gli_{rev} (relative to 1 equiv Gli_{fwd} in coupling reaction)

Sephadex G25 columns (1 for every 100 μ L suspension) IBI scientific, code IB06030

Amicon Ultra 0.5 filters, 3 kDa MWCO Millipore/Amicon, UFC500396

Annealing Reaction

1. Resuspend the lyophilized sample in 3 mL sterile H₂O and transfer to a 15 mL falcon tube. (Note: can resuspend in 1.5 mL, transfer to 15 mL tube, then use additional 1.5 mL to wash original tube and transfer.)

If precipitate is present, centrifuge at high speed for 5 min, transferring supernatant to a 15 mL tube. Repeat such that each tube is washed 1-2x, and the final volume is 3 mL.

2. Add the reverse strand to the sample.
3. Anneal by placing in 95°C heat block for 5 min, then cooling slowly in Styrofoam casing (at least 8 h). Note: 60-70°C should be sufficient, and this temperature has been used successfully as well.
4. Lyophilize

5. (*Spin Column Purification- Optional*)
 - Resuspend lyophilized sample in as little water as possible to avoid using too many G25 columns. Using sonication will help.
 - Allow Sephadex G25 columns (kept in deli fridge) to equilibrate to room temperature, then invert a few times to fully resuspend the gel. Uncap both ends of the column.
 - Dry Sephadex G25 columns according to the manual: centrifuge twice @1,100 rpm for 1min.
 - Add 100 µL sample to each sephadex column, then centrifuge @1,100 rpm for 4 min per manufacturer's instructions.
6. Concentrate the sample in 3 kDa MWCO Amicon filters for subsequent purification by HPLC or size exclusion chromatography. Amicon filters also serve to remove excess small molecule byproducts and impurities.

APPENDIX B: PURIFICATION AND CHARACTERIZATION OF CO-DNA

B.1. Purification of Co-DNA

B.1.1. Purification via Analytical-Scale Ion Exchange HPLC

Dionex DNAPac PA200 Analytical Columns (ThermoFisher P/N 063000) can be used to purify Co-DNA on an analytical scale by ion exchange chromatography. However, the analytical scale column is overloaded by ten-fold the recommended amount; this scale is used because ion exchange buffers should not be used in semi-prep pumps. Moreover, phosphorothioate linkages in Co-DNA lead to poor separation by ion exchange (See Figure B.1). Agilent is unable to provide technical support or advice for such a specified usage.

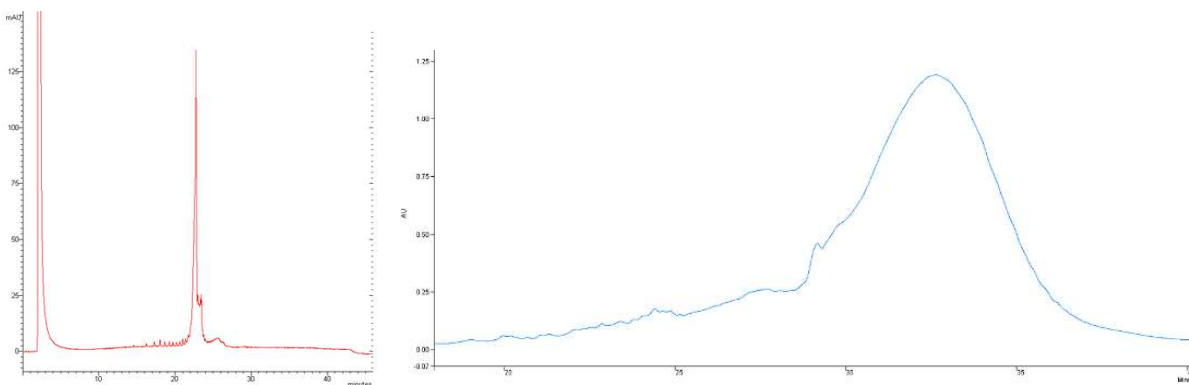


Figure B.1. Dionex ion exchange HPLC traces of Co-DNA without phosphorothioate bonds (left) and with phosphorothioate bonds (right). The presence of phosphorothioate bonds yields poor separation by ion exchange.

If using HPLC purification, using fresh buffers is important. Mobile phase A is 25 mM Tris and 0.5% acetonitrile, pH= 8.0. Mobile phase B is 25 mM Tris, 1.5 M NH_4Cl , and 0.5% acetonitrile, pH= 8.0. Adjust pH with HCl and NH_4OH as needed. Measure with a Tris-compatible

pH probe only (Pinnacle #476436), doing otherwise may cause an undesirable side reaction with the probe's salt bridge and damage the probe.

The protocol for Co-DNA purification by Dionex ion exchange HPLC can be found in Appendix C. Instructions are specific to Meade lab Agilent analytical HPLC. Fractions are collected in falcon tubes by hand, then:

1. Freeze collected fractions in liquid N₂, then put on pump line (place falcon tubes in Pyrex flask) for ~2 hours so that MeCN is removed. Ensure that falcon tubes are large relative to collected volume to prevent against bumping.
2. Re-freeze and lyophilize fractions overnight or until finished.
3. Dissolve in minimal H₂O and desalt on Amicon filters by centrifuging for 30 minutes at 14,000 x g. Repeat multiple times until total volume remaining is <100 μL. (Discard filtrate in Eppendorf tube each time). You may add an additional 400 μL H₂O and spin filter once more to remove excess salts.
4. Invert Amicon filter into new centrifuge tube and centrifuge for 2 minutes at 1,000 x g.
5. If necessary, combine relevant fractions in another Amicon filter and centrifuge 10 minutes at 14,000 x g so that total volume is <100 μL.
6. Determine volume (estimate with a micropipette) and dilute with H₂O to total volume of 100 μL.

B.1.2. Purification via Benchtop Size Exclusion Chromatography

Using NAP-25 size exclusion columns (GE Healthcare Life Sciences illustra NAP-25 Columns) has proved to be a more straightforward and efficacious method of purification. Going forward, this is the recommended method. The manufacturer's protocol was followed, using MES

buffer to elute. Excess storage buffer in column was drained, then column was equilibrated with 25 mL MES buffer. 2.5 mL sample was added and eluted with 3.5 mL MES buffer.

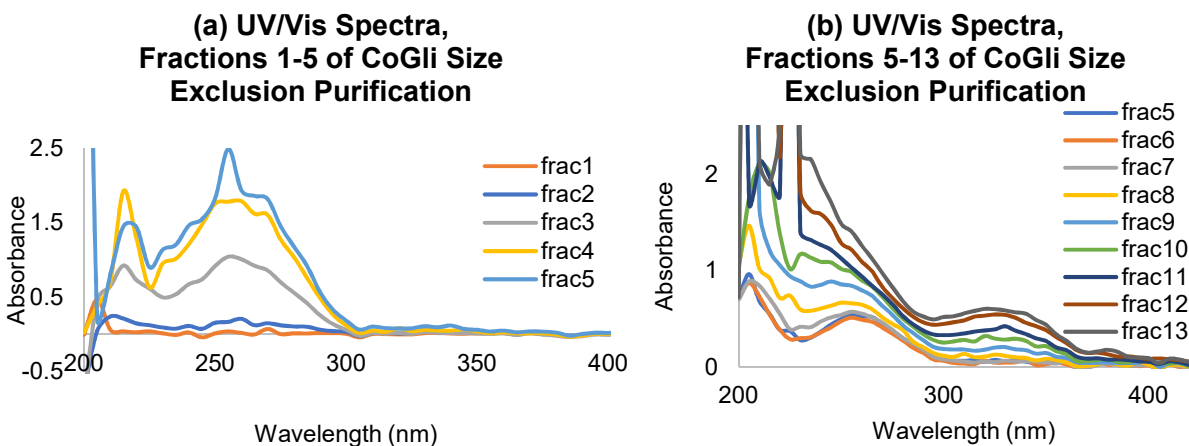


Figure B.2. (a) UV/Vis spectra of eluted CoGli fractions 1-5 from size exclusion chromatography. When comparing against ICP-MS data, fraction 3 was determined to have a Co:DNA ratio close to 1. Spectra were obtained using the 1 mm path length microvolume sample tray, which likely accounts for spectral noise; noise can be decreased by averaging 5-10 scans. (b) UV/Vis spectra of eluted CoGli fractions 5-13 from size exclusion chromatography. In these scans, the concentration of Co(acacenHA) is higher, accounting for the spectral feature at 340 nm. These fractions contained a stoichiometric excess of Co(acacenHA) and were therefore not used.

Fractions of 200-300 μ L were collected and analyzed by UV/Vis and ICP as described in sections B.2.3.1 and B.2.3.2. Figure B.2. shows UV/Vis spectra for all collected fractions. For later fractions, an absorbance band at 340 nm appears, corresponding to the presence of Co(acacenHA). While this band could be used for quantification, these concentrations are in significant excess of the desired stoichiometric ratio of 1:1 dsDNA:Co. Fraction 3 was determined to have a stoichiometric ratio close to 1, and was therefore used for subsequent biological assays. In the future, purer product can likely be obtained by performing Amicon spin filtration (3 kDa MWCO) prior to size exclusion chromatography. Removing additional unbound Co(acacenHA) and other impurities will ensure the column is not overloaded, and separation can be improved.

B.2. Characterization of Co-DNA

B.2.1. Mass Spectrometry

A variety of mass spectrometry (MS) techniques have been used in an attempt to characterize Co-DNA complexes. This section will review methods used their results.

B.2.1.1. Matrix-assisted laser desorption ionization time of flight (MALDI-TOF) MS

MALDI-TOF MS requires use of a matrix solution; the matrix molecule co-precipitates on the MALDI chip with the sample and serves to help ionization. Two common matrix molecules for MALDI of DNA samples are 2',6'-Dihydroxyacetophenone (DHAP) and 3-Hydroxypicolinic acid (3-HPA). To prepare the DHAP matrix solution, 3.3 μ L saturated ammonium citrate aqueous solution were added to 100 μ L 7.5 mg/mL DHAP solution in MeOH. The mixture was vortexed multiple times until a yellow solid precipitated. The remaining liquid DHAP matrix is then co-spotted at a 1:1 v/v ratio with DNA. To prepare the 3-HPA matrix solution, prepare a 50 mg/mL solution of 3-HPA in mH₂O and a 50 mg/mL solution of ammonium citrate in mH₂O. Combine the solutions in a 9:1 v/v 3-HPA:ammonium citrate ratio to yield the final matrix.

When analyzing oligonucleotides with MALDI, the laser may cause depurination and a concomitant decrease in observed m/z. Additionally, phosphorothioate bonds may undergo oxidation, causing a decrease in 16 Da per oxidized bond. Gli fwd target mass= 5443.9 Da. Gli rev target mass= 5309.8 Da. CoGli target mass= 11,116.8 Da. Upon analyzing these samples with MALDI-TOF-MS, the observed peaks were: Gli fwd= 5443.9; Gli rev= 5312.4; CoGli= 5314.6, 5311.4. Thus, the identity of Gli fwd and Gli rev can be satisfactorily confirmed, with no depurination or oxidation of phosphorothioate bonds. However, the presence of CoGli cannot be

determined, as these peaks most likely correspond to single-stranded Gli rev. To determine whether Co(acacenHA) is successfully coupled to DNA, consider that a dimer of ssDNA should exhibit a peak around 10,600 m/z, while dsDNA minus Co(acacenHA) should exhibit a peak around 10,800 m/z. However, the spectra show no consistent peaks in these regions, and there is a good deal of variability between runs. Thus, CoGli was not successfully detected by MALDI-MS. A representative MALDI spectrum of CoGli is shown in Figure B.3.

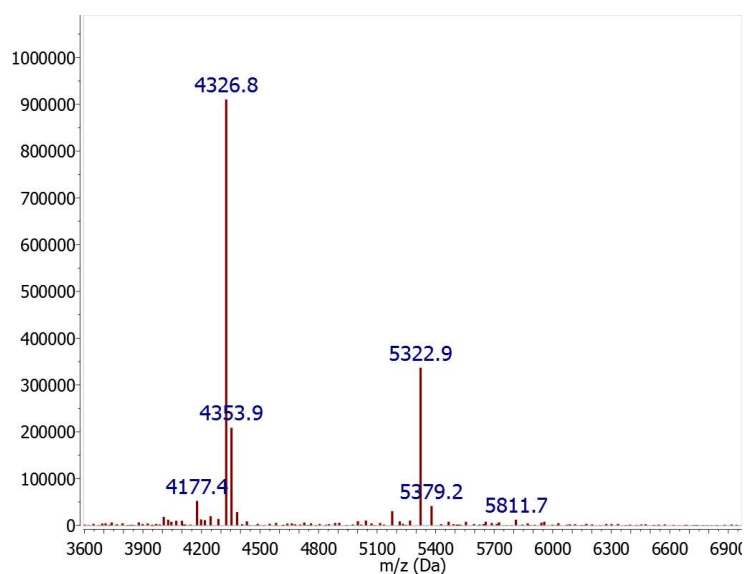


Figure B.3. A representative MALDI-MS spectrum of CoGli. The peak at 5322.9 is similar to (but not precisely) the mass of Gli rev= 5309.8. The identity of the peak at 4326.8 is unknown.

Despite the inability to detect CoGli directly, it was nonetheless possible to distinguish between dsCoGli and ssCoGli by MALDI-MS. For dsCoGli, the doubly charged peak was seen at $m/z = 5,300 - 5,350$ while the singly charged peak was seen at $m/z = 10,696 - 10,720$. For ssCoGli, the doubly charged peak was seen at $m/z = 5,508 - 5,700$ while the singly charged peak was seen at $m/z = 11,248 - 11,550$. Figure B.4 shows a summary of results from four dsCoGli and two ssCoGli samples.

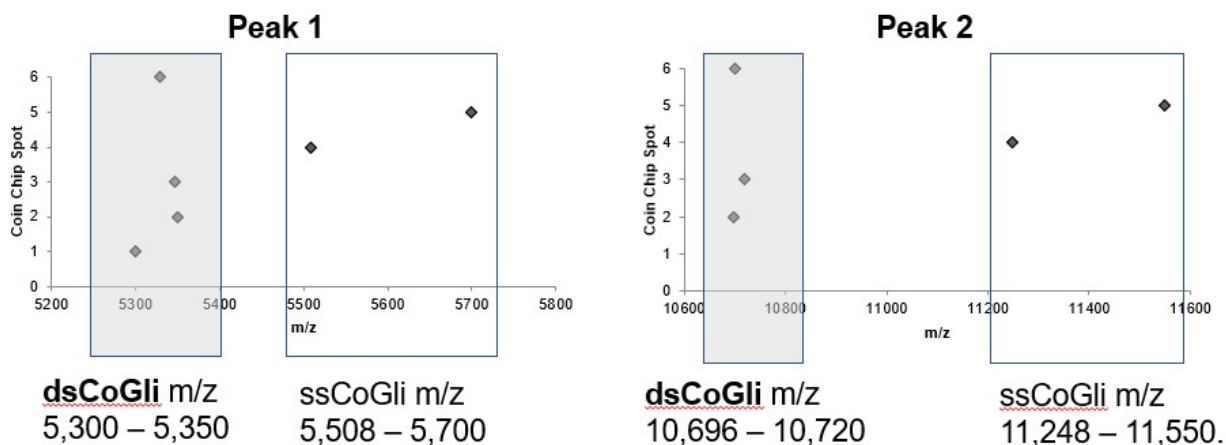


Figure B.4. An analysis of six MALDI samples (four dsCoGli and two ssCoGli) demonstrates that while peaks do not exactly match one another or the target mass, common groupings are seen for dsCoGli and ssCoGli. Peak 1 indicates the singly charged species; while Peak 2 indicates the doubly charged species.

B.2.1.2. Electrospray Ionization (ESI) MS

Using Northwestern's Amazon X ESI-MS, a sample of 5×10^{-7} M CoGli in water was analyzed using a standard small molecule method. The deconvolution report showed a triply charged peak at 771.50 m/z, but nothing in the mass region of interest. Thus, the oligonucleotide method was used instead; this method utilizes a column where mobile phase A= water/hexafluoroisopropanol/triethylamine and mobile phase B= methanol. 20 μ L of 0.5 μ M CoGli were injected, and the run time was 15 min. A peak at 5309.90 was found using MaxEnt deconvolution software, and corresponds to the expected mass of single-stranded Gli rev ($m=$ 5310.1 Da). CoGli was not successfully detected by ESI-MS.

B.2.2. DNA Melting Temperature Analysis

By observing a DNA sample's absorbance at 260 nm as the temperature is gradually

increase, it is possible to observe dehybridization of dsDNA due to an increase in chromicity upon melting. A sample of CoGli was analyzed with temperature ramping from 20°C to 80°C over a period of several hours. Figure B.5. shows an increase in chromicity upon increasing the temperature, verifying that CoGli DNA is double stranded.

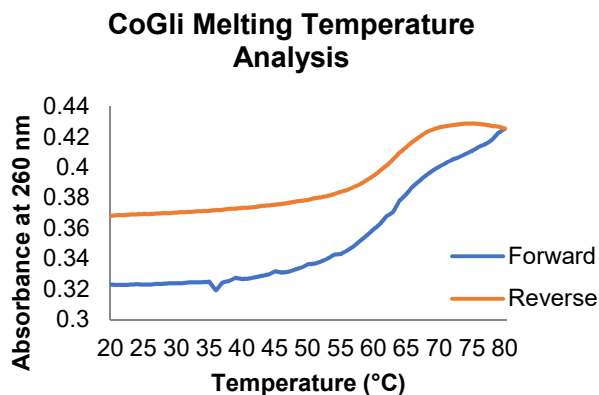


Figure B.5. Melting temperature analysis of CoGli verifies the double-stranded nature of the DNA. An increase in chromicity at 260 nm is observed with increasing temperature, indicating dehybridization of DNA. “Forward” trace indicates the trend with temperature ramping up, while “Reverse” trace indicates trend with temperature ramping down.

B.2.3. Cobalt:DNA Ratio

Given the poor success of direct detection of Co-DNA by mass spectrometry, purity is best assessed by determination of the cobalt:DNA ratio. In a given sample, cobalt concentration can be measured by inductively-coupled plasma mass spectrometry (ICP-MS). The DNA concentration can be measured by ICP-MS or UV/Vis.

B.2.3.1. Analyzing DNA Concentration by UV/Vis

Sample can typically be diluted 1:100 (2µL in 198µL or 1µl in 99µl) for use in 1 cm path length cuvette. Alternatively, sample can be used undiluted in microvolume sample cell (0.1 cm

or 0.02 cm path length). If microvolume sample cell is used, data is typically noisier and an average of 5-10 scans should be performed to ensure accuracy. Measure absorbance of samples at 260 nm and calculate concentration using the Beer's law equation (2) below:

$$A = \epsilon c \quad (2)$$

for Gli _{fwd}(phosphorothioate), $\epsilon = 149,200 \text{ L}/(\text{mol}\cdot\text{cm})$

for Gli _{rev}(phosphorothioate), $\epsilon = 175,300 \text{ L}/(\text{mol}\cdot\text{cm})$

for coupled Co-Gli(phosph), $\epsilon = 0.020 (\mu\text{g}/\text{mL})^{-1}\text{cm}^{-1}$ MW= 10,752g/mol

The extinction coefficient ϵ of free dsGli can be determined using equations (3) and (4) below:

$$\epsilon_{\text{ds}} = (1 - h_{260})(\epsilon_1 + \epsilon_2) \quad (3)$$

$$h_{260} = (0.287 \times f_{\text{AT}}) + (0.059 \times f_{\text{GC}}) \quad (4)$$

Where ϵ_{ds} is the extinction coefficient of double stranded DNA, ϵ_1 and ϵ_2 are the extinction coefficients of the two single strands of DNA, and f_{AT} and f_{GC} are the fraction of AT and GC base pairs, respectively. For Gli consensus sequence DNA (5'-AGAGACCACCCAGGTAG-3') and its complement (3'-TCTCTGGTGGGTCCATC-5'), the calculation yields $\epsilon_{\text{dsGli}} = 274,890 \text{ L}/(\text{mol}\cdot\text{cm})$.

B.2.3.2. Analyzing Co and P Concentrations by ICP-MS

To prepare ICP samples, combine 100 μL HNO_3 and 1 μL sample in a 15 mL falcon tube. Prepare samples in duplicate or triplicate. Vortex the mixture thoroughly and place in hot water bath (60°C) for 4-5 hours or overnight. Upon removing from water bath, let cool then add H_2O to a final volume of 3 or more mL. Submit samples to QBIC for analysis of Co and P content. Note that phosphorus is a very common contaminant, so metal-free tubes should be used, and care

should be taken when preparing samples. For this reason, UV/Vis is the preferred method for assessing DNA concentration.

APPENDIX C: PROTOCOL FOR CO-DNA PURIFICATION BY DIONEX ION EXCHANGE HPLC

Dionex protocol

Weekend and Monday: All day HPLC

Tues-Fri: 2pm-Evening HPLC

(All other times for MS)

Book on calendar and sign log book

Let one of the people in charge of HPLC know that a Dionex column will be run so that they will be prepared to wash the system out the following day

- 1) Turn all instruments on (should already be on), then turn on computer
- 2) On LC valve on LHS of MS, push black button to change mode:
 - i. Yellow → Load (MS): Direct injection into MS (this mode for Dionex)
 - ii. Green → Inject (HPLC): HPLC
- 3) Make sure ELSD is on stdby mode (press < button to go to mode, then ^ to go to stdby if it is in run mode)
- 4) On computer screen, click top button (system control) on menu bar
- 5) Go to Windows → find all the modules:
 - i. Prostar: Pumps
 - ii. 363.34: Fluorescence detector
 - iii. Column valve module: Solvents (Normally, A: aqueous, B: organic. For Dionex, use A: buffer without salt (25 mM Tris), B: buffer with salt (25 mM Tris + 1.5 M NH₄Cl) (for dionex, both are no.3 in column valve module – do not change this just yet))
 - iv. 410: Auto-sampler (don't touch)
 - v. Quad: MS
- 6) Turn on detectors:
 - i. 335.44 (UV-Vis): Go to options → Lamp operations → Lamp on
 - ii. 363.34 (Fluorescence): Same as above - Lamp on
 - iii. Quad (MS): Turn on 'spray' (top left corner) then detector on (gray circle on top menu bar, next to print icon) (NB MS not used for running but need to be on for the method to activate)
- 7) Wash out system first;
 - i. Remove column already on there
 - ii. Replace with union (in tool box, bottom right corner)
 - iii. Uncap at top of guard, cap asap with lid from union
 - iv. Normally connect the inlet to the column into the splitter (ie side), but for Dionex, bypass MS and go straight into the UV-Vis detector (ie remove connection at bottom of splitter and connect union onto this)
 - v. Disconnect between fluorescence detector outlet and ELSD for sample collection
 - vi. Put waste tube (long tubing) into Dionex HPLC waste
 - vii. In Prostar dynamax window, click Manual Control
 - viii. Go to column valve module → Manual control → Change B to H₂O
 - ix. Go to main window → Manual control
 - 10% A (H₂O):90%B(H₂O)
 - Ramp time: 0
 - Flow rate: 3 mL/min
 - x. Wash for 10 mins
 - xi. Stop pumps
 - xii. Go to Column valve module → Manual control → Change both A and B to dionex solvents (as specified in 5iii). Solvent B should still be storage buffer at this point.
 - xiii. Run at 100%A (Buffer A):0%B (Storage buffer) for 10 mins. Check there are no air bubbles in the solvent reservoirs/tubing → prime if necessary!! → Stop pumps, unscrew the nuts from pumps (use two wrenches, one small and one large, one to hold the larger portion on bottom and the other to unscrew the smaller part on top)
 - xiv. After 10 mins, go to 100% B (Storage buffer). Run for 10 mins. → water will well out, so stick syringe in and pull
 - xv. Change flow rate to 1 mL/min → screw piece on. Repeat with other pump
- 8) Open bypass valve

- 
- 9) Attach Dionex column
 - 10) Close bypass valve (let solvent drip through column before attaching to detectors)
 - 11) Ramp to 80%A (Buffer A):20% B (Storage buffer) over 3 mins, run for 3 mins. This is the closest mixture for the starting conditions of the method.
 - 12) Stop pumps
 - 13) Physically change over pump B filter from storage buffer to running buffer.
 - 14) Ramp to 90% A (Buffer A):10%B (Running buffer) over 3 mins.
 - 15) Let wash for 10 mins.
 - 16) Ramp to 30%A (Buffer A):70%B (Running buffer) over 3 mins, run for 5-10 mins
 - 17) Ramp to 90%A (Buffer A):10%B (Running buffer). Run for 5-10 minutes to equilibrate.
 - 18) Hit "End manual control"
 - 19) Go to methods (second button in menu bar on LHS of desktop) to create/alter any methods
 - 20) Open folder icon on top menu bar → choose method and activate
 - 21) From File → Open sample list
 - i. Sample type: Analysis (if you're running a new method, then 'Activate method' should be chosen, then Analysis line after it.)
 - ii. Inj mode: Partial loopfill
 - iii. Inj vol: 10 uL for H₂O, but 50 uL max for samples
 - iv. Specify the vial no.
 - 22) Check all the modules are ready → Press "begin" in sample list (activates method again)
 - 23) Wait for run to finish

For Dionex:

- 24) [Optional] Can do a blank run with Co-Ebox-Blank method (milliQ water is usually in slot 84)
- 25) [Optional] For first injection of sample, dilute sample 25uL:25uL (or whatever desired ratio as long as total volume is 50 uL) in milliQ water
- 26) Run sample using method: Co-Ebox 8-01-10
- 27) When run is finished, clean system to get rid of salts!!!!
 - i. Ramp to 100%A over 3 mins
 - ii. When A is 100%, swap filter in running buffer to storage buffer and ramp to 100%B (Storage buffer) over 3 mins. Equilibrate for 10 mins.
 - iii. Stop pumps
 - iv. Remove column, replace with union
 - v. Change solvents in column valve module to A:H₂O and B:H₂O
 - vi. Bring up Dionex-clean up sample list and hit begin (H₂O:MeOH → H₂O:H₂O → H₂O:MeOH → H₂O:ACN → pump stop). This can be left to complete overnight.
 - vii. After HPLC people have washed the pumps and brought the system back to ACN, change column back.
 - viii. Reattach all the tubing (including the one between Fluorescence detector and ELSD)
 - ix. Make sure all instruments (UV-Vis, Fluorescence and MS) are turned off the next day.

End Manual
control

APPENDIX D: PRELIMINARY qPCR STUDIES IN ASZ CELLS

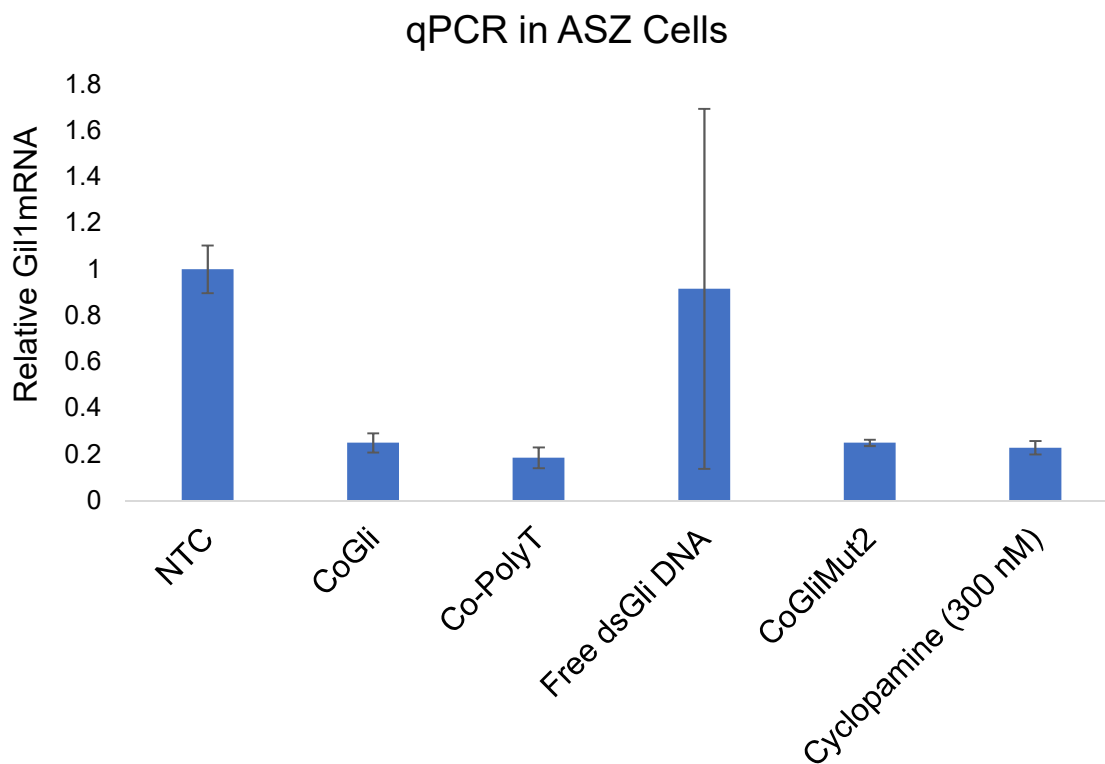


Figure D.1. ASZ cells were serum-starved to induce Hh pathway signaling and treated with CoGli/transfection agent as well as relevant controls (see Figure 18). Treatments were 200 nM unless otherwise indicated. Cells were harvested in TRIZol and analyzed by qPCR for Gli1 mRNA levels, normalizing to TUBB. CoGli, Co-PolyT, and CoGliMut2 all decreased Gli1 mRNA levels as much as the known Smo inhibitor cyclopamine. Free dsGli DNA did not exhibit an inhibitory effect, unlike results seen in NIH/3T3 Shh light II cells. While it is unclear why Co-PolyT and CoGliMut are inhibiting so effectively, these preliminary results are promising. Future work will include a concentration-dependent study to determine whether 200 nM is simply too much of any Co(acacenHA) agent.

APPENDIX E: PROTOCOL FOR CHELEXING FBS FOR USE IN ASZ, BSZ CELL CULTURE MEDIA

This protocol uses Chelex-100 to remove calcium from serum for culturing keratinocytes in low calcium medium. Adjusting the pH of the Chelex may take several hours so start the procedure early in the morning. Adapted from M. Denning/ A. Huen/ R. Hobbs 2008.

- Weigh out 50g Chelex resin (Bio-Rad 142-1253) for 500mL serum
- Wash beads (each wash is 20 min with slow stirring) with 10X the bead volume
 - mH₂O
 - 1 M HCl
 - 1 M NaOH
 - mH₂O; Beads are now ready for use or can be stored at room temperature for later use. Note: Number of times the resin can be regenerated before losing effectiveness has not been determined.
 - 0.5M sodium acetate (20 min)
- Allow to settle, decant sodium acetate
- Equilibrate with PBS (5-10 min)
- Decant, equilibrate with PBS again
- Check pH of slurry; should be ≥ 7.4
 - Adjust pH with HCl if necessary. Allow chelex to equilibrate 5-10 minutes each time after adding HCl.

- Allow to settle, decant liquid
- Wash with mH₂O
- Re-check pH to ensure it is 7.4
- Mix equilibrated chelex with appropriate amount of FBS (50g chelex/500mL FBS, or 5g chelex/50mL FBS)
 - Set aside some FBS as non-chelexed standard
 - Stir for 1 hour at room temp
- Decant chelexed FBS and filter sterilize
- Repeat steps 2-5 to regenerate and store the chelex resin (mH₂O, 1 M HCl, 1 M NaOH, mH₂O)
- Determine calcium concentration via ICP-MS

APPENDIX F: CULTURING ASZ AND BSZ CELL LINES

Adapted from Epstein Lab protocol, Jan. 2011

F.1. Cell Growth Media

To Gibco M154F media (500ml total), add the following and filter sterilize:

- 125 μ l CaCl₂ (supplied w/media; final concentration will be 0.05mM Ca²⁺),
- 5ml penicillin-streptomycin (PS) 100x,
- 10ml chelexed heat-inactivated FBS

Store media at 4°C

F.2. Cell Cryofreezing Media

Freezing media consists of the following:

- 90% Heat-inactivated and chelexed FBS, filter sterilized
- 10% DMSO

F.3. Maintenance and splitting of cells

1. Warm media and buffers in 37°C water bath prior to use

2. Aspirate media with glass pipette

3. Wash cells 2X with DPBS

-Add DPBS (2ml for T25; 5ml for T75; 10ml for T175), rock flask back and forth

-Aspirate immediately with glass pipette

-Add DPBS again; rock back and forth

-Incubate cells in DPBS at 37°C for 10 min

-Aspirate with glass pipette

4. Add TrypLE™ Express Enzyme (1X), no phenol red (ThermoFisher 12604013) (1ml for T25; 2ml for T75; 5ml for T175). Making sure bottom of flask is coated, incubate for ~10-12min at 37°C. Tap flask at end of incubation to loosen cells.
5. After 8-9 min, check whether cells have detached from bottom of flask. The vast majority of cells should move if you swirl the liquid in the flask. If there are still cells attached to the bottom, tap again and leave an extra 1 or 2 min in incubator.
6. When most cells are detached, add media to neutralize (4ml for T25; 8ml for T75; 10ml for T175), pipetting up and down to mix.
7. Transfer to 15ml tube for counting.
8. Spin @ 200 rcf for 10 min, then dispose supernatant w/glass pipette. Note: because growth media contains only 2% serum, spinning down to remove TrypLE is necessary for cell survival.
9. Thoroughly resuspend cells in appropriate volume of media, i.e. a volume that will give you $\sim 1 \times 10^6$ cells (pipette up and down very forcefully to break up clumps as much as possible).
10. Add fresh media (final volume of 5 mL in T25; 15 mL in T75; 30 mL in T175); label flask with cell line, passage number, and date.
11. Transfer desired number of cells into corresponding flask.
12. Rock flask back and forth to evenly distribute cells on bottom of flask; keep in incubator.

APPENDIX G: GOLD NANOPARTICLE SYNTHESIS PROTOCOL

Adapted from electronic protocol by Emma Coughlin

G.1. Reaction Equivalents for 13 nm AuNP (Table G.1.)

Compound	Formula	CAS #	MW (g/mol)	mole equiv.	Mass (g)
Gold (III) chloride trihydrate	$\text{HAuCl}_4 \cdot 3\text{H}_2\text{O}$	16961-25-4	393.83	1	0.198
Sodium citrate tribasic dihydrate	$\text{HOC}(\text{COONa})(\text{CH}_2\text{COONa})_2 \cdot 2\text{H}_2\text{O}$	6132-04-3	294.1	3.87	0.611

G.2. Equipment and Glassware Needed

Equipment needed includes:

- Heating mantle
- Stir plate and stir bar
- Teflon tape
- Condenser tubing

Glassware needed includes a condenser, fritted filter with clamp and filter flask, glass stopper, 1000 mL two neck round bottom flask, 500 mL volumetric flask, 1000 mL graduated cylinder, glass funnel, and large beaker. These items are depicted in Figure D.1.

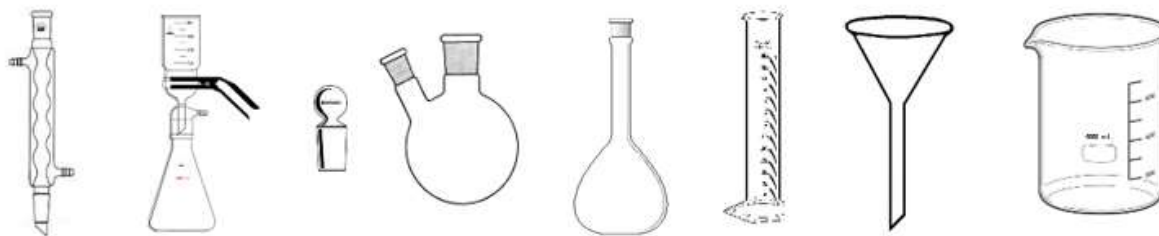


Figure G.1. Required glassware for AuNP synthesis

G.3. Procedure

1. Thoroughly wash all glassware and the stir bar with aqua regia before using
 - * Aqua regia: dissolves trace metals, 3:1 ratio HCl:HNO₃
 - * Any contaminants will cause the NPs to aggregate during formation
 - * Place Na or K Carbonate in the beaker for quenching and rinse waste
2. Place the condenser, funnel/frit, round bottom, stopper and stir bar in the oven overnight.
3. Cool the glassware and cover the bottom of the condenser and the stopper with Teflon tape.
4. Assemble the glassware for reflux, see Figure D.2. and add ~300 mL of Millipore Water to the flask (note the amount of water so the total can be 500 mL)

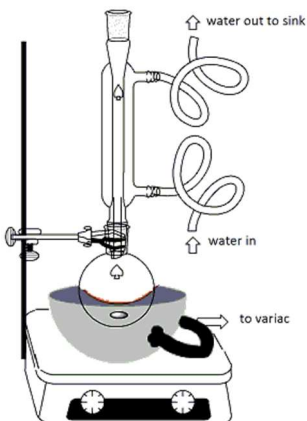


Figure G.2. Reflux setup for glassware for AuNP synthesis

5. Weigh out gold III chloride. Dissolve quickly in a known amount of H₂O.
6. Add the gold III chloride and heat until there is a steady reflux (~30 min) at 70 volts on the heating mantle.
7. Weigh out the calculated amount of NaCitrate and dissolve in a known amount of H₂O (~5 mL).
8. Add remaining H₂O into the two-neck flask (Total – Step 3 – Step 4)

9. Add the NaCitrates as quickly as possible
 - a. Solution should go from gold color to black to dark red
10. Let stir heated for ~15 min
11. Turn off the heat and let cool to handling temp, ~1 h
12. Filter to remove any particles that formed too large (450 μm Cellulose Acetate Filter)
13. Store in a clean glass bottle in the dark at room temp for 3-4 months.
14. Filter with a 0.2 μm Cellulose Acetate filter before using.

G.4. Reaction Equivalents for Various AuNP Sizes

Other sizes of AuNPs are synthesized by adjusting the ratio of gold (III) to NaCitrates, as shown in Table G.2. below.

Table G.2. Gold to NaCitrates Ratio for Synthesizing AuNP of Various Sizes

Size (nm)	HAuCl ₄ (mg)	Na ₃ Cit (mg)	HAuCl ₄ (mmol)	Na ₃ Cit (mmol)	Total H ₂ O (mL)
13	197.00	570.50	0.50	1.94	500
15	197.00	600.00	0.50	2.04	500
18	197.00	85.58	0.50	0.29	500
30	197.00	57.05	0.50	0.19	500
50	197.00	28.53	0.50	0.10	500
100	197.00	17.12	0.50	0.06	500

APPENDIX H: PRELIMINARY WORK WITH 3D ORGANOTYPIC KERATINOCYTE CULTURES

H.1. Experimental Setup

Organotypic skin culture of primary keratinocytes were grown by Dr. Bethany Perez-White at NU's Skin Disease Research Center (SDRC) downtown. 8 cultures were grown and subjected to a total of 4 conditions, as summarized below.

Samples 1 and 2: Non-treated control (NTC)

Samples 3 and 4: Full serum + 100 nM SAG

Samples 5 and 6: Serum starvation + 100 nM SAG

Samples 7 and 8: Serum starvation + 50 nM SAG.

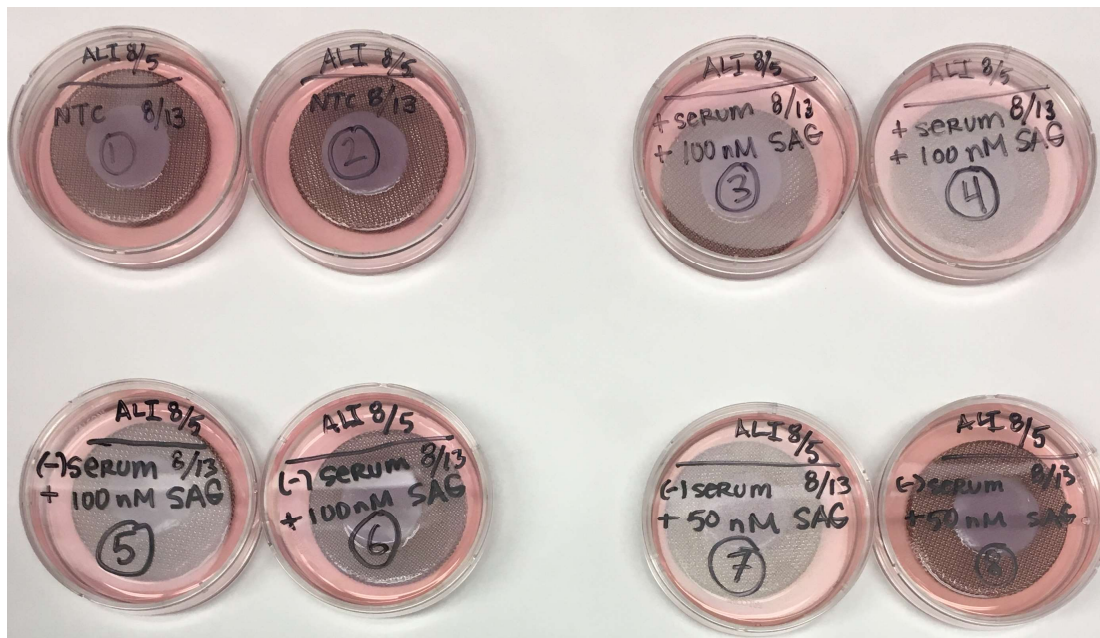


Figure H.1. Organotypic cultures of primary keratinocyte (neonatal foreskin). Meade/Perez White/SDRC Collaboration 08-05-2018. 3D Reconstituted Human Skin, Experiment #1. Day 0 (08-05-2018 start of culture at the air-liquid interface [ALI]), Treatments started 08-13-2018, Day 8. PURPOSE: To define parameters for activation of Hh pathway

H.2. Protocol

On 8/17/2018, cultures were harvested by Elizabeth Bajema and Meghan Ward. The culture was carefully removed from the grid and dissected into three pieces. One portion was frozen in OCT (optimal cutting temperature) compound for later use, another was stored in formalin, and the third was removed from the collagen support and digested in TRIzol for qPCR analysis.

H.3. qPCR Results

Although error bars are large, the trend roughly follows expectations. It is known that serum starvation is required for initiation of Hh pathway signaling, so -serum/+ 100 nM SAG was expected to have the highest Gli1 mRNA levels.

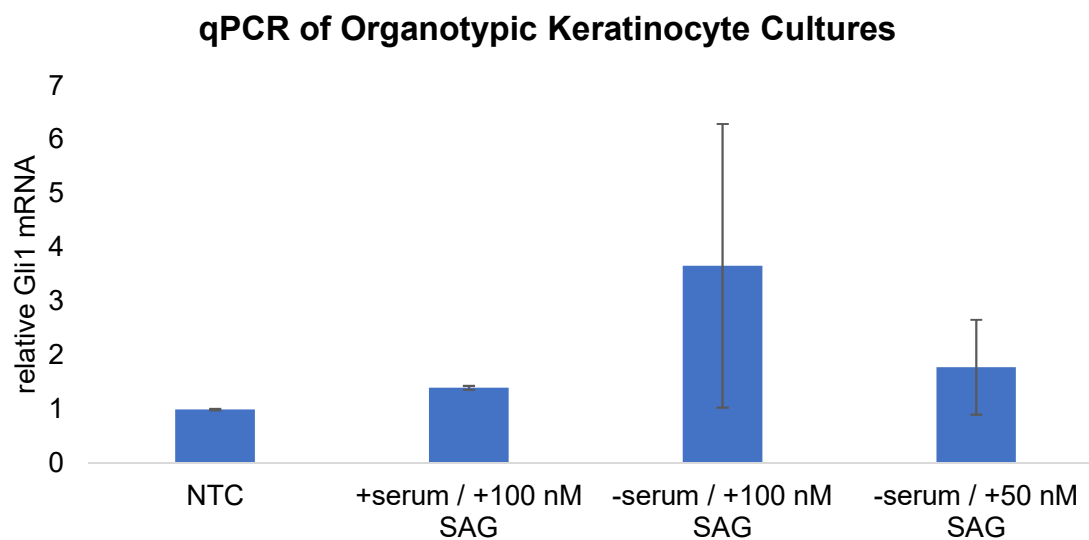


Figure H.2. qPCR results for organotypic cultures, were n=2 for each treatment condition. Samples were analyzed for Gli1 mRNA levels and normalized to TUBB.

APPENDIX I: IACUC-APPROVED IN VIVO STUDY, MOUSE MODEL OF BCC

I.1. Rationale and Experimental Approach

A number of mouse models for BCC have been developed, each of which presents different advantages and disadvantages. Conventional BCC models involve using a heterozygous *Ptch* $-/+$ line and irradiating them with UV exposure three times/week for up to 32 weeks.^{113,161,162} In these lines, BCC tumors develop in a subset of mice, as do medulloblastomas and other cancers that can limit the animals' lifetimes. Moreover, BCC lesions develop at various timepoints and are histologically heterogeneous, likely due to chronic UV exposure.¹⁶³ In order to avoid these setbacks, I planned to use a published mouse model that develops BCC tumors spontaneously in 100% of animals after induction with tamoxifen.¹⁶³⁻¹⁶⁵

This mouse model requires breeding two transgenic mice together, as described below. Experienced animal scientists at Northwestern's Developmental Therapeutics Core (DTC) can provide help with mouse breeding procedures.

Parent 1: A transgenic *Rosa26CreERT2* mouse (The Jackson Laboratory, strain B6.129-Gt(ROSA)26Sortm1(cre/ERT2)Tyj/J, Stock No. 008463)

Parent 2: A *Ptch*flox/flox mouse, generated by crossing two stock *Ptch*flox mice (The Jackson Laboratory, strain B6N.129-*Ptch*1tm1Hahn/J, Stock No. 012457)

The offspring of parents 1 and 2 will yield the desired mice for this study: *Ptch*flox/floxERT2 $+/-$. Parent 1 provides the *Rosa26CreERT2* gene, which expresses Cre-recombinase upon induction with tamoxifen.^{164,166} When Cre-recombinase is expressed, it recognizes and removes the *Ptch* gene because it is flanked by LoxP (this is why a homozygous *Ptch*flox/flox mouse is required as parent 2). Removal of the *Ptch* gene in these mice yields expression of BCC tumors in 100% of

animals. The tumors are reported to preferentially grow on ears and tails, and are fully developed at 90 days.¹⁶⁵

The experimental mice (Ptchflox/floxERT2+/-) will be given a single intramuscular injection of 100µg tamoxifen. Because tumor growth is induced by tamoxifen, not irradiation, tumors will progress in the same time frame and will be histologically homogeneous, allowing for specific study of Hh pathway-induced tumors in mouse models.¹⁶³ This will remove a measure of error that would otherwise be present in non-homogenous tumor models. From days 45-90 after tamoxifen injection, mouse BCC tumors will be treated with a topical treatment of AuGliCo, or other promising nanoconstruct. The treatment protocol must be optimized prior to in vivo work; laser irradiation may or may not be necessary depending on design of nanoconstruct. Once the process is optimized, mouse tumors will be treated over multiple days with AuGliCo or other agent and observe the effects. Success of the treatment will be determined by measuring tumor size, with successful treatments shrinking or eliminating the tumor.

This mouse study will be an in vivo study intended to demonstrate the use and effectiveness of CoGli for treating BCC tumors. Control groups and target groups will consist of 6 or 3 animals, depending on the importance of that control. The controls used will involve testing the various components of the nanoconstruct (AuNP, GO, CoGli, CoGliFluor) to ensure that no negative side effects or unexpected patterns are observed. No toxicity is expected for any of the compounds, and only CoGli and CoGliFluor will cause a decrease in tumor size.

I.2. Vertebrate Animals Section Information

Point 1: Animals to be Used

Summary of Procedures

This study requires the use of transgenic mice that will develop basal cell carcinoma (BCC) upon induction with tamoxifen. To generate these mice, I will cross the following two strains, according to published protocol:

Parent 1: A transgenic *Rosa26CreERT2* mouse (The Jackson Laboratory, strain *B6.129-Gt(ROSA)26Sor^{tm1(cre/ERT2)Tyj}/J*, Stock No. 008463)

Parent 2: A *Ptch^{flox/flox}* mouse, generated by crossing two stock *Ptch^{flox}* mice (The Jackson Laboratory, strain *B6N.129-Ptch1^{tm1Hahn}/J*, Stock No. 012457)

The offspring of parents 1 and 2 will yield the desired mice for my study (*Ptch^{flox/flox}ERT2^{+/-}*). Once the mice have reached adulthood, I will inject them with 100µg of tamoxifen to initiate formation of BCC skin tumors. Immunohistochemistry assays of tumor biopsies will be performed to ensure that tumors are Hedgehog pathway-mediated. On days 50-90 after tamoxifen injection, I will topically apply an ointment of Au-Gli-Go (the Hedgehog pathway inhibitor developed in Aim 1) or appropriate control to BCC tumors, then irradiate the area with a laser for 1-2 minutes. Tumors will be treated and observed daily, checking for tumor shrinkage or disappearance due to the use of inhibitor. After the experiment ends on day 90 after BCC induction, the mice will be euthanized.

Mouse Specifics

Species: Laboratory mouse

Strain: *Ptch^{flox/flox}ERT2^{+/-}* mice, generated as described above

Ages: Parent mice 1 and 2 will be adults. *Ptch^{flox/flox}ERT2^{+/-}* mice will be raised from birth and kept until they are 4-5 months in age (taking into account time to reach maturity plus 90 days of experimentation).

Sex: Parents 1 and 2 will be opposite-gendered, and both genders of their offspring will be collected for experimentation.

Number: About 34 mice total will be used (see Justification below for breakdown).

Point 2: Justification

Mouse studies are a crucial step in determining the *in vivo* efficacy and clinical viability of treating BCC with Au-Gli-Co. Laboratory mice were selected because they are the least highly evolved animal whose skin bears a significant resemblance to human skin. *In vitro* models will be used to verify that the treatment does not induce toxicity in a 3D raft culture skin model, providing a measure of safety before transferring the procedure to living mice. However, the raft culture model will fail to address systemic complexities introduced by using a living creature, necessitating the use of mice. Similarly, computer models and simulations are not yet advanced enough to predict all the complexity and unexpected effects that may be observed in a living organism. Moreover, using a mouse model will allow me to appropriately compare the effects of my BCC treatment against other published studies that use mouse models.

The number of mice used will be minimized while also enabling testing of the necessary controls for my system. The number of mice needed for each portion of the experiment (breeding, full treatment, and controls) is detailed in the table below.

Table I.1. Mice needed for proposed in vivo experiment

Strain	Purpose	Experimental Treatment	Number Required
<i>Ptch</i> ^{fllox} (B6N.129- <i>Ptch</i> ^{tm1Hahn/J})	Breeding	-	2
<i>Ptch</i> ^{fllox/fllox}	Breeding	-	1
<i>Rosa26CreERT2</i> (B6.129- <i>Gt(ROSA)26Sor</i> ^{tm1(cre/ERT2)Tyj/J})	Breeding	-	1
<i>Ptch</i> ^{fllox/fllox} <i>ERT2</i> ^{+/-}	Full treatment	Au-Gli-Co + Irradiation	6
<i>Ptch</i> ^{fllox/fllox} <i>ERT2</i> ^{+/-}	Control	Au-Gli-Co	6
<i>Ptch</i> ^{fllox/fllox} <i>ERT2</i> ^{+/-}	Control	Fluorescent Gli-Co + Irradiation	6
<i>Ptch</i> ^{fllox/fllox} <i>ERT2</i> ^{+/-}	Control	Gli-Co + Irradiation	3
<i>Ptch</i> ^{fllox/fllox} <i>ERT2</i> ^{+/-}	Control	Au + Irradiation	3
<i>Ptch</i> ^{fllox/fllox} <i>ERT2</i> ^{+/-}	Control	Irradiation	3
<i>Ptch</i> ^{fllox/fllox} <i>ERT2</i> ^{+/-}	Control	-	3
		Total:	34

Point 3: Veterinary Care

Veterinary care will be provided by staff at the Developmental Therapeutics Core (DTC) at Northwestern. Staff will feed and monitor mice daily under normal conditions, as no special housing is required. The staff and principal investigator work at the same site at which the mice will be housed. DTC staff members are familiar with clinical indicators of mouse discomfort, distress, illness and pain. At least daily they will observe animal appetite, stool, typical behavior, and physical condition. If any of the above parameters are found to be unacceptable, a member of the NU veterinary staff will be notified and their recommendations followed. No survival surgeries are proposed, but if a mouse exhibits prolonged discomfort due to treatment methods or tumors, staff will intervene by inducing euthanasia.

DTC (under the umbrella of the Center for Comparative Medicine (CCM)) provides and oversees the humane care and use of animals, houses research animals and maintains support space and services for the use of Northwestern University faculty using animals. CCM provides training in the care and use of animals, and supports the activities of the NU Animal Care and Use Committee. The DTC facility contains barrier, conventional and containment housing for rodents. CCM employs approximately 97 fulltime staff which supports animal care activities at the University. CCM staff is separated into the following units: Animal Husbandry (58), Quality Assurance and Training (4), Business Office and Support Staff (19) and Veterinary staff (6 veterinarians and 8 Animal Health Technicians: total 16). Staff will perform daily rounds to monitor animals and are on site for approximately 4 hours on Saturdays and Sundays. The veterinarians are available for animal emergencies during nonbusiness hours on a rotating schedule.

Point 4: Discomfort

The mice in this study are expected to undergo only mild discomfort or pain, and no surgical procedures are planned. All relevant procedures are detailed below, with descriptions of measures that will be taken to ensure that discomfort, pain, and distress are minimized. Any animal that appears to suffer as a result of the effects of the procedures will be euthanized immediately to minimize any discomfort.

Procedures relevant to mouse distress/discomfort/pain:

- 1) When mice reach maturity, each will receive one injection of tamoxifen. Pain from this injection will be no more than momentary.
- 2) Beginning at 45 days after step 1, an ointment of Au-Gli-Co (or control) will be topically applied to skin tumors. No pain or discomfort is expected.
- 3) After ointment is applied, the area will be irradiated with a near-infrared laser. Although this is not expected to cause pain, it will be necessary to ensure that the mouse is immobile during the irradiation period of 1-3 minutes. This will be effected by administering gaseous isoflurane (1-3% with oxygen), a commonly used inhalable tranquilizer, for the duration of irradiation. A respiratory monitor will be taped to the animal's chest, after which it will be placed in a specially designed holder with a nosecone for administration of inhaled isoflurane at a rate of 0.5-3% as necessary to maintain steady respiration.
- 4) A small tissue biopsy will be collected while the mouse is under the effects of isoflurane. Anesthesia is considered complete when there is no flexor withdrawal in response to noxious foot pinch. A minimal amount of tissue will be taken to ensure rapid healing and minimal discomfort upon removal of anesthesia.

Point 5: Euthanasia

The method of euthanasia will be CO₂ asphyxiation followed by cervical dislocation. This method was chosen because it is quick and minimizes pain. The method is consistent with the Panel on Euthanasia of the American Veterinary Medical Association. Mice will be euthanized upon conclusion of experimental procedures or if they exhibit discomfort, as described above.

APPENDIX J: ZINC BINDING OF S100A7/EPIDERMAL FATTY ACID BINDING PROTEIN

An Original Research Proposal

By Elizabeth Bajema

J.1. Background and Objectives

J.1.1. Psoriasin (S100A7): A Host Defense Peptide

Protein S100A7, also known as psoriasin, is highly overexpressed in inflammatory skin conditions and infections, but its role and regulation are not well understood.¹⁻⁵ S100A7 is expressed in epithelial cells and mostly localizes to keratinocytes where it exhibits activity as a natural antimicrobial against *E. coli* and other bacteria and fungi. It is considered a host-defense peptide and is effective at combatting both gram+ and gram- bacteria as well as aiding in wound healing.⁶ The mechanism of antimicrobial action is not fully understood, but relies in part on psoriasin's abilities to permeabilize bacterial cell membranes,⁷ recruit leukocytes to inflamed keratinocytes,⁸ and sequester zinc.⁹

Other proteins in the S100 family, such as calprotectin, also use metal binding as a way to withhold necessary transition metals from bacterial cells,¹⁰⁻¹³ and S100A7 is believed to have a similar role via zinc and/or calcium sequestration.^{9,10,14,15} In support of this hypothesis, S100A7 was determined to have a sub-nanomolar affinity for Zn(II) and exhibits antibacterial activity against multiple bacterial species via zinc sequestration in vitro.¹⁵ Furthermore, higher zinc concentrations were shown to attenuate antifungal capacity, suggesting that once zinc binding

domains are occupied and excess Zn(II) remains available for bacteria, S100A7 can no longer exhibit further antifungal activity.¹⁶

J.1.2. Structure and Metal Binding of S100A7

Crystal structures of S100A7 homodimer (Figure J.1) show two EF-hand calcium binding domains and two His₃Asp zinc binding domains (His87/His91/His18'/Asp25') at the dimer interface.^{17,18} The N-terminal Ca(II) binding domain of S100A7 is three residues shorter than the EF-hand motifs of related S100 family proteins, and contains a Ser residue in place of an Asp/Glu in a Ca(II) binding site, which may be integral to its particular ion regulation and binding activity. Notably, each member of the homodimer can form an intramolecular disulfide bond between Cys47 and Cys96 with a physiologically relevant midpoint potential.¹⁵ Therefore, the homodimer can exist in reduced or oxidized forms in biology. The redox activity of disulfide bonds is postulated to play a role in metal ion binding, but conflicting accounts exist in the literature as to its effect.^{15,16}

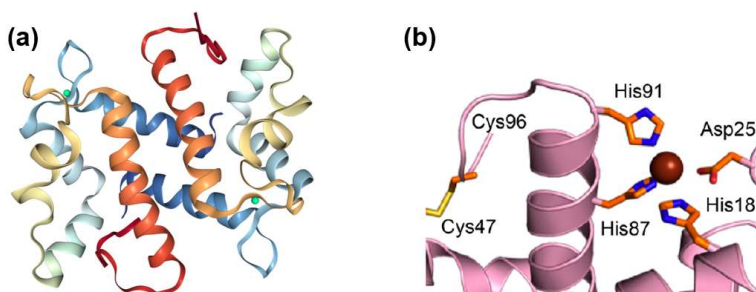


Figure J.1. (a) Crystal structure of S100A7 homodimer bound to two Ca(II) ions in the EF-hand domains. PDB 1PSR NGL viewer. (b) Closeup of Zn(II) bound in His₃Asp site at homodimer interface with distorted tetrahedral geometry. Also shown is the Cys47/Cys96 disulfide bond.⁹

J.1.3. S100A7 Complexation with Epidermal Fatty Acid Binding Protein (E-FABP)

Under some conditions, S100A7 complexes with epidermal fatty acid binding protein (E-FABP) and moves to peripheral structures, but little is known about the biological role of this interaction.^{19,20} Both calcium and zinc concentrations can affect S100A7/E-FABP complexation, but the effects of these two metals have not been studied in tandem, and some accounts are conflicting. Low calcium concentrations promote increased complexation of S100A7/E-FABP, while low zinc concentrations promote monomerization.²¹ Thus, the presence of unbound calcium and zinc is important to the interaction, and complexation may be driven by the relative metal binding affinities of S100A7 in complexed and uncomplexed states. The complexation of S100A7 and E-FABP is hypothesized to play a role in antimicrobial activity, as has been demonstrated with other S100 protein family interactions.^{9,19,22}

J.1.4. Scientific Objectives

The proposed studies will investigate both the metal binding affinities and biological behavior of S100A7 and its complexation with E-FABP. These studies will significantly contribute to our understanding of how zinc and calcium binding affect the S100A7/E-FABP interaction. This would provide useful biochemical insight into the control of metals in psoriatic skin; metals are known to play a large role, but little is known of how cells perform this regulation. Moreover, knowledge of the S100A7/E-FABP interaction would help guide therapeutic efforts aimed at inflammatory skin diseases and immune response.²³

Specifically, I propose to determine zinc binding affinities of (1) S100A7 and (2) complexed S100A7/E-FABP proteins. This comparative study will help to elucidate whether

calcium or zinc concentrations affect protein complexation and its role as a host defense protein.

To achieve this goal, I propose three specific aims.

Aim 1: Isolate S100A7 and S100A7/E-FABP from psoriatic cells by methods with literature precedent.¹⁹

Aim 2: Determine zinc-binding affinities of S100A7 (uncomplexed) and S100A7/E-FABP (complexed) in various concentrations of calcium. This will be achieved using the ZinPyr4 zinc binding chromophore.

Aim 3: Study behavior of S100A7 and S100A7/E-FABP in live cells, using 2D cultures of primary human keratinocytes and 3D organotypic raft cultures. 2D cultures will be analyzed via Western blot and qPCR. 3D cultures will undergo laser capture micro-dissection and confocal microscopy.^{24,25}

J.2. Specific Aim 1: Isolate S100A7 and S100A7/E-FABP from psoriatic cells by methods with literature precedent.¹⁹

J.2.1. Protein Isolation Procedure

Given the known overexpression of S100A7 in psoriasis, protein will be isolated from psoriatic skin samples. Samples can be readily obtained from Northwestern's Skin Disease Research Center through the Dermatopathology Tissue Repository for Research²⁶ or from diagnostic biopsies and scraping of lesional skin. The protocol by Hagens et al.¹⁹ will be used to isolate protein from the tissue sample. In brief, psoriatic tissues will be homogenized and centrifuged, then the cytosolic fraction will undergo Sephadex G-100 filtration and ion-exchange HPLC purification. The resulting protein solution will be subjected to SDS-PAGE, and

immunoblotting will be performed for both S100A7 and E-FABP. Using this method, I expect to obtain free S100A7, free E-FABP, and complexed S100A7/E-FABP.

J.2.2. Experimental Challenges and Contingency Plans

Should isolation of S100A7 and S100A7/E-FABP from cells prove irreproducible or too low-yielding, recombinant protein can be expressed in bacterial cells and isolated. This would require separate expression of S100A7 and E-FABP and use of a cleavable protein tag (FLAG tag, His-tag, or GST). This is slightly less desirable due to the proteins' non-native state, but the products could still be carried forward into Aim 2. If either protein cannot be isolated, a number of other similar and biologically relevant binding partners exist. S100A15 could be used in place of S100A7, or RANBP9 could be used in place of E-FABP.^{27,28}

J.3. Specific Aim 2: Determine zinc binding affinities of S100A7 (uncomplexed) and S100A7/E-FABP (complexed) in various concentrations of calcium. This will be achieved using the ZinPyr4 zinc binding chromophore.

J.3.1. Determining Zinc Binding Affinities

First, using methods similar to literature precedent,²² I will modulate both calcium and zinc concentrations to determine what, if any, relationship exists between metal ion concentrations and S100A7 zinc binding affinity. ZinPyr-4, a fluorescent, zinc-selective indicator will be used for measurements.²⁹ ZinPyr-4 (Figure J.2) was selected for its tight binding of Zn(II) ($K_{d,Zn(II)} \sim 0.7\text{nM}$) and high quantum yield ($\Phi = \sim 0.4$). Upon binding Zn(II), a 5-fold fluorescence enhancement occurs with $\text{ex/em} = 495/515\text{ nm}$.³⁰ This will be used to determine the zinc binding affinities of

S100A7 and complexed S100A7/E-FABP. The experiments will be carried out in a series of 10 calcium concentrations in order to elucidate the relationship between zinc binding and the presence of calcium. Fluorescence spectra will be integrated from 505 to 650 nm to quantify zinc interactions.

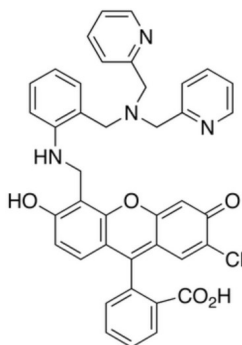


Figure J.2. Chemical structure of ZinPyr-4. Upon binding zinc ($K_d \sim 0.7$ nM), ZinPyr-4 undergoes a 5-fold increase in fluorescent intensity.

J.3.2. Calcium Competition Studies

Next, competition titrations with S100A7 vs. ZinPyr-4 and S100A7/E-FABP vs. ZinPyr-4 will be performed. This will allow for a more thorough understanding of the role of calcium binding in the zinc/S100A7 interaction. In this assay, S100A7 or S100A7/E-FABP with ZinPyr-4 will be titrated with zinc for maximal fluorescence, then calcium will be added, and emission spectra will be observed over multiple hours. If high calcium concentrations cause an increase in zinc binding affinity, fluorescence will be attenuated as zinc is bound by protein. If calcium concentrations do not affect zinc binding affinity, no change will be observed.

I predict that S100A7 will have a higher zinc binding affinity in its uncomplexed state, and, accordingly, in higher concentrations of calcium. This matches physiological observations that

psoriatic lesions have high concentrations of free calcium and are also resistant to fungal infection via the activity of S100A7.^{19,31}

J.3.3. Experimental Challenges and Contingency Plans

It is possible that divalent calcium ions will interfere with ZinPyr-4 readings. By carefully observing controls in the first few experiments, I will determine whether Ca^{2+} is interfering under my experimental conditions. In the case of interference, I will use FluoZin3 as an alternate fluorescent probe for determining zinc binding affinity. FluoZin3 (Figure J.3) has a lower binding affinity for zinc ($K_d, \text{Zn(II)} \sim 15\text{nM}$), but will likely be suitable for the purposes of this proposal. FluoZin3 has $\lambda_{\text{ex}} = 493 \text{ nm}$, and fluorescence spectra will be integrated from 500 to 650 nm to quantify zinc interactions. Using FluoZin3, concentrations of up to 10 mM Ca^{2+} and μM amounts of EDTA- Ca^{2+} will not perturb zinc measurements.³²

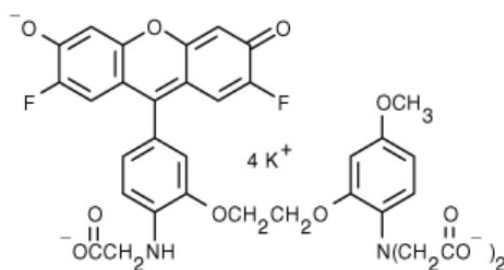


Figure J.3. Chemical structure of FluoZin3. FluoZin3 binds zinc with $K_d = 15 \text{ nM}$, but can be used as an alternative fluorescent probe for the S100A7/EFABP system.

J.4. Specific Aim 3: Study behavior of S100A7 and S100A7/E-FABP in live cells, using 2D cultures of primary human keratinocytes and 3D organotypic raft cultures.

J.4.1. Primary Keratinocyte Studies

Primary keratinocytes from neonatal foreskin will be cultured in the presence of varying concentrations of both calcium and zinc. The cultured cells will be analyzed for the presence of S100A7 and S100A7/E-FABP by performing Western blots and immunostaining for both proteins. For validation, qPCR will also be performed to measure expression levels of both proteins. Antibodies for both S100A7 and E-FABP are commercially available, and similar investigations have been performed without regard to metal ion concentrations. Pending results from Aim 2, I predict that it will be possible to observe changes in S100A7/E-FABP protein complexation and colocalization depending on calcium and zinc concentration in cell culture media.

J.4.2. 3D Organotypic Skin Cultures

3D organotypic raft cultures will be generated in collaboration with the SDRC's Skin Tissue Morphology and Engineering core. Primary keratinocytes will be grown on a collagen plug at the air/medium interface with various concentrations of calcium and zinc. These cells will differentiate to roughly approximate a human epidermis as shown in Figure J.4.³³

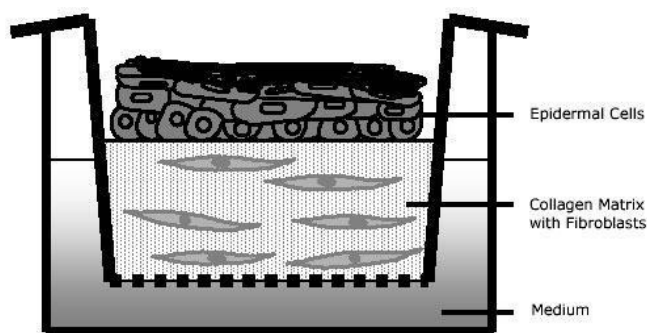


Figure J.4. Illustration of a 3D organotypic skin culture. Keratinocytes grown at the air-medium interface will differentiate into an epidermis-like structure, useful for studying live skin-like tissue without necessitating patients or animals.³³

3D cultures will be treated with fluorescently labeled versions of S100A7 and E-FABP according to literature precedent.²⁰ Subsequently, laser capture micro dissection will be performed to generating small cross-sections of tissue for analysis. Tissue cross-sections will be analyzed via confocal microscopy for extent of colocalization of S100A7 and E-FABP under various calcium and zinc growth conditions. Higher calcium and zinc concentrations are expected to yield less colocalization of S100A7 and E-FABP.

J.4.3. Experimental Challenges and Contingency Plans

It may not be possible to perform confocal microscopy of tissue cross sections, or the fluorescently-labeled proteins may not be observable in this system. In this case, two alternative strategies can be employed:

- (1) The 3D cultures will undergo Western blots, qPCR, and immunostaining for the two proteins of interest. This has the downside of not providing information regarding protein localization, but will still allow for analysis of protein levels in a skin-like system that more closely approximates *in vivo* conditions.
- (2) Primary keratinocytes in 2D culture will be transfected with fluorescently labeled S100A7 and E-FABP. Performing confocal microscopy on these samples should not prove as technically challenging as the differentiated 3D samples, but would be a poorer approximation of conditions in human epidermis. This method has previously been employed successfully (see Figure J.5), but without regard to metal ion concentrations.

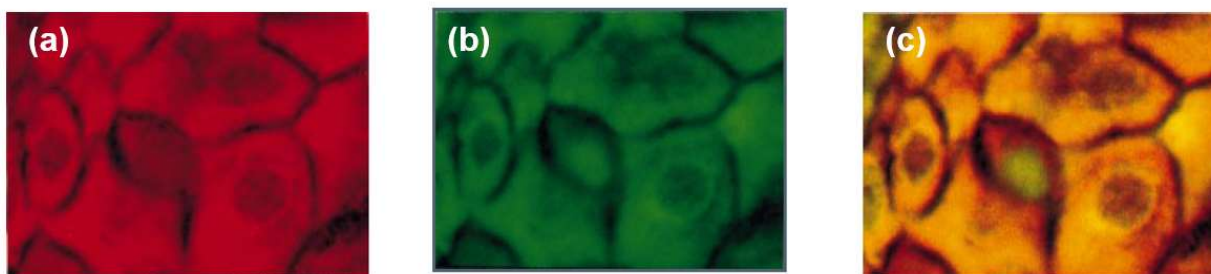


Figure J.5. Confocal microscopy analysis for (a) E-FABP, (b) S100A7, and (c) overlay demonstrating colocalization in keratinocytes.

J.5. Conclusions

Aims 1 and 2 of the proposed investigation will allow us to gain a clear understanding of the calcium- and zinc-dependence of the S100A7/E-FABP protein interaction. This will provide invaluable information for determining the role of metal binding in antimicrobial activity as well as protein partner binding. Aim 3 will provide information on how this set of protein partners interacts biologically in cells and in whole tissue approximations. Given the unique localization of these proteins to keratinocytes, this is a crucial next step that will provide context to the biochemical results obtained in Aims 1 and 2.

J.6. References for Appendix J

- (1) Gross, S. R.; Sin, C. G. T.; Barraclough, R.; Rudland, P. S. Joining S100 Proteins and Migration: For Better or for Worse, in Sickness and in Health. *Cell Mol Life Sci* **2014**, *71* (9), 1551–1579.
- (2) Jia, J.; Duan, Q.; Guo, J.; Zheng, Y. Psoriasin, A Multifunctional Player in Different Diseases. *Curr Protein Pept Sci* **2014**, *15* (8), 836–842.
- (3) Madsen, P.; Rasmussen, H. H.; Leffers, H.; Honoré, B.; Dejgaard, K.; Olsen, E.; Kiil, J.; Walbum, E.; Andersen, A. H.; Basse, B.; et al. Molecular Cloning, Occurrence, and Expression of a Novel Partially Secreted Protein “Psoriasis” That Is Highly up-Regulated in Psoriatic Skin. *J. Invest. Dermatol.* **1991**, *97* (4), 701–712.

- (4) Fulton, C.; Anderson, G. M.; Zasloff, M.; Bull, R.; Quinn, A. G. Expression of Natural Peptide Antibiotics in Human Skin. *Lancet* **1997**, *350* (9093), 1750–1751.
- (5) Schitteck, B.; Paulmann, M.; Senyürek, I.; Steffen, H. The Role of Antimicrobial Peptides in Human Skin and in Skin Infectious Diseases. *Infect. Disord. - Drug Targets* **2008**, *8* (3), 135–143.
- (6) Steinstraesser, L.; Koehler, T.; Jacobsen, F.; Daigeler, A.; Goertz, O.; Langer, S.; Kesting, M.; Steinau, H.; Eriksson, E.; Hirsch, T. Host Defense Peptides in Wound Healing. *Mol. Med.* **2008**, *14* (7–8), 528–537.
- (7) Michalek, M.; Gelhaus, C.; Hecht, O.; Podschun, R.; Schröder, J. M.; Leippe, M.; Grötzinger, J. The Human Antimicrobial Protein Psoriasin Acts by Permeabilization of Bacterial Membranes. *Dev. Comp. Immunol.* **2009**, *33* (6), 740–746.
- (8) Wolf, R.; Howard, O. M. Z.; Dong, H.-F.; Voscopoulos, C.; Boeshans, K.; Winston, J.; Divi, R.; Gunsior, M.; Goldsmith, P.; Ahvazi, B.; et al. Chemotactic Activity of S100A7 (Psoriasin) Is Mediated by the Receptor for Advanced Glycation End Products and Potentiates Inflammation with Highly Homologous but Functionally Distinct S100A15. *J. Immunol.* **2008**, *181* (2), 1499–1506.
- (9) Cunden, L. S.; Nolan, E. M. Bioinorganic Explorations of Zn(II) Sequestration by Human S100 Host-Defense Proteins. *Biochemistry* **2018**, *57* (11), 1673–1680.
- (10) Zackular, J. P.; Skaar, E. P.; Chazin, W. J. Nutritional Immunity: S100 Proteins at the Host-Pathogen Interface. *J Biol Chem* **2015**, *290* (31), 18991–18998.
- (11) Hood, M. I.; Skaar, E. P. Nutritional Immunity: Transition Metals at the Pathogen–Host Interface. *Nat Rev Micro* **2012**, *10* (8), 525–537.
- (12) Cunden, L. S.; Gaillard, A.; Nolan, E. M. Calcium Ions Tune the Zinc-Sequestering Properties and Antimicrobial Activity of Human S100A12. *Chem Sci* **2016**, *7* (2), 1338–1348.
- (13) Kehl-Fie, T. E.; Skaar, E. P. Nutritional Immunity beyond Iron: A Role for Manganese and Zinc. *Curr. Opin. Chem. Biol.* **2010**, *14* (2), 218–224.
- (14) Lee, K. C.; Eckert, R. L. S100A7 (Psoriasin) - Mechanism of Antibacterial Action in Wounds. *J Invest Dermatol* **2006**, *127* (4), 945–957.
- (15) Cunden, L. S.; Brophy, M. B.; Rodriguez, G. E.; Flaxman, H. A.; Nolan, E. M. Biochemical and Functional Evaluation of the Intramolecular Disulfide Bonds in the Zinc-Chelating Antimicrobial Protein Human S100A7 (Psoriasin). *Biochemistry* **2017**, *56* (43), 5726–5738.
- (16) Hein, K. Z.; Takahashi, H.; Morita, E.; Tsumori, T.; Yasui, Y.; Nanjoh, Y.; Toga, T.; Wu, Z.; Schroeder, J. M.; Grotzinger, J.; et al. Disulphide-Reduced Psoriasin Is a Human Apoptosis-Inducing Broad-Spectrum Fungicide. *Proc Natl Acad Sci U A* **2015**, *112* (42), 13039–13044.

- (17) Brodersen, D. E.; Etzerodt, M.; Madsen, P.; Celis, J. E.; Thøgersen, H. C.; Nyborg, J.; Kjeldgaard, M. EF-Hands at Atomic Resolution: The Structure of Human Psoriasin (S100A7) Solved by MAD Phasing. *Struct. Lond. Engl.* **1998**, *6* (4), 477–489.
- (18) Brodersen, D. E.; Nyborg, J.; Kjeldgaard, M. Zinc-Binding Site of an S100 Protein Revealed. Two Crystal Structures of Ca²⁺-Bound Human Psoriasin (S100A7) in the Zn²⁺-Loaded and Zn²⁺-Free States. *Biochemistry* **1999**, *38* (6), 1695–1704.
- (19) Hagens, G.; Masouye, I.; Augsburger, E.; Hotz, R.; Saurat, J.-H.; Siegenthaler, G. Calcium-Binding Protein S100A7 and Epidermal-Type Fatty Acid-Binding Protein Are Associated in the Cytosol of Human Keratinocytes. *Biochem J* **1999**, *339* (2), 419–427.
- (20) Ruse, M.; Broome, A.-M.; Eckert, R. L. S100A7 (Psoriasin) Interacts with Epidermal Fatty Acid Binding Protein and Localizes in Focal Adhesion-Like Structures in Cultured Keratinocytes. *J. Invest. Dermatol.* **2003**, *121* (1), 132–141.
- (21) Cubillos, S.; Jaradat, S. W.; Truta-Feles, K.; Koehler, M. J.; Norgauer, J.; Walther, M. Association of S100A7 Gene Polymorphisms with Manifestations of Common Types of Psoriasis: Effect on Serum Calcium Levels. *Exp Dermatol* **2015**, *24* (11), 894–896.
- (22) Brophy, M. B.; Hayden, J. A.; Nolan, E. M. Calcium Ion Gradients Modulate the Zinc Affinity and Antibacterial Activity of Human Calprotectin. *J. Am. Chem. Soc.* **2012**, *134* (43), 18089–18100.
- (23) D'Amico, F.; Skarmoutsou, E.; Granata, M.; Trovato, C.; Rossi, G. A.; Mazzarino, M. C. S100A7: A RAMPing up AMP Molecule in Psoriasis. *Cytokine Growth Factor Rev* **2016**, Ahead of Print.
- (24) Curran, S.; McKay, J. A.; McLeod, H. L.; Murray, G. I. Laser Capture Microscopy. *Mol. Pathol.* **2000**, *53* (2), 64–68.
- (25) Anacker, D.; Moody, C. Generation of Organotypic Raft Cultures from Primary Human Keratinocytes. *J Vis Exp* **2012**, No. 60.
- (26) Northwestern University. Dermatology Archived Tissue Biorepository Request Form <https://www.skinresearch.northwestern.edu/research/Archived%20tissue-request-form%20html.html> (accessed Oct 8, 2018).
- (27) Zwicker, S.; Bureik, D.; Ruzicka, T.; Wolf, R. [Friend or Foe?--Psoriasin and Koebnerisin: multifunctional defence molecules in skin differentiation, tumorigenesis and inflammation]. *Dtsch. Med. Wochenschr.* **1946** *2012*, *137* (10), 491–494.
- (28) Emberley, E. D.; Gietz, R. D.; Campbell, J. D.; HayGlass, K. T.; Murphy, L. C.; Watson, P. H. RanBPM Interacts with Psoriasin in Vitro and Their Expression Correlates with Specific Clinical Features in Vivo in Breast Cancer. *BMC Cancer* **2002**, *2*, 28.

- (29) Koh, J. Y.; Suh, S. W.; Gwag, B. J.; He, Y. Y.; Hsu, C. Y.; Choi, D. W. The Role of Zinc in Selective Neuronal Death after Transient Global Cerebral Ischemia. *Science* **1996**, *272* (5264), 1013–1016.
- (30) Burdette, S. C.; Frederickson, C. J.; Bu, W.; Lippard, S. J. ZP4, an Improved Neuronal Zn²⁺ Sensor of the Zinpyr Family. *J. Am. Chem. Soc.* **2003**, *125* (7), 1778–1787.
- (31) Hagens, G.; Roulin, K.; Hotz, R.; Saurat, J.-H.; Hellman, U.; Siegenthaler, G. Probable Interaction between S100A7 and E-FABP in the Cytosol of Human Keratinocytes from Psoriatic Scales. *Mol. Cell. Biochem.* **1999**, *192* (1), 123–128.
- (32) Zhao, J.; Bertoglio, B. A.; Gee, K. R.; Kay, A. R. The Zinc Indicator FluoZin-3 Is Not Perturbed Significantly by Physiological Levels of Calcium or Magnesium. *Cell Calcium* **2008**, *44* (4), 422–426.
- (33) Stark, H.-J.; Szabowski, A.; Fusenig, N. E.; Maas-Szabowski, N. Organotypic Cocultures as Skin Equivalents: A Complex and Sophisticated in Vitro System. *Biol. Proced. Online* **2004**, *6*, 55–60.
- (34) Rohleder, N. H.; Wolff, K.-D.; Heimüller, S.; Axt, A.; Kesting, M. R.; Koerdt, S.; Mücke, T.; Rommel, N. Influence of Gender on Epithelial Host Defence Peptide Gene Expression under Non-Infected and Infected Conditions: A Basic Medical Research Study. *J. Cranio-Maxillofac. Surg.* **2018**, *46* (1), 128–134.